UC Irvine
UC Irvine Electronic Theses and Dissertations

Title
Understanding how irrigation, plant physiology, and the Madden-Julian Oscillation shape regional water cycles and their extremes

Permalink
https://escholarship.org/uc/item/5z40c6c0

Author
Fowler, Megan Devlan

Publication Date
2019

License
https://creativecommons.org/licenses/by-nc-nd/4.0/ 4.0

Peer reviewed|Thesis/dissertation

eScholarship.org Powered by the California Digital Library
University of California

UNIVERSITY OF CALIFORNIA,
IRVINE

Understanding how irrigation, plant physiology, and the Madden-Julian Oscillation shape regional water cycles and their extremes

DISSERTATION

submitted in partial satisfaction of the requirements
for the degree of

DOCTOR OF PHILOSOPHY

in Earth System Science

by

Megan Devlan Fowler

Dissertation Committee:
Associate Professor Michael S. Pritchard, Chair
UCI Chancellor's Professor of Earth System Science James T. Randerson
Associate Professor Steven J. Davis

2019

Chapter 2 © American Meteorological Society. Used with permission.
Chapter 3 © 2019 Megan D. Fowler, Gabriel J. Kooperman, James T. Randerson, and Michael S. Pritchard
Chapter 4 © 2019 Megan D. Fowler and Michael S. Pritchard
All other materials © 2019 Megan D. Fowler

DEDICATION

I dedicate this dissertation to my incredible partner, for his endless wit, love, and support.

TABLE OF CONTENTS

Page

LIST OF FIGURES ..... **v**

LIST OF TABLES ..... **viii**

ACKNOWLEDGEMENTS ..... **ix**

CURRICULUM VITAE ..... **x**

ABSTRACT OF THE DISSERTATION ..... **xiv**

1 Introduction **1**
- 1.1 Research overview 1
- 1.2 Irrigation and its ability to modify the climate 3
- 1.3 Future changes in streamflow and flooding 8
- 1.4 MJO modulation of tropical cyclones in the West Pacific 14
- 1.5 Organization 18

2 Assessing the impact of Indian irrigation on precipitation in the irrigation enabled Community Earth System Model **19**
- 2.1 Introduction 21
- 2.2 Methods 24
- 2.3 Results and Discussion 29
  - 2.3.1 Surface cooling and evapotranspiration responses 29
  - 2.3.2 Initial adjustment timescale 31
  - 2.3.3 Unrealistic aspects of the local land surface response to irrigation 33
  - 2.3.4 Robust but synoptically sensitive non-local precipitation responses 36
  - 2.3.5 Details of the fast response and the role of moisture advection 42
  - 2.3.6 A dynamic limitation of ET response magnitude 46
- 2.4 Summary and Conclusions 48
- 2.5 Acknowledgements 52

3 Identifying the effect of plant physiological responses to rising CO_2 on global streamflow **53**
- 3.1 Introduction 54
- 3.2 Methods 56
  - 3.2.1 Methods summary 56
  - 3.2.2 CESM experiments 58
  - 3.2.3 Hydrodynamic downscaling and extreme value curve fitting .. 59
  - 3.2.4 Defining grid cells as *RAD*-driven, *PHYS*-driven, or multiply stressed 61

3.3 Results and discussion 61
3.3.1 Physiological and radiative effects on extreme flooding 61
3.3.2 Detecting a plant-physiological effect on annual streamflow metrics 65
3.3.3 Quantifying radiative and physiological contributions to basin-level streamflow changes 69
3.4 Conclusions 73
3.5 Acknowledgements 74

4 Regional MJO modulation of West Pacific tropical cyclones driven by multiple transient controls 75
4.1 Introduction 76
4.2 Data and methods 81
4.3 Results 83
4.4 Discussion and conclusions 92
4.5 Acknowledgements 95

5 Conclusion 96
5.1 Non-local precipitation responses to irrigation. 96
5.2 Flood and streamflow responses to future plant-physiological changes 98
5.3 Present day TC modulation in the West Pacific by the MJO 101

Bibliography 105

Appendix A Supplementary Information for Chapter 2 119
A.1 Double irrigated area experiment 120
A.2 Climatological simulations of irrigation in California's Central Valley 120
A.3 Supporting figures 122

Appendix B Supplementary Information for Chapter 3 132
B.1 Evapotranspiration and vegetation response 133
B.2 Environmental drivers of flood increases 134
B.3 Supporting figures and tables 136

Appendix C Supplementary Information for Chapter 4 161
4.1 Creation of MJO phase climatologies 162
4.2 Supporting figures 163

LIST OF FIGURES

		Page
Figure 2.1	Magnitude and location of irrigation-induced surface water source over India. Shading shows the average irrigation amount (mm/day) over the full 45-day period for the 60-member IRRIG ensemble mean. The inset rectangle outlines the "heavily irrigated" region	26
Figure 2.2	Daily progression of (a) ET, and (b) near-surface (2 m) temperature for the CTRL (black), IRRIG (blue), and IRRIG2X (red) experiments. Averages are taken over all 60- ensemble members in the heavily irrigated region defined by Figure 2.1. Error bars represent twice the standard error of all 60 ensemble members (~95% confidence level). Daily observational constraints, averaged over the period 2003-2015, are included for ET (from GLEAM) and temperature (from ERA-Interim). Day one of both observations is set to May 15th, and error bars again show twice the standard error of the 13 years of observations	29
Figure 2.3	Daily progression of (a) irrigation amounts, and (b) surface runoff. Averages are taken over all 60-ensemble members in the heavily irrigated region defined by Figure 2.1. Error bars represent twice the standard error of all 60 ensemble members (~95% confidence level)	32
Figure 2.4	Daily progression of vertically integrated soil moisture in (a) the top 1m of soil, (b) the top 11cm of soil, and (c) in the topmost level of the soil column only. Averages are taken over all 60-ensemble members in the heavily irrigated region defined by Figure 2.1. Error bars represent twice the standard error of all 60 ensemble members (~95% confidence level). (d) The distribution of roots for the crop PFT across all levels of the soil column, as determined by Eq. 8.21 in Oleson et al. [2010]	33
Figure 2.5	Ensemble mean difference (IRRIG-CTRL) in days 8-45 average (a,b) ET, (c,d) near-surface temperature, and (e,f) precipitation in the May 15th ensemble. The second column is the same as the first, but the region shown is restricted to the area of largest changes for easier viewing. Stippling represents significance at the 95% level as determined by the standard error of the differences between irrigation and control ensemble members	37
Figure 2.6	Change in precipitation (irrigation – control) over days 2-10 of the simulations for the 60-member ensemble mean with original irrigated area (a) and doubled irrigated area (b),and for the 20-member initialization date sub-ensemble means: May 10th (c,d), May 15th (e,f), and May 20th (g,h), where the left column gives the results of the IRRIG experiment, and the right column shows the IRRIG2X experiment	39

Figure 2.7 As in Figure 2.6, but with averages taken over the full period (days 8-45) 41
Figure 2.8 As in Figure 2.6, but with changes (IRRIG-CTRL left; IRRIG2X-CTRL right) shown as percent rather than absolute values 43
Figure 2.9 May 20th IRRIG ensemble mean response of vertically integrated precipitable water (IRRIG-CTRL) during the first 10 days of the simulation 45
Figure 2.10 ET' decomposition into (a) wind-driven and (b) thermally-driven components, as determined by the full 60-member IRRIG ensemble mean May values for each term 47
Figure 3.1 Frequency of the pre-industrial 100-year flood under elevated CO2 and its drivers. (a) Return period of the historical 100-year flood in FULL vs. (b) the results of H13 for a multi- model average under RCP8.5 forcing (H13 Figure 1; dry regions masked). (c) PHYS and (d) RAD as individual drivers of flood responses in FULL. (e) Regional categorization of flood increases as primarily PHYS-driven (green), RAD-driven (orange), or a combination of both (blue) based on their contributions to the return period of the CTRL100 flood in FULL. Results omitted in (a, c-e) where insignificant at 95% confidence (see text) 63
Figure 3.2 Changes in seasonal streamflow. (a,b) Percent change from CTRL in low and peak streamflow for FULL; regions with CTRL Q_{low} discharge less than 50 or Q_{peak} less than 500 m3 s-1 masked (Fig. B.5). (c,d) Latitudinal decomposition of FULL into PHYS and RAD smoothed 5° running mean; shading denotes zonal variability as the interquartile range 66
Figure 3.3 Basin-level streamflow changes. FULL changes in (a) Q_{mean}, (b) Q_{peak}, and (c) Q_{low} relative to CTRL. (d-f) The contributions of $\Delta PHYS$ and ΔRAD to ΔFULL flow changes. Black stars represent the FULL percent change from CTRL (as shown by shaded circles in a-c), and black circles represent the sum of $\Delta PHYS$ and ΔRAD. Colored bars indicate the ΔPHYS (green) + ΔRAD (blue) percent changes that support the total 70
Figure 3.4 Average annual streamflow cycles at river outlets in PHYS-dominated basins. Area-weighted average streamflow annual cycles near the outlets of each river. Dashed black lines represent nearby GRDC station data (all available years in the period 1970-2005) while colored lines show modeled streamflow, where all grid cells within a quarter degree of the GRDC station have been averaged together. Error bars correspond to twice the standard error of discharge over the 30-year period 71
Figure 4.1 Genesis density of MIT model generated storms in each phase of the MJO as defined by RMM (right) and OMI (left) during the active season (Jun-Nov). Boundaries of each sub-domain are marked in white 85

Figure 4.2 (a) Anomalous GPI for each phase of the OMI-defined MJO (x-axis), relative to the Phase 1-8 mean, as computed in Equation 1. Each of the five regions outlined in (b) are assessed independently, shown as colored bars in (a), which represent the mean of the 100-member bootstrap for the TC season of June-November with error bars corresponding to the 25th and 75th percentiles of that analysis 88

Figure 4.3 (Left hand side) Average 850 (blue) and 250 mb (green) winds in the 100-member bootstrap ensemble for each phase of the MJO; dashed lines represent the Phase 1-8 mean. (Right hand side) Average GPI decomposition from Equation 1 for each phase of the MJO, taken from the 100-member bootstrap ensemble. Error bars correspond to the 25th and 75th percentiles as in Figure 2. These averages are taken for each region over the TC season of June-November 90

LIST OF TABLES

Page

Table 2.1 Summary of experiments used in this study 28
Table 4.1 Summary of methods and findings of the MJO-TC relationship in the West Pacific 79

ACKNOWLEDGMENTS

First and foremost, I would like to thank my advisor, Mike Pritchard. Your guidance and support have been immensely valuable over the course of my PhD, and I've truly appreciated the opportunities you've given me to grow and learn as a scientist. I simply could not have asked for a better mentor, and I'll be forever grateful.

I would also like to thank my dissertation committee, Jim Randerson and Steve Davis, for their advice over the last few years. Your input on these projects and on the long journey towards a doctorate have greatly improved my work and helped me along the way. Thank you also to Gabe Kooperman, who helped me spin-up on climate modeling and graduate-level research during my first summer at UCI and has been a wonderful mentor and collaborator ever since.

I'd also like to thank Ken Bowman at Texas A&M, as well as Gino Izzi and Eric Lenning at the Chicago National Weather Service, for their mentoring and guidance during my undergraduate research projects. Working with each of them helped foster my love of research and science, solidifying my decision to go after a PhD.

The PhD experience would be even more difficult without the many friends and colleagues that I've met in my time at UC Irvine. I would like to thank my cohort in particular, and offer a special thank you to: Felicia Chiang, Tom Beucler, Chris Terai, Hongchen Qin, Galen Yacalis, Stefan Rasp, Sungduk Yu, Griffin Mooers, Jacob Hendrickson, Hossen Parishani, Baird Langenbrunner, Jessica Wang, Zack Labe, Shih-Wei Fang, and Zach Wolff. I also gratefully acknowledge the support of Elliot McCollum and the entire administrative staff for all their help over the years and with this process.

An immense thank you also to my parents, who have helped and encouraged me to chase after my dreams ever since I was little; I wouldn't be here without you. To my partner, Ian Heming – thank you for being you. Your humor has kept me going for the last few years, and I am eternally grateful for all that you've done to help me get here.

Funding for this work was provided by the Department of Energy (DE-SC0012152), the NSF (AGS-1734164), NASA MIRO (NNX15AQ06A) and the Department of Earth System Science at University of California – Irvine. Computational resources were provided by the Extreme Science and Engineering Discovery Environment (XSEDE) supported systems – Stampede, Stampede2, and Comet, as well as by the National Energy Research Scientific Computer Center (NERSC).

CURRICULUM VITAE

MEGAN DEVLAN FOWLER

EDUCATION

Ph.D. Earth Systems Science **Jul 2019**
University of California – Irvine, Irvine, CA
Advisor: Michael S. Pritchard
Thesis: Understanding how irrigation, plant physiology, and the Madden-Julian Oscillation shape regional water cycles and their extremes

M.S. Earth System Science **Dec 2017**
University of California – Irvine, Irvine, CA

B.S. Meteorology **Dec 2014**
Texas A&M University, College Station, TX
Summa Cum Laude

PUBLICATIONS

5. Fowler, M.D. and M.S. Pritchard (*in prep.*.; 2019): Complex MJO modulation of West Pacific tropical cyclones revealed through regional hotstpots with multiple transient controls.

4. Fowler, M.D., G.J. Kooperman, J.T. Randerson and M.S. Pritchard (*in review at Nat. Clim. Change*; 2019): Identifying the effect of plant-physiological responses to rising CO_2 on global streamflow.

3. Kooperman, G.J., M.D. Fowler, F.M. Hoffman, C.D. Koven, K. Lindsay, M.S. Pritchard, A.L.S. Swann, J.T. Randerson (2018): Plant physiological responses to rising CO_2 modify simulated daily runoff intensity with implications for global-scale flood risk assessment. *Geophysical Research Letters*, 45, 12457–12466. doi: https://doi.org/10.1029/2018GL079901

2. Fowler, M.D., M.S. Pritchard and G.J. Kooperman, (2018): Assessing the impact of Indian irrigation on precipitation in the irrigation-enabled Community Earth System Model. *J. Hydromet.*, 19, 427–443, doi: https://doi.org/10.1175/JHM-D-17-0038.1

1. Bowman, K.P., and M.D. Fowler (2015): The diurnal cycle of precipitation in tropical cyclones. *J. Climate*, 28, 5325-5334. doi: http://dx.doi.org/10.1175/JCLI-D-14-00804.1

PRESENTATIONS

Fowler, M.D., G.J. Kooperman, J.T. Randerson, and M.S. Pritchard (2019): *Global river responses to rising CO_2: Separating the effects of physiological and radiative changes on streamflow and flooding*. Oral Presentation. Land Model Working Group, Boulder, CO. Feb 12.

Fowler, M.D., M.S. Pritchard, G.J. Kooperman, and J.T. Randerson (2018): *Global river responses to rising CO_2: Separating the effects of physiological and radiative changes on streamflow and flooding*. Poster. American Geophysical Union Fall Meeting, Washington D.C. Dec 13.

Fowler, M.D., M.S. Pritchard, G.J. Kooperman, and J.T. Randerson (2018): *Global river responses to rising CO_2: Separating the effects of physiological and radiative changes on streamflow and flooding*. Oral and poster presentation. U.S. Department of Energy Regional & Global Climate Modeling (RGCM) Program – Principal Investigators Meeting, Potomac, MD. Nov. 8.

Fowler, M.D. and M.S. Pritchard (2018): *Investigating the Ability of Global Climate Models to Simulate MJO Modulation of Tropical Cyclone Activity in the Pacific Basin*. Poster. American Meteorological Society Annual Meeting, Austin, TX. Jan 8.

Fowler, M.D., G.J. Kooperman, M.S. Pritchard, and J.T. Randerson (2017): *Attributing increased river flooding in the future: hydrodynamic downscaling reveals role of plant physiological responses to increased CO_2 is first order*. Poster. American Geophysical Union Fall Meeting, New Orleans, LA. Dec 15.

Fowler, M.D. and M.S. Pritchard (2017): *Using observed MJO-modulation of tropical cyclone activity to test a downscaling framework with potential for climate change analysis*. Oral presentation. Graduate Climate Conference, Woods Hole, MA. Nov. 11.

Fowler, M.D., M.S. Pritchard, and G.J. Kooperman (2016): *Assessing the Impacts of Central Valley Irrigation on Downstream Precipitation in the Irrigation-Enabled Community Earth System Model*. Oral presentation. American Geophysical Union Fall Meeting, San Francisco, CA. Dec 16.

Fowler, M.D., M.S. Pritchard and G.J. Kooperman (2016): *Assessing the Impacts of Indian and Californian Irrigation on Non-Local Precipitation in the Irrigation-Enabled Community Earth System Model*. Oral and poster presentation. U.S. Department of Energy Regional & Global Climate Modeling (RGCM) Program – Principal Investigators Meeting. Nov 29.

Fowler, M.D. and G. Izzi (2014): *Assessment of Heat Related Casualties in Chicago.* Oral presentation. NOAA Hollings Science and Education Symposium**.** July 29.

AWARDS AND HONORS

Andrew Slater Award **2019**
Best student or post-doc presentation at the NCAR Land Model Working Group Meeting 2019

1st Place Student Poster Presentation **2018**
AMS Annual meeting – 6th Symposium on the Madden-Julian Oscillation and Sub-Seasonal Monsoon Variability

Honorable Mention **2017**
National Science Foundation Graduate Research Fellowship

Outstanding Undergraduate Award **2014**
Department of Atmospheric Sciences, Texas A&M University

Hollings Scholar **2013-2014**
National Oceanic and Atmospheric Administration

RESEARCH EXPERIENCE

University of California – Irvine **Irvine, CA**
Thesis projects
Madden-Julian Oscillation modulation of tropical cyclone genesis *2017-2019*

- Developed a new downscaling methodology to assess MJO modulation of TC genesis in the West Pacific

Attributing streamflow changes in the future *2017-2019*

- Examined the impact of plant-physiological responses to increased CO_2 on future flood frequency and seasonal streamflow cycles in comparison to the role of radiatively-driven temperature and precipitation changes
- Large datasets generated for four 30-year sensitivity experiments of daily runoff downscaled to global 0.25˚ river runoff through CaMa-Flood
- Analysis of data required heavy use of both Python and MATLAB, including management of big data through parallel loops

Impacts of irrigation on non-local precipitation *2015-2017*

- Ran and modified a series of Community Earth System Model (CESM) experiments with irrigation to determine the effect of local irrigation in modifying non-local hydroclimate
- Focus placed on California's Central Valley and the Indian subcontinent
- Developed a bash script for easily running large ensembles of simulations without rebuilding the climate model each time

National Weather Service – Chicago **Romeoville, IL**
Hollings Scholar, Advisors: Gino Izzi and Eric Lenning
Heat-related casualties in Cook County *June-July 2014*

- Assessed the current heat warning system in Cook County in terms of avoiding heat-related fatalities reported by local hospitals
- Developed an alternative method of measuring and warning of heat stress in coordination with meteorologists at the office

Texas A&M University **College Station, TX**
Undergraduate student researcher, Advisor: Kenneth P. Bowman
Diurnal cycle of precipitation in tropical cyclones *2012-2014*

- Investigated the diurnal cycle of rainfall in tropical cyclones by utilizing the IBTrACS database in conjunction with TRMM satellite measurements of precipitation

TEACHING EXPERIENCE

University of California – Irvine **Irvine, CA**
Teaching Assistant

ESS5: The Atmosphere	Spring 2019
ESS1: Introduction to Earth System Science	Fall 2018
ESS116: Data Analysis	Spring 2018, 2015
ESS19: Modeling the Earth System	Winter 2017
ESS16: Climate Change	Fall 2016

C2 Education **Southlake, TX**
Tutor *Jan-May 2015*

Texas A&M University **College Station, TX**
Meteorology Help Desk *2013-2014*

LEADERSHIP AND OUTREACH

zotCAMS: Student Chapter of the American Meteorological Society at University of California – Irvine
Secretary, Apr 2017 – Jun 2019

NASA DIRECT-STEM Buddy
Contact point to visiting Cal-State LA students, Jun 2016, Aug 2017, & Aug 2018

School of Physical Sciences Undergraduate Mentorship Program (PSUM)
Mentor to two students at UCI, Oct 2016 – August 2017

Water UCI Middle School Water Conservation Challenge
UCI representative in multiple middle school science classes to help students develop new water conservation ideas, Feb-Mar 2017

CERTIFICATES AND WORKSHOPS

American Meteorological Society (AMS) Summer Policy Colloquium *2018*

Certificate of Mentoring Excellence *2017*

TECHNICAL SKILLS

- Scripting: advanced in MATLAB and Python; proficient in bash scripting and Linux OS; familiar with Fortran and NCL
- Models: experience running/modifying Community Earth System Model (CESM) and the Community Land Model (CLM); experience running the Catchment-Based Macroscale Floodplain Model (CaMa-Flood)
- Supercomputers: experience running on NERSC (Cori, Edison), and XSEDE (Stampede, Stampede2) machines

ABSTRACT OF THE DISSERTATION

Understanding how irrigation, plant physiology, and the Madden-Julian Oscillation shape regional water cycles and their extremes

By

Megan Devlan Fowler

Doctor of Earth System Science

University of California, Irvine, 2019

Associate Professor Michael S. Pritchard, Chair

The water cycle is one of the most fundamental building blocks of the earth system; without it, life would cease to exist, but its extremes pose a threat to both economies and ecosystems. It is thus especially important to understand the hydrologic cycle in as much depth as possible, including how human actions are already shaping it and how it could change in the future. In that vein, this dissertation addresses three distinct topics – how irrigation has altered precipitation; how plant-physiological changes in response to rising CO_2 can alter future flooding and streamflow; and how the Madden-Julian Oscillation (MJO) modulates tropical cyclones (TCs) in the West Pacific.

The first main chapter of this dissertation (Chapter 2) assesses non-local hydroclimate responses to irrigation in India, using an ensemble hindcast approach aimed at clarifying the ongoing debate in the literature about the robustness of forced water cycle responses relative to high levels of atmospheric internal variability. The results suggest a strong sensitivity to the initial synoptic condition, with separate non-local hotspots responding to

irrigation differently (but robustly) under different initial conditions. This argues that chaos plays a major role such that even heavy irrigation such as that over India has difficulty manifesting as strong, robust non-local water cycle responses. On longer time scales and across ensembles, the Meiyu-Baiu rainband region is highlighted as having a potentially robust non-local irrigation-induced precipitation signal, opening new questions.

In my second study (Chapter 3), I investigate streamflow changes as driven by (1) atmospheric responses and (2) plant-physiological responses to rising CO_2. A series of four modeling experiments help isolate these two response pathways and their combined effects, revealing that the plant physiological driver is actually of first order importance to projections of future flooding and streamflow. This is especially true in the tropics, where river discharge increases are controlled almost exclusively by the plant response in the Amazon, Parana, Congo, and Yangtze. This adds to a growing recognition in our field that profound changes in regional water cycles can occur even without warming-induced changes of precipitation as a result of how the terrestrial biosphere adapts to increased CO_2.

The final project (Chapter 4) seeks to better understand the mechanisms through which the MJO, a slow-moving tropical weather pattern, modulates West Pacific TCs. How, where, and even if the MJO modulates tropical cyclones is unresolved in this region, despite the fact that it is especially prone to human vulnerability from both high levels of current TC activity and future MJO amplification. Through a novel downscaling strategy that creates thousands of synthetic cyclone tracks for each phase of the MJO, I reveal two previously un-

emphasized but distinct stationary modes in opposite portions of the West Pacific basin that are modulated out of phase with one another. The South China Sea region is particularly responsive to the oscillation, driven by a transient combination of dynamic and thermodynamic factors. This adds to a decades long debate about what mechanisms mediate MJO-TC modulation in nature and identifies new subregions that will be particularly important to focus on in the coming decade, towards advancing understanding of how MJO amplification may affect TC hazards in a future climate.

Chapter 1

Introduction

Human actions have modified the natural hydrologic cycle for centuries, and the influence of our actions will only continue to grow in the face of ongoing climate change. This dissertation spans three topics that, despite focusing on separate issues, are each germane to advancing our understanding of how precipitation and hydrometeorological extremes can be influenced by people – be it through irrigation (Chapter 2), plant physiological responses to rising CO_2 (Chapter 3), or through a globally important tropical wave that is predicted to intensify in coming decades (Chapter 4). Some of the overarching connections between these topics is introduced briefly below in Section 1.1, followed by individual motivations for each chapter in Sections 1.2-1.4 as they are each interesting in their own right.

1.1 Research overview

In Chapter 2, I focus on the expansion of irrigation, which has had a profound impact on landscapes around the world, altering surface energy and moisture fluxes in ways that can heavily influence the regional hydroclimate [*de Vries*, 1959; *Boucher et al.*, 2004; *Douglas et al.*, 2006; *Kueppers et al.*, 2007; *Sacks et al.*, 2009; *Puma and Cook*, 2010; *Harding and*

Snyder, 2012]. Today, despite only 40% of all farmland being irrigated, the practice is responsible for 70% of the total water withdrawn for agriculture and nearly 90% of all global consumptive water use [*Doll and Siebert*, 2002; *Harding et al.*, 2015; *Meier et al.*, 2018]. As population continues to rise, the amount of irrigated area will likely need to increase alongside it to meet growing food demands, necessitating a full understanding of the practice's effects, especially with respect to water re-distribution through atmospheric pathways. Though a large number of studies have attempted to answer the question of how precipitation is linked to irrigation [*Barnston and Schickedanz*, 1984; *Lohar and Pal*, 1995; *Segal et al.*, 1998; *Pielke et al.*, 2007; *Saeed et al.*, 2009; *DeAngelis et al.*, 2010; *Puma and Cook*, 2010; *Lo and Famiglietti*, 2013; *Sorooshian et al.*, 2014; *Alter et al.*, 2015; *Huang and Ullrich*, 2016; *Pei et al.*, 2016; *de Vrese et al.*, 2016], our understanding of the relationship between the two, especially non-locally, remains uncertain for a number of critical regions (see Section 1.2). I will thus investigate the response of remote mean precipitation to irrigation in northwestern India and, more briefly, California's Central Valley.

The water cycle can also be heavily affected by other parts of the biosphere that are indirectly modulated by human actions through our emissions of greenhouse gases. Plants, for example, are thought to respond to elevated CO_2 concentrations by reducing their stomatal conductance and increasing their leaf area [*Ainsworth and Long*, 2004; *De Kauwe et al.*, 2013], both of which could have important ramifications on terrestrial hydrology through their effects on evapotranspiration and soil moisture. Those changes have the potential to play a role in driving streamflow and flood changes [*Gedney et al.*, 2006], but the importance of these physiological effects remains uncertain (see Section 1.3). Chapter 3

thus seeks to better understand the ability of future plant-physiological changes to alter river flows relative to radiatively driven changes in precipitation and temperature.

Tropical cyclones (TCs) and their future changes with global warming also remain uncertain at regional scales [*Christensen et al.*, 2013], despite overall agreement at the global scale that their average intensity will rise even if their numbers do not [*Knutson et al.*, 2010; *Christensen et al.*, 2013]. In part, regional agreement has been hampered by the inability of most global climate models (GCMs) to capture important tropical wave patterns that are known to modulate cyclogenesis [*Frank and Roundy*, 2006; *Christensen et al.*, 2013; *Wu and Takahashi*, 2018; *Zhao and Li*, 2018]. One particularly important wave, the Madden-Julian Oscillation (MJO), is well known to modulate TC formations in the West Pacific [*Liebmann et al.*, 1994; *Kim et al.*, 2008; *Camargo et al.*, 2009; *Huang et al.*, 2011; *Klotzbach*, 2014], but the exact mechanism behind that control is still debated (see Section 1.4). Signs of MJO amplification in GCM experiments [*Arnold et al.*, 2014, 2015; *Adames et al.*, 2017; *Maloney et al.*, 2019] suggest the importance of properly understanding the relationship behind MJO-based TC variability in today's climate to better constrain future impacts of intensification. I will thus investigate the sensitivity of subregional cyclogenesis to the MJO in today's climate through a series of confidence building tests that aim to improve our understanding of the phenomenon.

1.2 Irrigation and its ability to modify the climate

Global population has risen by more than 350% over the last century, and although our peak growth rate was reached in the 1960s, the upward trend is expected to continue

towards 11 billion by the end of the century [*Roser et al.*, 2019]. The dramatic rise in population has already spurred a number of adaptations to meet growing food and water demands, including those in the agricultural sector that have altered the terrestrial water cycle through the application of large volumes of water to the surface. Irrigation now accounts for the majority of global consumptive water use [*Doll and Siebert*, 2002; *Harding et al.*, 2015] through re-routing it from rivers or pumping it to the surface from underground aquifers, both of which can have serious impacts on local ecosystems (i.e., land subsidence resulting from over-pumping, or diversions altering low and high flows critical to ecosystem health). The addition of that water to the land surface also has the potential to significantly alter atmospheric moisture content and, more importantly, subsequent precipitation patterns [*Lo and Famiglietti*, 2013; *de Vrese et al.*, 2016].

One of the most common tools to assess the effects of an environmental shift such as the expansion of irrigation is GCMs, but human activities and agricultural practices have historically not been included in these models. As a consequence, many studies that have previously assessed the ability of irrigation to alter precipitation within a modeling framework have had to rely on inconsistent modifications of the model source code that vary in how irrigation is applied (above vs. below ground; concentrated in time vs. spread evenly over a day, etc.) rather than using a thoroughly reproducible approach integrated into the GCM itself. The result has been a series of mixed conclusions on precisely how irrigation can impact the simulated atmosphere based on the variety of choices made in how to represent this phenomenon [i.e., *Puma and Cook*, 2010; *Lo and Famiglietti*, 2013; *de Vrese et al.*, 2016; *Huang and Ullrich*, 2016].

The precipitation response to irrigation is typically one of the lesser agreed upon signals, whether local to the center of irrigation or non-locally through moisture transport and teleconnections. Although the topic has been frequently studied, differing conclusions have been drawn in each case [*Barnston and Schickedanz*, 1984; *Cook et al.*, 2006; *Saeed et al.*, 2009; *Puma and Cook*, 2010; *Kueppers and Snyder*, 2012; *Lo and Famiglietti*, 2013; *Huang and Ullrich*, 2016; *Selman and Misra*, 2016; *de Vrese et al.*, 2016]. Recently, a few studies have suggested that irrigation-enhanced soil moisture could alter remote monsoon precipitation. *Lo and Famiglietti* [2013] noted this effect for the North American Monsoon system when irrigation was applied in the Central Valley of California, while *de Vrese et al.* [2016] note similar impacts on the Asian Monsoon for South Asian irrigation. In both locations, however, significant disagreement between other models and studies calls into question the robustness of this link [*Saeed et al.*, 2009; *Puma and Cook*, 2010; *Sorooshian et al.*, 2014; *Huang and Ullrich*, 2016].

Internal variability may offer an explanation for the spread in previous studies on how irrigation can impact non-local rainfall [*Thiery et al.*, 2017]. Precipitation is an especially noisy part of the atmosphere, one that is prone to high levels of natural variability [*Deser et al.*, 2012, 2014]. It is thus perhaps unsurprising that irrigation-induced changes in rainfall are so much less certain than those in temperature, especially at large distances from the anthropogenic moisture source. Ensembles can help allay the risk of internal variability dominance, but this approach has rarely been employed due to the high computational cost of running multiple instances of the same experiment on long timescales.

Both *Lo and Famiglietti* [2013] and *de Vrese et al.* [2016] use only a single long-running simulation of irrigation, but a small 5-member ensemble of 30 years from *Thiery et al.* [2017] highlights the importance of assessing more than just a single realization of the climate system, especially when interpreting irrigation's effects on precipitation. I will thus use an ensemble approach that includes a large 60-member sample. Unlike *Thiery et al.* [2017], irrigation is only allowed on the Indian subcontinent so as to isolate its potential influence on the non-local hydroclimate. To make such a large ensemble feasible, I focus on hindcast experiments that span just 45 days each – a significant departure from the multi-decadal experiments assessed in *de Vrese et al.* [2016] and commonly employed by others. Any non-local effects of irrigation should be well established after more than a month and, if robust, their transient set-up should also be observable near the beginning of the simulations through clear teleconnection patterns observable in high-frequency output.

Research Objectives

Chapter 2 broadens the scope of past studies that have attempted to quantify the ability of irrigation to alter non-local precipitation, with a focus on the heavily irrigated Indian subcontinent. Unlike previous studies, I will use a novel hindcast ensemble approach that (1) helpfully minimizes the potential role of internal variability, and (2) enables the search for teleconnection mechanisms responsible for remote rainfall changes. The initial conditions used for these simulations span a range of dates in May, allowing for robust sampling of multiple synoptic conditions and focusing on the monsoon onset period, which is hypothesized to have an especially sensitive atmosphere to changes in the land surface.

Brief consideration is also given to the Central Valley region of California to confirm some of the signals associated with irrigation, but our primary finding of insignificant non-local precipitation effects there (in line with *Sorooshian et al.* [2014] and *Huang and Ullrich* [2016]) relegates most of the discussion to Appendix A.

Through these experiments, I also uncover limitations on the land model that ultimately inhibit irrigation's ability to moisten the soil. I will therefore explore an approach that effectively doubles the amount of water being applied each day, which helps identify consistently amplifying signals that emerge in the non-local hydroclimate as a result of local irrigation. Continued disparity between these results and those of others suggests the need for better representing irrigation practices in GCMs, in addition to future studies across a wide array of irrigation-enabled models to fully understand the capacity of irrigation to alter the non-local hydrologic cycle.

The following questions in particular are addressed in this study:

- Is there a significant connection between non-local precipitation and irrigation over the Indian subcontinent as suggested by *de Vrese et al.* [2016], or is the signal swamped by internal variability, consistent with suggestions from *Thiery et al.* [2017]? If one does exist, over what time scales is the teleconnection observable?
- What mechanisms are responsible for non-local hydroclimate changes induced by the addition of irrigation? As a further test of credibility, are they robust to varied levels of irrigation intensity?

- Based on details revealed through high frequency sampling of the transient response, is the irrigation module in the land model realistic in terms of its impact on the soil column and overlying atmosphere?

This chapter was published in the *Journal of Hydrometeorology* and is reproduced here with the permission of the American Meteorological Society:

> **Fowler, M.D**., M.S. Pritchard, and G.J. Kooperman, (2018): Assessing the Impact of Indian Irrigation on Precipitation in the Irrigation-Enabled Community Earth System Model. *J. Hydrometeor.,* **19**, 427–443, https://doi.org/10.1175/JHM-D-17-0038.1.

1.3 Future changes in streamflow and river flooding

More than 200,000 people around the world were killed by floods between 1970 and 2013 [*UNISDR*, 2015]. But as the climate continues to change in the coming decades, variations in the frequency and intensity of floods are likely to occur as well. The Fifth Assessment Report of the International Panel on Climate Change (IPCC) notes that there is now medium confidence on flood frequency changes [*Jiménez Cisneros et al.*, 2014], an uptick from the Special Report on Extremes (SREX) that assigned only low confidence to projected frequency and intensity shifts a few years earlier [*Seneviratne et al.*, 2012]. The still-limited certainty, though on the rise, is partly related to the scarcity of global-scale flood studies [*Seneviratne et al.*, 2012; *Kundzewicz et al.*, 2014], with many that focus only on a single model/iteration. But perhaps the biggest barrier to higher confidence in flood projections lies in the tools themselves that are used to make these estimates. Precipitation estimates

from GCMs are often biased, with a tendency to over-produce light rain rates [*Stephens et al.*, 2010] that ultimately contribute to systematic uncertainty in future projections of flood frequency and severity. But precipitation is not the only mechanism that causes flooding; soil moisture and land surface changes are equally important to account for [*Ivancic and Shaw*, 2015; *Woldemeskel and Sharma*, 2016].

Vegetation cover acts as a crucial link between the land surface and the overlying atmosphere in the hydrologic cycle; the largest portion of terrestrial evapotranspiration (ET) comes from plant transpiration [*Lemordant et al.*, 2018], which can then be recycled as precipitation. Meanwhile, beneath the surface, plants exert a major control on soil moisture: they draw up water through their roots and lower the amount that remains in the soil column as a result. The plant-physiological traits that control these functions, however, may face a series of changes in the future that could significantly alter the hydrologic cycle, regardless of atmospherically driven changes in precipitation that suggest regionally more frequent/intense rainfall [*Sun et al.*, 2007; *Allan and Soden*, 2008; *Zhang et al.*, 2013; *Kooperman et al.*, 2016].

A series of Free Air Carbon Enrichment (FACE) experiments have revealed robust responses of plants to elevated CO_2 [*Ainsworth and Long*, 2004; *De Kauwe et al.*, 2013]. Plants with the C3 photosynthetic pathway in particular have been observed to respond most strongly to the perturbation, reducing the amount of time their stomata are open during photosynthesis and thus decreasing the amount of water lost during the process via transpiration and increasing their water use efficiency (WUE) [*Ainsworth and Long*, 2004].

As a consequence, soil moisture would likely increase: with higher efficiency comes a decreased need for roots to draw up moisture at the previous rate. As a result, even if there were no concurrent warming induced shifts in precipitation, soil saturation could be reached more readily during a storm, thereby limiting infiltration and causing more frequent and/or larger runoff. These changes also have the potential to increase annual streamflow statistics and more extreme river flood events.

If this were the only mechanism by which plants responded to heightened CO_2, decreased ET over land could be expected as a result. But a second effect of the elevated concentrations may act in part to counteract these shifts in ET and soil moisture by increasing the amount of vegetation present. This "carbon fertilization" effect has been observed in FACE experiments to increase plant productivity, increasing the leaf area index (LAI) and vegetation cover of a region in response to higher atmospheric CO_2 [*Ainsworth and Long*, 2004]. The additional stomata in the expanded vegetation may thus result in an increase or no net change of ET even though leaf-level WUE has increased, eliminating any potential increases in antecedent soil moisture conditions. But the extent to which this effect occurs remains debated [*Reich et al.*, 2014; *Obermeier et al.*, 2017; *Hovenden and Newton*, 2018]. Tree ring studies assessing ambient increases in CO_2, for example, have found evidence of increased WUE but no concurrent increases in plant growth [*Peñuelas et al.*, 2011; *van der Sleen et al.*, 2015; *Norby et al.*, 2016].

The balance between these two drivers and the cumulative effects of rising CO_2 on plant physiology and growth remain uncertain in observations, which has complicated analysis

of their role in projections of future river flow. Existing FACE sites have been primarily located in mid-latitude temperate forests, which are likely *not* representative of vegetation responses in tropical or boreal regions [*Hickler et al.*, 2008]. There has been a recent effort to expand into a wider range of climate zones [*Norby et al.*, 2016], but it will be a number of years before a sufficiently long record can be used from these locations to understand the wide array of possible plant responses. But the issue of record length is not unique to these newer sites; the process of maintaining FACE experiments for extended periods of time is expensive and time consuming, and has thus only been possible at a few locations. But those that have remained operational for more than 15 years suggest the critical importance of doing so. From a 16-year study, the effects on net primary production are found to decline under extreme weather conditions compared to average ones [*Obermeier et al.*, 2017], while a 20-year experiment in Minnesota finds that C3 plants actually stop increasing productivity after about 12 years; C4 plants began to expand after that point, representing a significant departure from previous findings [*Reich et al.*, 2018].

Generalizing the varied responses and constantly evolving knowledge from relatively small-scale site level experiments for use in global scale models has remained a challenge. Land surface models (LSMs) thus exhibit a large spread in their behavior, stemming from a number of factors including different parameterizations of stomatal responses to CO_2, the treatment of canopy interception/evaporation, and the limited ability of soil moisture to modify that relationship [*De Kauwe et al.*, 2013]. But despite disagreements on just how strong the CO_2 response should be in LSMs, its effects on the hydrologic cycle have been investigated somewhat frequently from the standpoint of mean changes, with relatively

consistent trends. A doubling of CO_2, for example, is expected to cause a global average increase in mean runoff of 5-6% [*Leipprand and Gerten*, 2006; *Betts et al.*, 2007].

River discharge accumulates all the runoff in a basin as the water moves downstream, so that the physiological effect on runoff may not be a direct corollary for the impacts felt along the river bank. On this topic, there has been significantly more disagreement. One of the first studies to consider the impacts of rising CO_2 on streamflow used a series of calculations rooted in the water balance equation to argue that precipitation will always exert a stronger force than ET changes, but relied on numerous simplifying assumptions to reach that conclusion, including no allowances for variation based on climate zone or photosynthetic pathway [*Wigley and Jones*, 1985]. *Gedney et al.* [2006] was the first to suggest that a detectable signal was already present in global streamflow records based on a modeling attribution study, but their findings were almost immediately criticized. In addition to using a discharge record that relies on controversial back-filling [*Peel and McMahon*, 2006], their modeling approach ignored the carbon fertilization effect entirely, likely over-estimating the importance of increased WUE [*Piao et al.*, 2007; *Gerten et al.*, 2008]. When this effect was included, precipitation changes were found to be the most likely explanation for any observed increases in streamflow [*Piao et al.*, 2007; *Gerten et al.*, 2008; *Trenberth*, 2011]. The overall consensus then is that there is not yet a detectable physiological signal in 20th century streamflow, although a future trend may yet emerge.

The effect of plant-physiological changes on future weather and climate extremes is a topic that has only recently begun to receive attention. It has been suggested to reduce drought

severity by increasing soil moisture [*Swann et al.*, 2016] and also to play a large role in increasing the most extreme runoff rates [*Kooperman et al.*, 2018b]. But extreme runoff alone cannot determine the human impacts that will be felt as a result of plant-physiological changes on the water cycle. I thus assess seasonal streamflow characteristics and more extreme long-term flood events to help bridge that gap, highlighting the importance of including this effect in future projections of both. Streamflow also has the advantage of being more readily observable than raw runoff, suggesting a useful proxy for better constraining the strength of the physiological effect in observations.

Research Objectives

Chapter 3 investigates the individual abilities of radiatively-driven changes in precipitation/temperature and physiologically-driven changes in transpiration/LAI to alter future flood frequency and seasonal streamflow. The work pairs output from the four GCM simulations in *Kooperman et al.* [2018b] with a hydrodynamic model capable of predicting high-resolution river discharge including transient riverbed inundation dynamics. Extreme value statistics are then used to estimate flood return periods and magnitudes. In addition to these high-impact events, radiative and physiological changes in more readily observable annual streamflow extremes (peak and low flows) are assessed.

Specific research questions addressed in this work include:

- How large of an impact does the plant-physiological effect have on century-scale flood extremes? On more observable seasonal streamflow?

- Can particular regions of the globe be identified where streamflow could be used as a proxy for the physiological response, as initially suggested by *Gedney et al.* [2006]?

This chapter is currently under review at *Nature Climate Change* as:

> **Fowler, M.D.,** G.J. Kooperman, J.T. Randerson and M.S. Pritchard (*in review at Nat. Clim. Change*; 2019): Identifying the effect of plant-physiological responses to rising CO_2 on global streamflow.

1.4 MJO modulation of tropical cyclones in the West Pacific

TCs are responsible for massive amounts of damage in terms of both fatalities and economic losses in the West Pacific, which is home to more of these storms annually than any other ocean basin [*Zhao et al.*, 2015a; *Ramsay*, 2017]. While the Atlantic experiences an average of 6.4 hurricanes a year, the northern West Pacific faces more than twice as many at 16.5 annually [*Landsea and Delgado*, 2017]. It is thus especially important to understand the factors that drive TC formations here, though that task has been historically difficult. That can be linked in part to the inability of most GCMs to reasonably simulate important tropical waves that play a role in modulating some of the "necessary but not sufficient" factors for cyclogenesis including high relative humidity, low vertical wind shear, andwarm sea surface temperatures [*Christensen et al.*, 2013; *Wu and Takahashi*, 2018; *Zhao and Li*, 2018].

One such wave with implications for cyclogenesis is the MJO: a quasi-periodic, global, intraseasonal oscillation with a period of roughly 30-60 days [*Zhang*, 2005; *Krishnamurti et*

al., 2013]. Originally discovered by *Madden and Julian* [1971, 1972], the oscillation can be described as a packet of organized convection that makes its way through the tropics from the Indian to West Pacific Oceans in a series of phases defined by its location. It is often noted in observations by positive anomalies of outgoing longwave radiation (OLR) with nearby suppressed convection (negative OLR anomalies). These large cloud clusters are coupled to wind anomalies that can affect weather patterns around the world as they move beyond the dying precipitation center over the Pacific and circumnavigate the globe. The MJO has thus been noted for its ability to have significant effects on cyclogenesis in almost all ocean basins, but especially in the northern West Pacific [*Liebmann et al.*, 1994; *Kim et al.*, 2008; *Camargo et al.*, 2009; *Huang et al.*, 2011; *Klotzbach*, 2014]. The oscillation also shows robust patterns of amplification as a result of global warming in state-of-the-art GCM experiments [*Arnold et al.*, 2014, 2015; *Chang et al.*, 2015; *Adames et al.*, 2017; *Wolding et al.*, 2017; *Maloney et al.*, 2019]. But before attempting to understand how the relationship between TCs and the intraseasonal oscillation could change in the future, it's necessary to first understand their connection today.

Despite its importance to West Pacific cyclogenesis, the exact mechanism through which the MJO modulates TC formations in the basin remains debated. Studies that have relied on the Genesis Potential Index [*Emanuel and Nolan*, 2004], which quantifies the environmental favorability for TC genesis, suggest that the thermodynamic effects associated with the MJO, most notably increased relative humidity, are the primary cause for observed controls on cyclogenesis [*Camargo et al.*, 2009; *Huang et al.*, 2011; *Zhao et al.*, 2015a, 2015b; *You et al.*, 2018; *Zhao and Li*, 2018]. But a number of other studies, including those that assess

high-resolution model output and other genesis metrics, suggest a leading role of dynamic factors instead, including shear and vorticity changes [*Liebmann et al.*, 1994; *Maloney et al.*, 2000; *Hall et al.*, 2001; *Tippett et al.*, 2011; *Wang and Moon*, 2017; *Moon et al.*, 2018].

The MJO-TC modulation is further complicated by the many methodological choices that have been made in how to determine that relationship, which have not only made it difficult to compare their findings, but are also responsible for the lack of a clear consensus on which phases of the MJO are beneficial for TC formations versus those that tend to inhibit them at basin scales. *Li and Zhou* [2013], for example, suggest that Phases 1 and 2 are favorable for West Pacific TCs based on an index that uses only OLR to define the MJO. Studies that rely on the Realtime Multivariate MJO (RMM) index instead, developed by *Wheeler and Hendon* [2004], tend to suggest the later periods of the MJO as most favorable – ranging from Phase 5-8 [*Klotzbach*, 2014; *Klotzbach and Oliver*, 2015b; *You et al.*, 2018]. Studies that rely on observations have also been limited by small sample sizes, motivating large spatial and temporal aggregation; the co-occurrence of TC genesis with individual MJO phases, both relatively rare events individually, remains limited even in records that span multiple decades. Modeling studies, for their part, have attempted to fill this gap but require such a high resolution to properly resolve both the MJO and TCs that they remain too expensive to run on century timescales. In light of these limitations on the current state of knowledge regarding the MJO-TC modulation, I develop a new downscaling strategy that creates thousands of synthetic TC tracks in each phase of the MJO as defined by both the RMM index and one relying solely on OLR. This serves as an independent test of previous findings regarding the ability of the MJO to modulate cyclogenesis in the West Pacific,

which is further confirmed by a genesis potential analysis, which reveals that *both* dynamic and thermodynamic factors are critical for enhancing TC formations, especially in the South China Sea region.

Research Objectives

Chapter 4 intends to expand the conversation surrounding the ways in which the MJO can alter TC formations in the West Pacific. The two indices used to define the oscillation serve as a confidence building test to determine robust signals of MJO-TC modulation in the basin, which should be insensitive to reasonable choices of how to define the MJO. A model developed by Kerry Emanuel at MIT is then used to seed thousands of synthetic TC tracks in a coupled ocean-atmosphere framework, with environmental conditions characteristic of single phases of the MJO. This downscaling strategy aims to increase confidence in the TC modulation signal by avoiding spatial and temporal aggregation that may have obscured important regional details of the signal previously.

The expanded set of TCs generated by the MIT model suggests that contrary to previous assessments, enhanced cyclogenesis does not simply propagate eastward with the MJO but is instead favored in two distinct stationary geographic action centers – the South China Sea region and the West-Central Pacific, which are modulated out of phase with one another. Analysis of the Genesis Potential Index supports this pattern and suggests transient controls of reduced shear, increased potential intensity, and finally enhanced relative humidity for the western region.

The following research questions are addressed in this work:

- What is the nature of TC modulation by the MJO in the West Pacific, if viewed through an expanded set of synthetic TC tracks that avoids spatio-temporal smoothing?
- As a new test of credibility, are these findings robust to independent definitions of the MJO?
- What is the underlying mechanism behind MJO modulation of cyclogenesis in the West Pacific? How does it add to the debate about thermodynamic vs. dynamic control?

This chapter is in preparation as:

Fowler, M.D. and Pritchard, M.S. (*in prep.*.; 2019): Complex MJO modulation of West Pacific tropical cyclones revealed through regional hotspots with multiple transient controls.

1.5 Organization

Chapters 2, 3, and 4 are the research chapters as outlined above, which have either been published in or are currently under review in/being prepared for peer-reviewed journals. The only alterations of each have been for reformatting purposes. Chapter 5 concludes with a summary of the dissertation and suggestions for future work.

Chapter 2

Assessing the impact of Indian irrigation on precipitation in the irrigation-enabled Community Earth System Model

Adapted from:

Fowler, M.D., M.S. Pritchard, and G.J. Kooperman, 2018: Assessing the Impact of Indian Irrigation on Precipitation in the Irrigation-Enabled Community Earth System Model. *J. Hydrometeor.,* **19**, 427–443, https://doi.org/10.1175/JHM-D-17-0038.1.

© American Meteorological Society. Used with permission.

Abstract

Global climate models are beginning to include explicit treatments of irrigation to investigate the coupling between human water-use and the natural hydrologic cycle. However, differences in the formulation of irrigation schemes have produced inconsistent results, and thus the impact of irrigation on the climate system remains uncertain. To better understand the influence of irrigation on precipitation, we analyze simulations from the irrigation-enabled Community Land Model version 4 (CLM4) where irrigation is applied only over a region centered on India. The addition of irrigation to the land surface has the anticipated consequence of increasing evapotranspiration locally, despite issues revealed in CLM4 of unrealistically high partitioning of irrigation water to surface runoff and unrealistically fast water drainage through the soil column. These limitations highlight a need to observationally constrain and simultaneously optimize irrigation, runoff, drainage, and evapotranspiration. Non-local precipitation changes as a result of Indian irrigation during the pre-monsoon season are examined through a hindcast framework that reveals robust hydrologic teleconnections to parts of the Arabian Sea, Bay of Bengal, and Japan on short lead times, but with strong dependence on initial synoptic condition. On longer time-scales, many of these teleconnections to Indian irrigation are easily shrouded by internal variability, but a potential geographic action center remains over the Meiyu-Baiu rainband indicative of a non-local bridge mechanism. Many of the sensitivities identified here are distinct from other global models, emphasizing the need for carefully designed irrigation-intercomparison studies.

2.1 Introduction

Rapid population growth in the last century has led to numerous modifications of the hydrologic cycle to meet the growing food and water needs of the planet. One of the largest changes has come from the expansion of irrigation, which now represents 90% of global consumptive water use [*Harding et al.*, 2015]. Despite the large surface- and ground-water withdrawals that must occur to support this practice, parameterizations of irrigation have only recently been added to global climate models (GCMs), with mixed conclusions drawn about its effects on the simulated climate system [*Puma and Cook*, 2010; *Lo and Famiglietti*, 2013; *de Vrese et al.*, 2016; *Huang and Ullrich*, 2016]. Fully understanding such impacts will be necessary for interpreting the results from the next generation of GCMs to be used for coupled model intercomparison projects (CMIPs), which are likely to include irrigation as an anthropogenic modification of the natural water cycle.

Irrigation may interact with the climate system in a number of ways, some of which are better understood than others. One robust effect of irrigation is the lowering of near-surface temperatures, which occurs as a result of repartitioned surface fluxes that favor latent over sensible heat release [*de Vries*, 1959; *Barnston and Schickedanz*, 1984; *Selman and Misra*, 2016]. This process has been suggested to reduce a warm bias present in some GCMs [*Huang and Ullrich*, 2016] and to modulate regional circulations [*Lohar and Pal*, 1995; *Saeed et al.*, 2009; *de Vrese et al.*, 2016; *Thiery et al.*, 2017].

The effects of irrigation on simulated precipitation remain more heavily debated, in terms of both the location (local versus non-local) and sign of the change (increase versus

decrease). Studies that have analyzed the impacts of irrigation globally tend to find increases in precipitation in response to wetter soils, though this generalization masks important regional differences in the response [*Sacks et al.*, 2009; *Puma and Cook*, 2010; *de Vrese et al.*, 2016], as well as differences that arise among different models and resolutions [*Hohenegger et al.*, 2009; *Sorooshian et al.*, 2011; *Tuinenburg et al.*, 2014].

In some cases, irrigation may lead to local increases in rainfall due to enhanced moisture recycling [*Saeed et al.*, 2009; *de Vrese et al.*, 2016]. In others, rainfall may increase through increased convective available potential energy (CAPE) and enhanced moist static energy, which can arise from the lower surface albedo caused by wetter soils, or a stronger greenhouse effect due to enhanced low-level atmospheric moisture [*Pal and Eltahir*, 2001]. Alternatively, irrigation may decrease local precipitation due to moistening and cooling of the lower atmosphere, which acts to increase stability and favor low-cloud formation rather than deep convection [*Cook et al.*, 2006; *Selman and Misra*, 2016]. Yet another possible outcome of irrigation is that local precipitation patterns do not change at all if the water is applied during a time that lacks the support of synoptic systems to provide the instability and/or lift needed for precipitation to form [*Barnston and Schickedanz*, 1984; *Kueppers and Snyder*, 2012].

The impacts of irrigation on *non-local* precipitation are far less studied than those that occur locally, in part because of the common use of regional climate models (RCMs) to study the links between enhanced soil moisture and the overlying atmosphere. While this approach allows for high resolutions and realistic orographic effects, it excludes potentially

important non-local feedbacks on large scales. The recent advent of GCMs with explicit irrigation schemes has thus emerged as a useful tool for studying potential links between local irrigation and non-local changes in the hydroclimate system. A recent pioneering study by *de Vrese et al.* [2016] has highlighted South Asia as a region of the world where local irrigation may significantly impact remote precipitation patterns through advective pathways; this same region is therefore chosen as the primary focus of this work using an independent modeling framework. An earlier GCM study of irrigation also suggested California's Central Valley as a region with potentially significant teleconnections to non-local precipitation [*Lo and Famiglietti*, 2013]. Although we focus our analysis on India, some results are tested for geographic resilience by using climatological simulations that isolate irrigation in the Central Valley. These are summarized in the Supplemental Information (Section A.2).

There is significant model disagreement in regards to the impacts of Indian irrigation. *Puma and Cook* [2010] find local decreases in precipitation as a result of irrigation, while *Saeed et al.* [2009] find both increases and decreases in rainfall across the region. It has been suggested that, like aerosols, irrigation in south Asia has the potential to modify the summer monsoon circulation and local precipitation via cooling and a weakening of the land-sea temperature gradient [*Lohar and Pal*, 1995; *Saeed et al.*, 2009; *Tuinenburg et al.*, 2014; *de Vrese et al.*, 2016; *Thiery et al.*, 2017]. A recent study using an irrigation-enabled GCM found that irrigation in the Indian region may also significantly impact non-local precipitation, leading to increased rainfall in parts of the Arabian Peninsula, Africa, and even Australia [*de Vrese et al.*, 2016]. Similar disagreement amongst model predictions

have also been found in the western United States, where *Lo and Famiglietti* [2013] suggested that Californian irrigation can increase summer precipitation in the southwestern United States by as much as 15%, while a few recent studies have found only minor rainfall changes elsewhere [*Sorooshian et al.*, 2014; *Huang and Ullrich*, 2016].

The wide discrepancy among studies that use different model types, resolutions, and even irrigation schemes suggests the need for additional studies addressing the impacts of irrigation on non-local precipitation. The aim of this paper is therefore to broaden the range of GCMs that have addressed this topic by using an irrigation-enabled version of the Community Earth System Model (CESM) to assess the impacts of Indian irrigation on precipitation. Our experiment design will also aim to test hypotheses for bridge mechanisms that have been proposed to connect local irrigation with non-local hydroclimatic changes, such as the advective pathway suggested by *de Vrese et al.* [2016].

Section 2.2 of this chapter details the model set-up used in our experiments as well as the methods used to analyze the resulting output. Section 2.3 discusses the impacts of Indian irrigation on both the local and remote climate system, as well as an assessment of the irrigation scheme's realism. Section 2.4 concludes the paper with a summary of the main findings and potential pathways forward.

2.2 Methods

We use the National Center for Atmospheric Research CESM framework, which couples the Community Atmosphere Model version 5 (CAM5, Neale et al. [2012]) with the Community

Land Model version 4 (CLM4, *Lawrence et al.* [2011]). Simulations are performed at a horizontal resolution of 0.9˚x1.25˚ and sea surface temperatures (SSTs) are prescribed to climatological values to minimize internal variability.

We make use of an irrigation module embedded within CLM4, described by *Levis and Sacks* [2011]. Although this scheme does not include all the effects of irrigation – such as the ability for leaf area indices to respond – it does include the first order effect of removing water limitations on transpiration. The existing crop plant functional type (PFT) is subdivided into both an irrigated and non-irrigated fraction within each grid cell based on a map of irrigated areas from *Siebert et al.* [2007]. Then, to avoid water stress, the land model makes a check once a day at 6 AM local time to determine if irrigation is required. If it is, water is applied to the surface (bypassing interception) from 6-10 AM local time. The decision to irrigate is based on the presence of non-zero crop leaf area and a soil moisture level that is limiting for photosynthesis. The latter condition is based on *Eq. 2.1*, which calculates a target soil moisture to maintain optimal plant growth:

$$w_{target,i} = (1 - F_{IRRIG})w_{o,i} + F_{IRRIG} * w_{sat,i} \qquad (2.1)$$

where for each soil layer *i*, w_o is the minimum soil moisture required for zero water stress, w_{sat} is the soil moisture at saturation, and F_{IRRIG} is an empirically derived constant tuned so that global mean irrigation rates match observations from the year 2000 [*Levis and Sacks*, 2011; *Leng et al.*, 2013]. It has been suggested that tuning the empirically derived F_{IRRIG} in *Eq. 1* leads to more realistic irrigation water demand regionally, relative to observational

constraints [*Leng et al.*, 2013, 2014, 2015]. In this study, the parameter is reduced from its default value of 0.70 to 0.55 to bring the parameter more in line with the findings of *Leng et al.* [2015].

The CLM4 irrigation scheme was designed to implement irrigation globally, but in this study we want to isolate the impacts of one region's irrigation on precipitation elsewhere. We therefore modify the input surface data file to allow irrigated crops only within a domain centered over India (the large rectangle in *Fig. 2.1*), while the pre-existing crop PFT is completely non-irrigated outside of this target region.

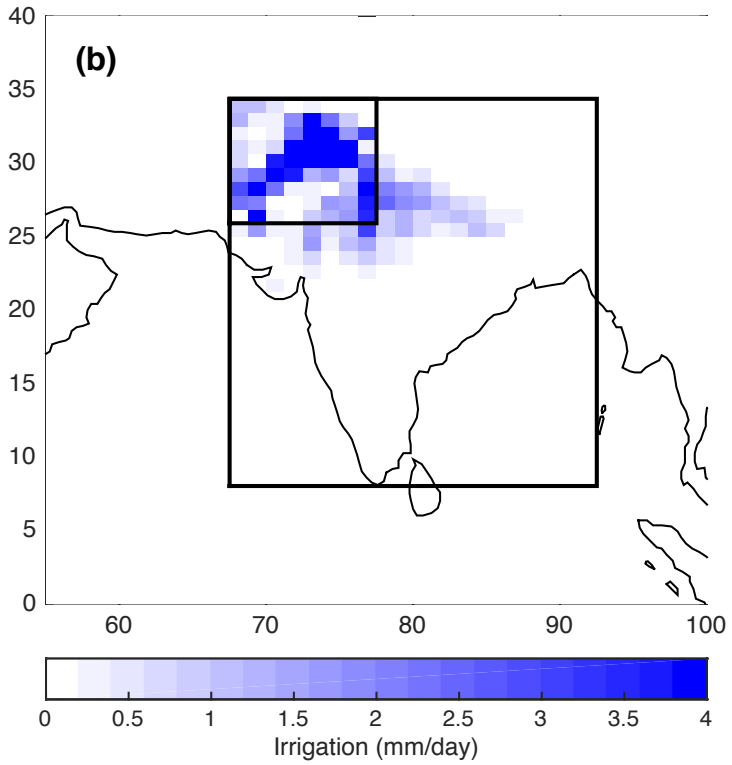

Figure 2.1: *Magnitude and location of irrigation-induced surface water source over India. Shading shows the average irrigation amount (mm/day) over the full 45-day period for the 60-member IRRIG ensemble mean. The inset rectangle outlines the "heavily irrigated" region.*

To reduce natural variability and increase the potential of identifying statistically significant impacts of irrigation, we conduct a wide ensemble of hindcasts and focus first on short lead times, before noise can mask the detectability of an irrigation-induced signal. We generate a set of 60-member 45-day hindcast ensembles for both the control and irrigation experiments, all of which are initialized in mid-May. This minimizes computational expense while targeting the monsoon onset period, during which the atmosphere is expected to be more vulnerable to soil moisture modifications than during the more externally forced active phase of the monsoon [*Tuinenburg et al.*, 2014]. The hindcast approach implicitly assumes that the hydrologic response to irrigation is both fast and atmospheric, which is also a reasonable expectation in an SST-prescribed simulation. This strategy also provides the ability to control for weather noise in order to detect potentially subtle non-local irrigation impacts.

We performed three sets of ensemble hindcast experiments, summarized in *Table 2.1.* In the control simulations (CTRL), irrigation was set to zero. In an irrigation-enabled ensemble (IRRIG), water is added over the region according to *Eq. 2.1*, with the reduced value of F_{IRRIG}. In addition, as a sensitivity test, we create a second 60-member irrigation ensemble with twice the amount of irrigated area per grid cell (IRRIG2X), effectively increasing the local irrigation rate. Details of this experiment design can be found in Section A.1. This aids the search for monotonic non-local responses to irrigation but is also a scientifically interesting test in its own right as a plausible future in South Asia, as

population continues to grow rapidly and food demand rises alongside it [*Davis et al.*, 2017].

Table 2.1. Summary of experiments used in this study.

Experiment	Description
CTRL	Control simulation; irrigation is set to zero.
IRRIG	Irrigation is allowed over the target region specified in *Fig. 2.1*. No modifications are made to the default irrigation area per grid cell.
IRRIG2X	Irrigation is allowed over the target region specified in *Fig. 2.1*. The irrigated area of each grid cell is doubled.

To include a degree of synoptic diversity, 20-member sub-ensembles were initialized on three separate calendar dates (May 10th, 15th, and 20th) from spun-up land and atmospheric conditions drawn from long, free-running model simulations with irrigation enabled; using model generated rather than observed initial states reduces model drift to maximize detectability. Small amplitude noise was applied to the initial temperature field of each ensemble member to seed chaos. The impact of irrigation on the atmosphere was then determined by taking the ensemble mean difference between the irrigation and control ensembles at varying lead times. This difference is considered significant at the 95% confidence level if it was larger than twice the standard error of the differences between individual ensemble pairs.

2.3 Results and discussion

2.3.1 Surface cooling and evapotranspiration responses

Detailed analysis of the irrigation-induced modulation of the local atmospheric environment provides a means to assess the realism of the CLM4 irrigation module. For the following analysis, we assess only the most heavily irrigated region, as outlined by the small rectangle in *Figure 2.1*. At first glance, the response of the local land surface to irrigation is roughly in line with expectations; the increased soil moisture (*Fig. 2.4*) in the irrigation experiments leads to enhanced ET (*Fig. 2.2a*) while decreasing the near-surface air temperature (*Fig. 2.2b*) relative to the CTRL experiment.

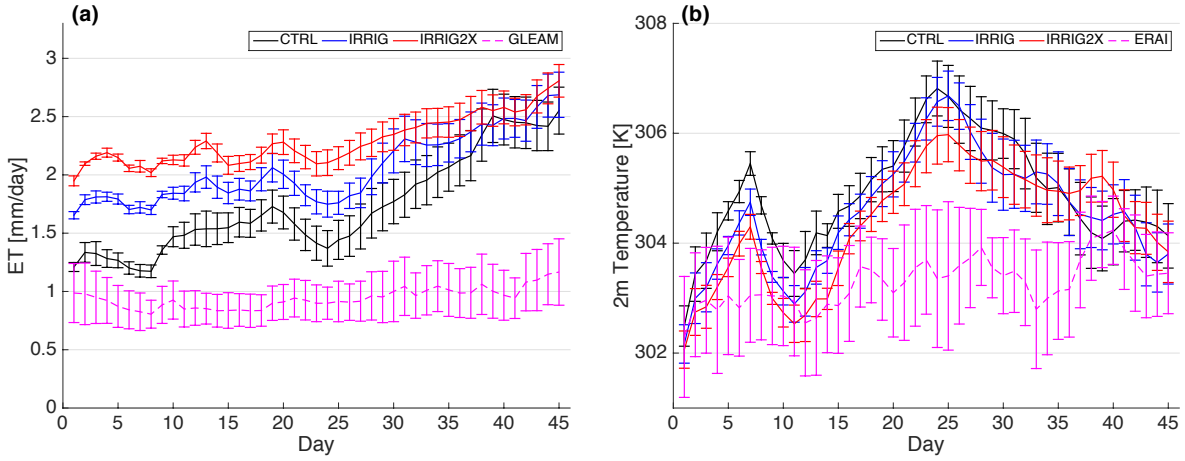

Figure 2.2: *Daily progression of (a) ET, and (b) near-surface (2 m) temperature for the CTRL (black), IRRIG (blue), and IRRIG2X (red) experiments. Averages are taken over all 60-ensemble members in the heavily irrigated region defined by Figure 2.1. Error bars represent twice the standard error of all 60 ensemble members (~95% confidence level). Daily observational constraints, averaged over the period 2003-2015, are included for ET (from GLEAM) and temperature (from ERA-Interim). Day one of both observations is set to May 15th, and error bars again show twice the standard error of the 13 years of observations.*

If the IRRIG2X sensitivity experiment is achieving its intended goal of significantly increasing the irrigation flux above weather noise, there should exist a monotonic sensitivity of the surface variables between the two irrigation experiments. This is indeed the case for at least the first few weeks of the simulation. ET is significantly different between IRRIG and IRRIG2X (and CTRL) through day 25 (*Fig. 2.2a*). The daily progression of surface temperature, however, suggests that the response of this field is more prone to being overwhelmed by other factors (*Fig. 2.2b*); detectable differences between IRRIG and CTRL only extend through day 10, though differences between IRRIG2X and CTRL are distinguishable through day 15.

Though the IRRIG and IRRIG2X experiments are able to produce a reasonable response of the surface to irrigation in comparison with the CTRL ensemble, observational validation reveals potential model biases, though these are difficult to assess given high uncertainty in observed ET. Simulated ET is compared with the Global Land Evaporation Amsterdam Model (GLEAMv3.0b; *Miralles et al.* [2011]; *Martens et al.* [2017]), a global ET product based on satellite observations. The 2003-2015 average daily ET from May 15th – June 28th (dashed line, *Fig. 2.2a*) indicates that ET is over-estimated by CLM4, even in the control case. This dataset, however, may have only limited relevance over this region; it has been noted that GLEAM is unable to capture irrigation-induced ET modulation in irrigated portions of California's Central Valley [*Anderson et al.*, 2012], suggesting that it may not accurately reflect model skill in simulating surface fluxes in heavily irrigated areas. Further supporting this hypothesis, simulations of irrigation in California have been seen to significantly underestimate ET compared to other, well-validated observational constraints

(*Fig. A.1*), while GLEAM again suggested an overestimation. It is thus likely that the irrigation-enabled CLM4 habitually underestimates ET over irrigated areas. Due to the limited nature of reliable ET estimates, however, validation against additional observational products remains outside the scope of the present study.

Simulated near-surface temperature is compared to ERA-Interim reanalysis [*Dee et al.* 2011] over the same period as GLEAM data is available (2003-2015; *Fig. 2.2b*). Though temperature in this region is highly variable from year to year, a model warm bias is apparent over the region, though the addition of irrigation reduces this slightly. This reduction of the CAM5 warm bias as a result of irrigation in CLM4 is also noted in *Huang and Ullrich* [2016].

2.3.2 Initial adjustment timescale

The flux of irrigation exhibits a rapid decay during the first day of the simulation as the model attempts to adjust soil moisture levels up to those targeted by *Eq. 2.1* (*Fig. 2.3a*). After the first day, however, irrigation amounts gradually decline, until entering a steadier state around day 8. We therefore exclude the first week (days 1-7) in subsequent analysis but include all other days as indicative of an irrigation-induced signal (i.e., the "full period" represents a 38-day average from days 8-45; the "initial period" covers only the second week of the simulations, days 8-14).

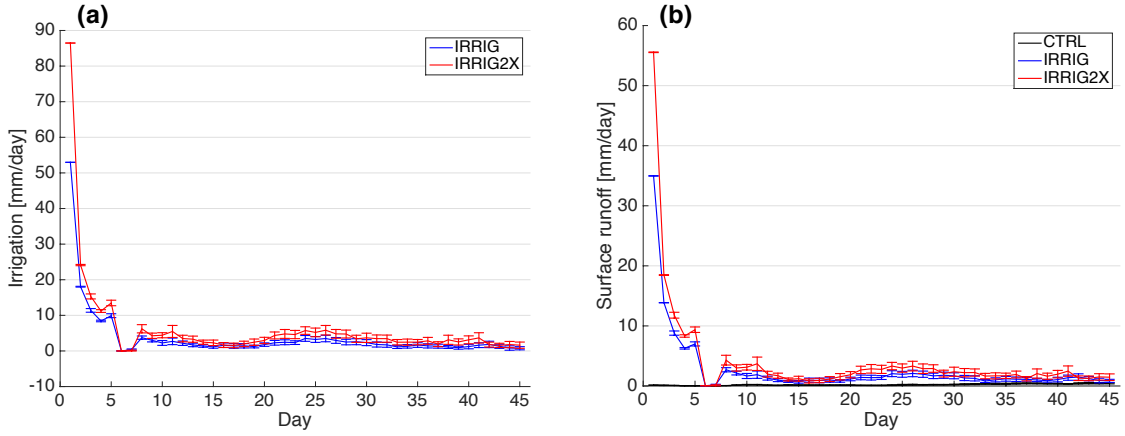

Figure 2.3: *Daily progression of (a) irrigation amounts, and (b) surface runoff. Averages are taken over all 60-ensemble members in the heavily irrigated region defined by Figure 2.1. Error bars represent twice the standard error of all 60 ensemble members (~95% confidence level).*

This choice of excluding only the first week as spinup is further supported when assessing the adjustment of soil moisture to irrigation (*Fig. 2.4)*. To a depth of 1 m, soil moisture takes roughly a week to reach a stable state by increasing continuously throughout days 2-5 before declining temporarily through day 7 (*Fig. 2.4a*). Irrigation amounts drop to zero around the same time that soil moisture at this depth initially peaks (*Fig. 2.3a*), likely indicating that the target soil moisture has been temporarily met by the first few additions of irrigation. Despite a different behavior of soil moisture within shallower levels in response to irrigation (*Fig. 2.4b,c*), a more steady state is achieved by day 7 close to the surface as well.

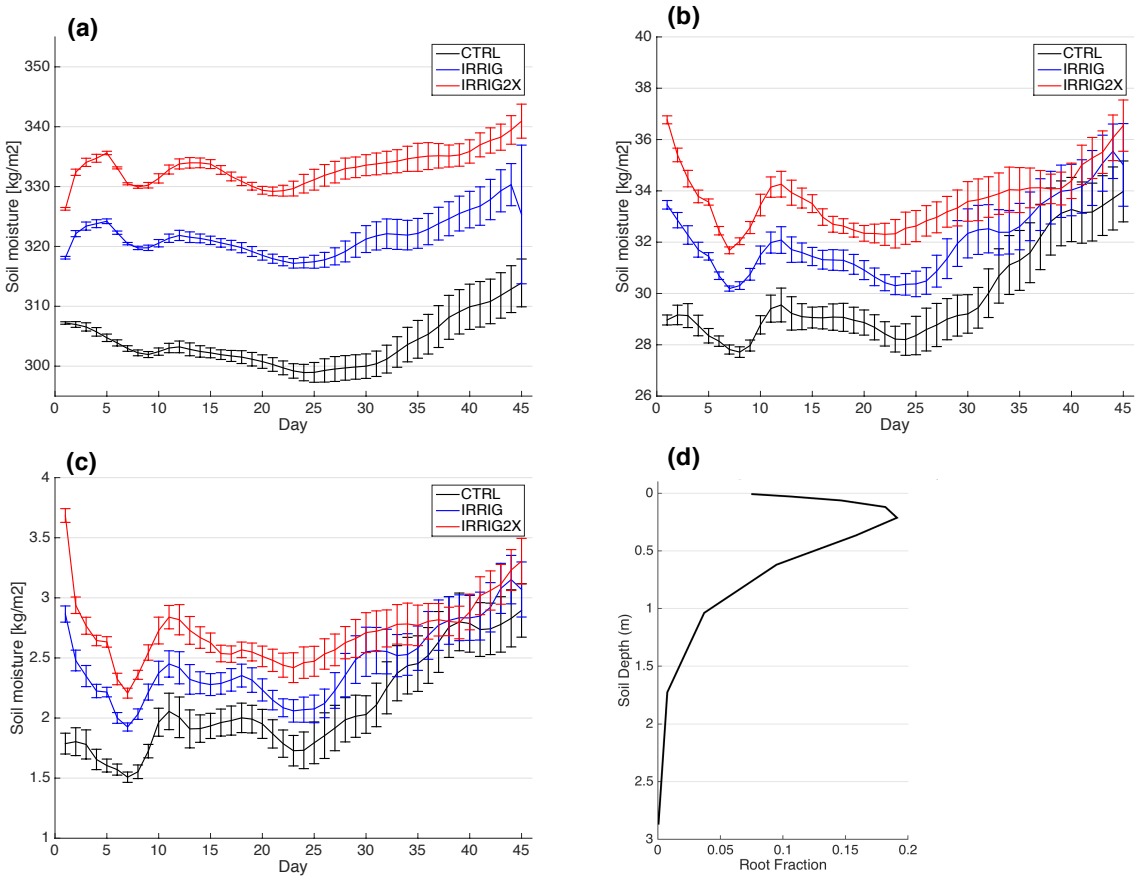

Figure 2.4: *Daily progression of vertically integrated soil moisture in (a) the top 1m of soil, (b) the top 11cm of soil, and (c) in the topmost level of the soil column only. Averages are taken over all 60-ensemble members in the heavily irrigated region defined by Figure 2.1. Error bars represent twice the standard error of all 60 ensemble members (~95% confidence level). (d) The distribution of roots for the crop PFT across all levels of the soil column, as determined by Eq. 8.21 in Oleson et al. [2010].*

2.3.3 Unrealistic aspects of the local land surface response to irrigation

The difference in the soil moisture response with depth during the early stages of the experiment is indicative of a limitation in the way that the CLM4 irrigation module determines soil moisture availability for crop roots. The tight coupling between irrigation amount (*Fig. 2.3a*) and the rate of change of soil moisture vertically integrated to 1 m (*Fig. 2.4a*) indicates that the water deficit is primarily driven by dryness at lower levels of the

soil column; soil moisture in the top 11 cm and topmost layer of the column actually *decrease* after the first day of irrigation, despite continuous water application. This sign reversal of the change in soil moisture with time suggests that irrigation at the surface tends to drain efficiently through the upper soil levels. This hypothesis is further supported by a growing separation between the CTRL/IRRIG and IRRIG/IRRIG2X ensemble mean as the depth of the vertical soil moisture integral increases (e.g. 5 kg/m^2 spread between experiments in the 0-11 cm depth interval, but 30 kg/m^2 spread for the 0-100 cm interval during days 5-20). Though the percent change in soil moisture between experiments is larger at shallower depths, we focus here on the actual *mass* of the applied water and how it is vertically distributed (especially relative to the root concentration profile) since this constrains the extent to which irrigation, which is slave to the vertically integrated water deficit, can actually increase transpiration. The growth in water amount differences suggests very efficient topsoil throughflow that allows water to pool at depth. Given that just over 50% of the crop PFT's roots are present in the upper 11 cm of the soil column (*Fig. 2.4d*), this limits the transpiration increases that are intended by the addition of irrigation as surface water.

It is also shown that the coupling between irrigation and surface runoff is likely too strong, with runoff shifting from a near constant 0 mm/day in the control ensemble to balancing a large fraction of the irrigation water in IRRIG and IRRIG2X (*Fig. 2.3b*). Runoff in the most heavily irrigated region represents a loss of more than 60% of the applied irrigation water when averaged over the full period, a fraction that would suggest striking irrigation inefficiencies in an already water-scarce region if it were true. It is unlikely, however, that

60% of irrigation fails to enter the soil column in reality. *Huang and Ullrich* [2016] suggest that the irrigation scheme in CLM4 has a tendency to overestimate surface runoff as a result of infiltration limitations at the surface. In addition to high runoff as a result of Indian irrigation, we have also found unrealistically high partitioning of irrigation water to surface runoff in simulations of Californian irrigation (*Fig. A.2*). Indeed, the implementation of irrigation in CLM4 inherently reduces the amount of water that can seep into the soil relative to some other studies by concentrating irrigation water within a fractional area of each grid-box and applying it all over a short period of time (only 4 hours per day). An infiltration threshold thus appears to be surpassed relatively early in each application of irrigation, leading to enhanced surface runoff.

The above deficiencies of the irrigation scheme suggest that tuning F_{IRRIG} alone, as in *Leng et al.* [2013, 2015], may not be enough to achieve a realistic response of the land surface to irrigation. Additional parameters in the CLM4 irrigation methodology may also need retuning to hedge against an infiltration and soil flow problem that is endemic to CLM4. For instance, it may be necessary to apply irrigation for longer durations during the day and at lower rates to allow the water to infiltrate into the surface, similar to the approach used by *Lo and Famiglietti* [2013], which applied irrigation evenly at every time step during the growing season. It may also be necessary to tune sub-surface infiltration to ensure the additional irrigation water interacts with the portions of the soil column with the heaviest root fractions. Alterations such as these might increase the chance of the morning-diagnosed irrigation requirement achieving its intended effect of filling soil moisture deficits in the root zone, and consequently boosting ET more strongly. From this view, one

role of the IRRIG2X experiment is to compensate for these deficiencies that otherwise limit the ET magnitude response in IRRIG. That is, the pair of (IRRIG, IRRIG2X) simulations may bracket the potential atmospheric forcing amplitude, in addition to being interesting in their own right as sensitivity tests.

2.3.4 Robust but synoptically sensitive non-local precipitation responses

The impact of irrigation in India on ET, surface temperature, and precipitation from the 20-member May 15th hindcast ensemble in the IRRIG experiment is shown in *Figure 2.5* for the full 38-day period of analysis. Locally to the most heavily irrigated region, the most robust signal is an increase of ET and an associated decrease in near-surface temperature, as expected. The magnitude of this cooling is on par with previous estimates for the region, though it is more localized than in *de Vrese et al.* [2016].

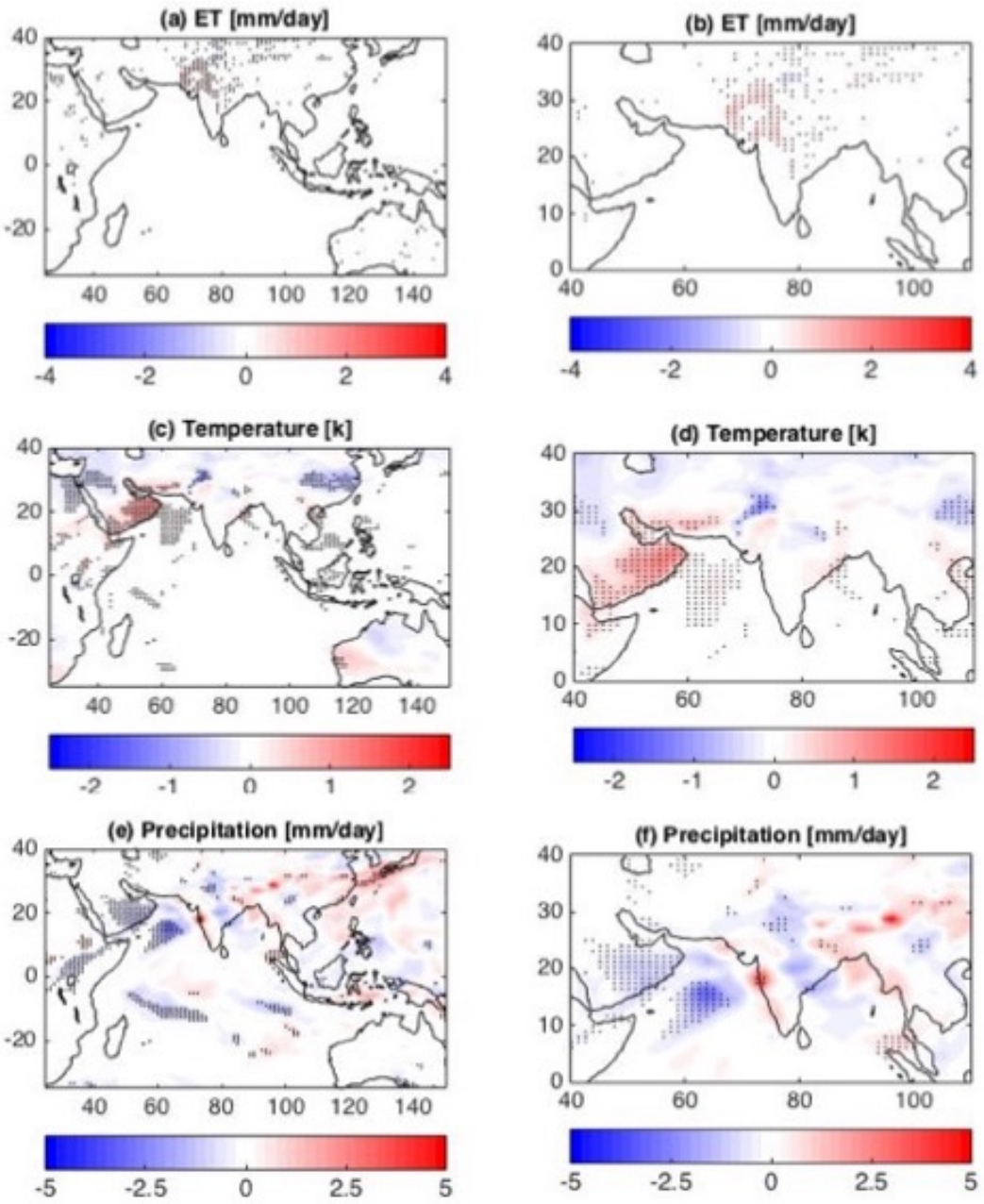

Figure 2.5: *Ensemble mean difference (IRRIG-CTRL) in days 8-45 average (a,b) ET, (c,d) near-surface temperature, and (e,f) precipitation in the May 15th ensemble. The second column is the same as the first, but the region shown is restricted to the area of largest changes for easier viewing. Stippling represents significance at the 95% level as determined by the standard error of the differences between irrigation and control ensemble members.*

In terms of precipitation, an almost local change occurs just to the east of the heavily irrigated region, where rainfall decreases over northern India. Interestingly, there are also

a few regions of non-local precipitation decreases over Africa, the Arabian Peninsula, and the Arabian Sea. If robust, these signals are contrary to the findings of *de Vrese et al.* [2016], who noted climatological precipitation increases in these regions and over parts of Australia when implementing an irrigation scheme within the ECHAM GCM.

The advantage of a hindcast approach is that the robustness of these non-local ET and precipitation responses can be easily tested. We therefore expand beyond this initial ensemble to determine if the responses in *Figure 2.5* are (1) resilient to different synoptic conditions, and (2) amplify under a doubling of the irrigation level. To address the first condition, we assess all 60-members of our irrigation and control ensembles, now spanning two additional calendar dates separated by 5-day intervals. To test the second condition, we analyze the IRRIG2X experiment ensemble, which prescribes twice the amount of irrigated area per grid cell.

These additional experiments reveal interesting patterns in the response of non-local precipitation as a result of irrigation (*Fig. 2.6*). Multiple robust precipitation responses are detectable that amplify coherently in response to doubled irrigation (left vs. right panels of *Fig. 2.6*). To maximize their detectability while also avoiding the initial adjustment period revealed in Section 3b, we focus on the early period of days 8-14, exploiting the nature of a hindcast approach to minimize noise associated with flow decorrelation at longer lead times.

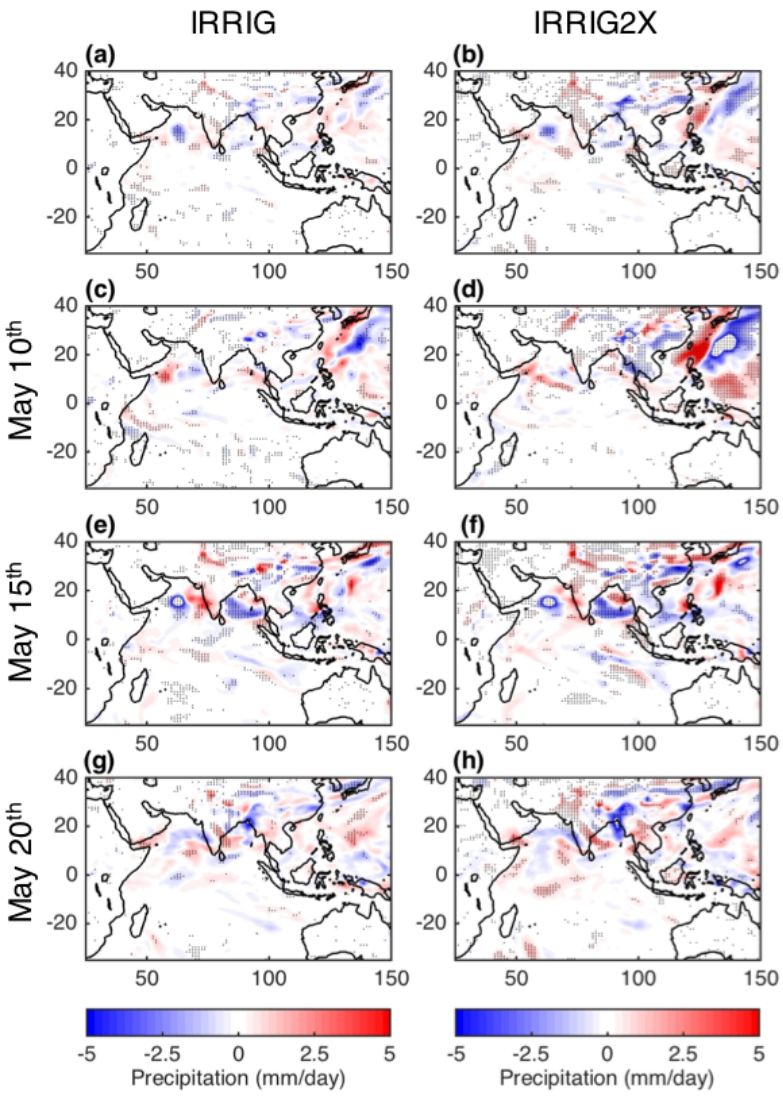

Figure 2.6: *Change in precipitation (irrigation – control) over days 2-10 of the simulations for the 60-member ensemble mean with original irrigated area (a) and doubled irrigated area (b),and for the 20-member initialization date sub-ensemble means: May 10th (c,d), May 15th (e,f), and May 20th (g,h), where the left column gives the results of the IRRIG experiment, and the right column shows the IRRIG2X experiment.*

There is a robust local increase in precipitation as a result of irrigation in the 60-member ensemble mean (*Fig. 2.6a*). The fact that this feature amplifies when irrigation is doubled (*Fig. 2.6b*) and occurs in all sub-ensembles attests to its robustness. Similarly, there is a robust decrease in non-local rainfall over the Bay of Bengal (*Fig. 2.6a*) and a zonal dipole

pattern of precipitation changes over the East China Sea and western North Pacific; these signals amplify in the doubled irrigation experiment (*Fig. 2.6b*), which confirms they do not occur by chance, but as shown below, are synoptically sensitive.

Robust non-local effects of irrigation are detectable but dependent on synoptic details, determined by comparison of the sub-ensembles from independent initialization dates in *Figure 2.6*. For instance, the Bay of Bengal precipitation reduction is only apparent at lead times of 8-14 days when a ridge of high pressure is present just to the west of the region, as in the May 15th ensemble (*Fig. 2.6e,f; Fig. A.3*), while the East China Sea dipole pattern of precipitation changes is most apparent in the May 10th ensemble (*Fig. 2.6c,d*), though this action center occurs in multiple sub-ensembles. Other robust yet synoptically-specific responses to irrigation include a decrease in precipitation over the Arabian Sea in the May 15th ensemble (*Fig. 2.6e,f*) and an increase in rainfall over the Eastern Ghats region in the May 20th ensemble (*Fig. 2.6g,h*). Synoptic conditions associated with each of these initialization dates, diagnosed from the wind field at 750, 500, and 200 hPa and vertically integrated precipitable water, are included in the supplementary information (*Fig. A.3-5*).

At longer lead times (8-45 days; *Fig. 2.7*), many of the above regional responses become shrouded by noise, though the May 15th decrease in precipitation over the Arabian Sea does appear to be a lasting, robust feature. The disappearance and/or weakening of other signals, however, indicates that synoptic variability can overwhelm many fast, regional effects of irrigation. Likewise, many potentially significant changes initially suggested by the May 15th ensemble in *Figure 2.5* are not robust to differing weather conditions or

increased irrigation amounts; decreases over the Arabian Peninsula are only present in *Figure 2.7e*, and do not amplify when additional irrigation is applied (*Fig. 2.7f*). Similarly, decreases in rainfall over Africa and the Arabian Sea are not present in all initialization date sub-ensembles, nor do they increase as a result of doubling the irrigated area of each grid cell.

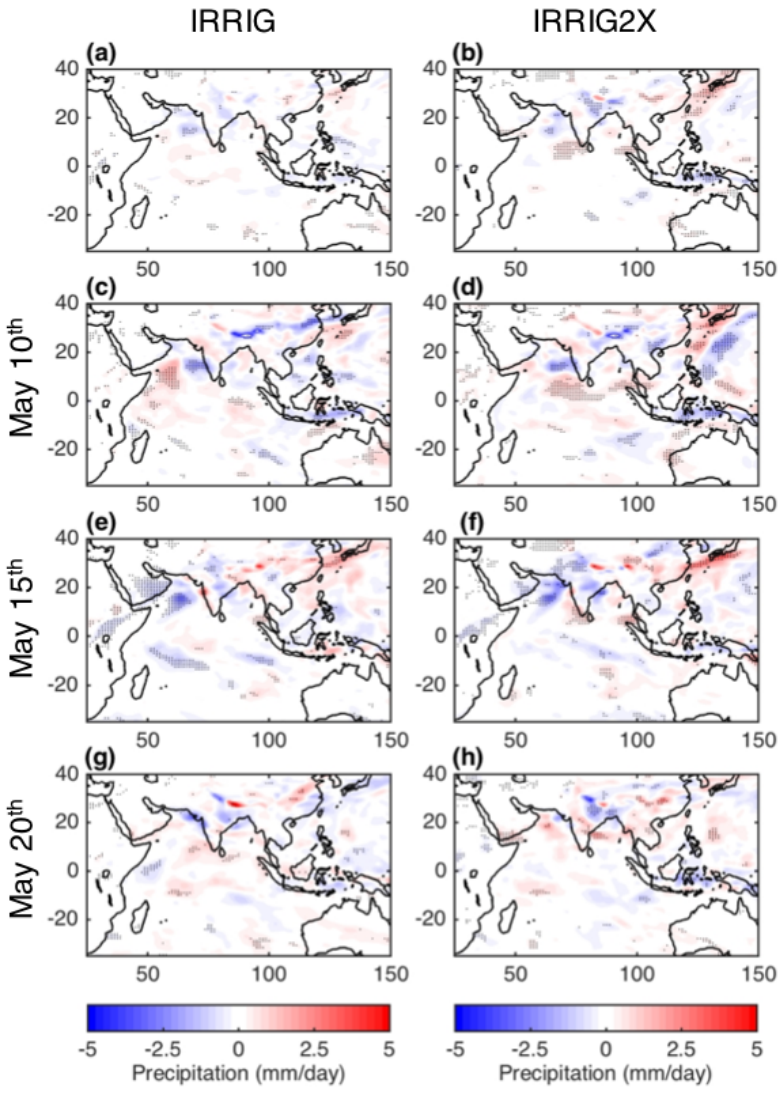

Figure 2.7: *As in Figure 2.6, but with averages taken over the full period (days 8-45).*

Two features, however, are apparent in *Figure 2.7* that may indicate bridge mechanisms capable of projecting beyond synoptic onto sub-seasonal (and thus potentially even climatic) timescales. This is again evidenced by the amplification of coherent regional patterns in response to a doubling of irrigation. The first signal is an irrigation induced precipitation reduction over northeastern India, visible in the full 60-member ensemble mean (*Fig. 2.7a,b*), as well as, more noisily, in each sub-ensemble. The second is a southwest-to-northeast oriented positive rainfall anomaly off the east coast of China, extending over Japan, which amplifies in two of the three sub-ensembles (*Fig. 2.7c,d; e,f*) and in the full ensemble mean (*Fig. 2.7a,b*), evocative of a Meiyu-Baiu rainband teleconnection. Both signals are also present at shorter lead times (*Fig. 2.6*), suggesting robust non-local impacts of Indian irrigation over a range of time scales (though in different action centers than suggested by *de Vrese et al.* [2016]).

2.3.5 Details of the fast response and the role of moisture advection

For the most part, robust impacts of Indian irrigation are only detected at short lead times when weather noise can be controlled. To provide another perspective on the precipitation response in this regime, we also evaluate percent changes, as there are large geographic gradients in the baseline amount of rainfall across the region (*Fig. 2.8*). This visualization highlights an additional region of locally increased precipitation in southwestern and central India, though regions of significance vary slightly between sub-ensembles, leading to only weak significance in the ensemble mean (*Fig 2.8a,b*). Nevertheless, this suggests robust increases in precipitation over much of India as a result of irrigation, at least on fast time scales.

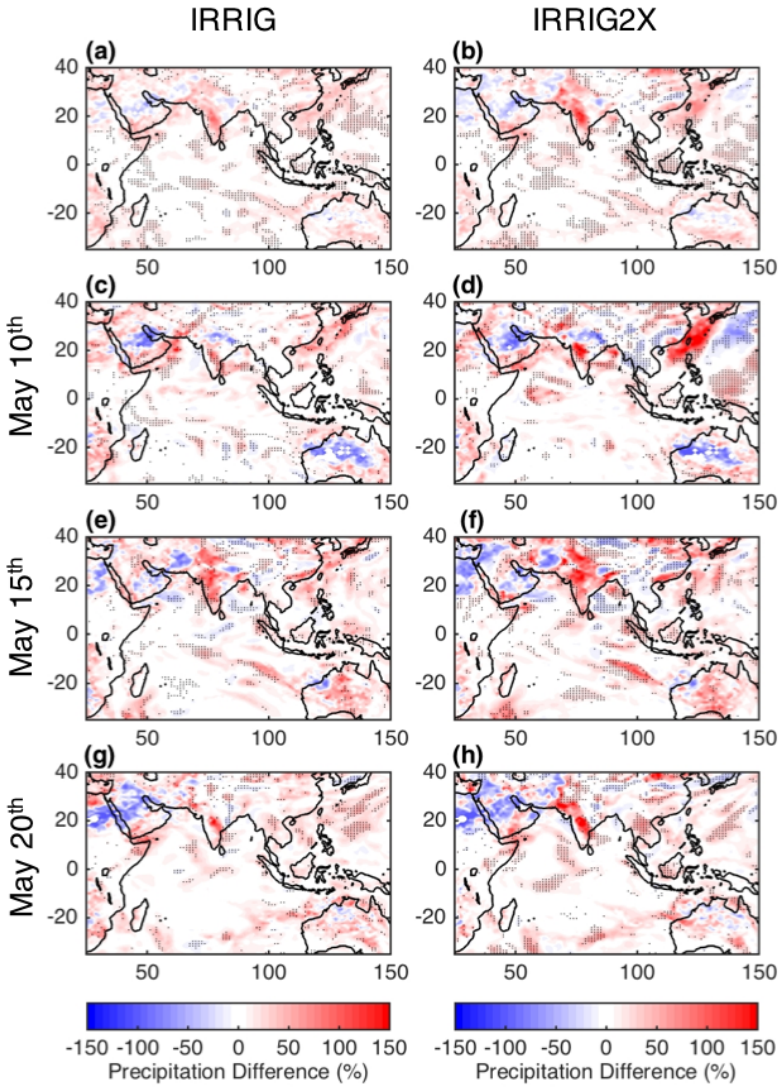

Figure 2.8: *As in Figure 2.6, but with changes (IRRIG-CTRL left; IRRIG2X-CTRL right) shown as percent rather than absolute values.*

Similar to the findings of *de Vrese et al*. [2016], the ensemble mean response of rainfall to irrigation shows small increases in portions of the Arabian Peninsula, Africa, and Australia (*Fig. 2.8a*). Our analysis further reveals a sensitivity to the synoptic conditions for these features. Increases in these regions appear in each sub-ensemble, but the location and

magnitude of the change varies between initialization date and does not always amplify in the doubled irrigation experiments. This again suggests that significant changes in non-local precipitation as a result of Indian irrigation can be unique to certain synoptic conditions.

In a further attempt to identify potential pathways linking irrigation in India with non-local hydroclimatic changes on the fast timescales where we have maximum detectability, we analyze the daily progression of vertically integrated precipitable water in the May 20th ensemble (*Fig. 2.9*; similar figures for all other experiments are available in Section A.3). In this case, we assess days 1-10, as the growth of noise in this particular atmospheric field inhibits the detection of robust, irrigation-induced signals beyond the first few days of the simulations. An initial irrigation-induced local increase in column water vapor spreads to the east with the prevailing westerlies (*Fig. 2.9,* days 1-4), preceded by a developing negative moisture anomaly that travels ahead of it until it reaches the Bay of Bengal (*Fig. 2.9*, days 2-5). This pattern is enhanced in the doubled irrigation experiment initialized on the same date, and similar patterns are present in the May 10th and 15th ensembles, though they are less cohesive when initialized on these dates. After roughly ten days, the similarity between ensembles deteriorates and spurious changes begin appearing in the southern hemisphere randomly, likely a result of noise beginning to dominate the signal.

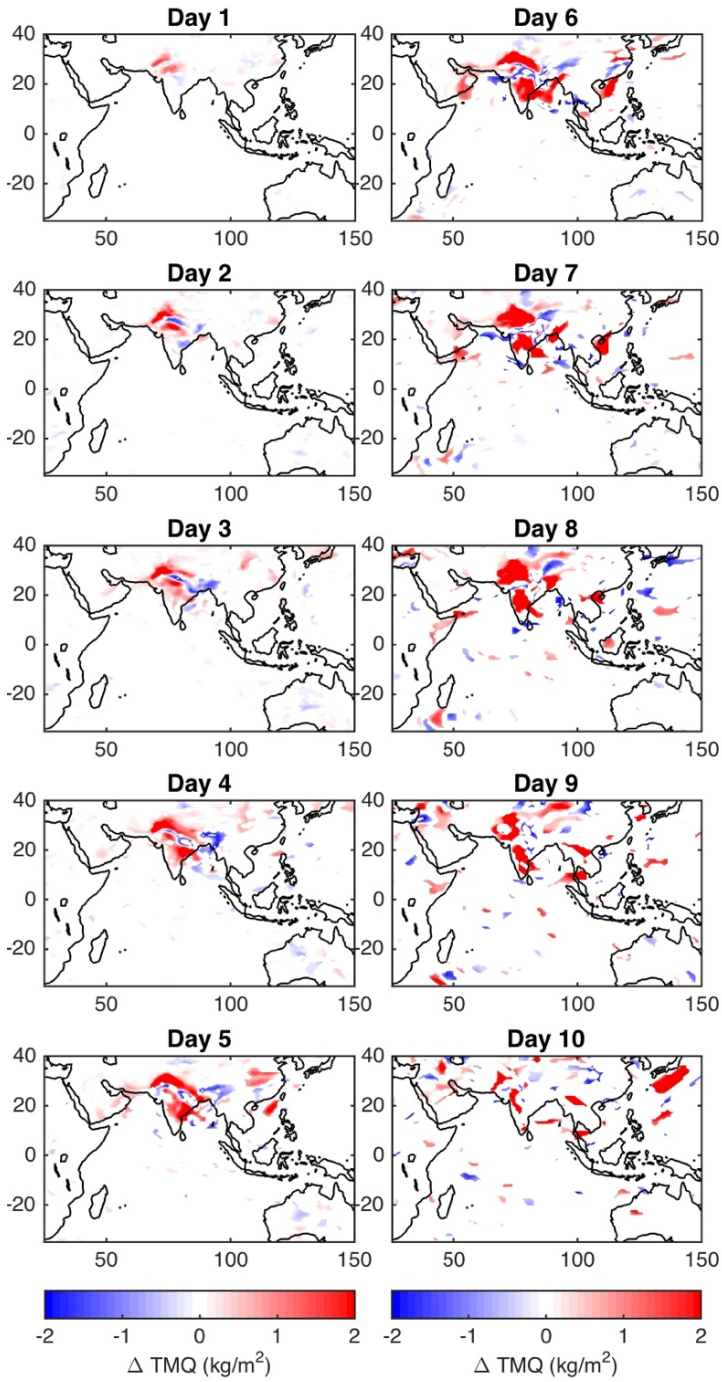

Figure 2.9: *May 20th IRRIG ensemble mean response of vertically integrated precipitable water (IRRIG-CTRL) during the first 10 days of the simulation.*

de Vrese et al. [2016] suggest an advective pathway (including rainout and subsequent re-evaporation) by which enhanced atmospheric moisture over south Asia can lead to

increased precipitation over regions of Africa and Arabia. Our results, however, do not exhibit a smooth transition of atmospheric water vapor that would indicate an advective pathway linking these regions with Indian irrigation. On the one hand, this may simply be a result of differences in the choice of analysis period; *de Vrese et al.* [2016] show that advection towards these regions is dominant in early rather than late spring, which we have not sampled here. On the other hand, we do not see a smooth advective footprint in any direction, which may argue against the dominance of such a bridge mechanism at levels detectable from noise, at least in CESM.

2.3.6 A dynamic limitation on ET response magnitude

In Section 2.3.1, we suggested that the magnitude of the ET response to irrigation in our experiments may be unrealistically small, due in part to sub-surface distortions (i.e., surface and subsurface runoff partitioning). A second factor that may be acting to limit the ET response in India is a reduction of near-surface horizontal wind speeds, which can reduce the efficiency of evaporation. While the situation is more complex over land, one way to quantitatively illustrate this effect is by decomposing the ET demand into thermally- and wind-driven components under the bulk latent heat flux formulation used over ocean surfaces:

$$ET' = \rho L_v C_e(\overline{\Delta q}|V|' + \Delta q'|\bar{V}| + \Delta q'|V|') \qquad (2.2)$$

where ρ is the density of air, L_v is the latent heat of vaporization, C_e is the latent heat transfer coefficient, q is the saturation specific humidity, and $|V|$ is the near surface horizontal wind speed (e.g. *DeMott et al.* [2016]). Overbars denote mean values, while

primes represent differences taken between the irrigation and control experiments. The first term of the equation ($\overline{\Delta q}|V|'$) gives the wind-driven portion of ET changes, while the second ($\Delta q'|\bar{V}|$) gives the thermodynamically-driven component; the third term represents second order effects. The results of this decomposition for monthly mean output in our simulations show that changes in the velocity field are large enough to rival the reduction of potential ET that is caused by near-surface moistening (*Fig. 2.10*). A lowering of wind speeds when soil moisture is increased has been reported in other studies as well, suggesting a local wind response that is robust across numerous models [*Saeed et al.*, 2009; *Tuinenburg et al.*, 2014; *de Vrese et al.*, 2016].

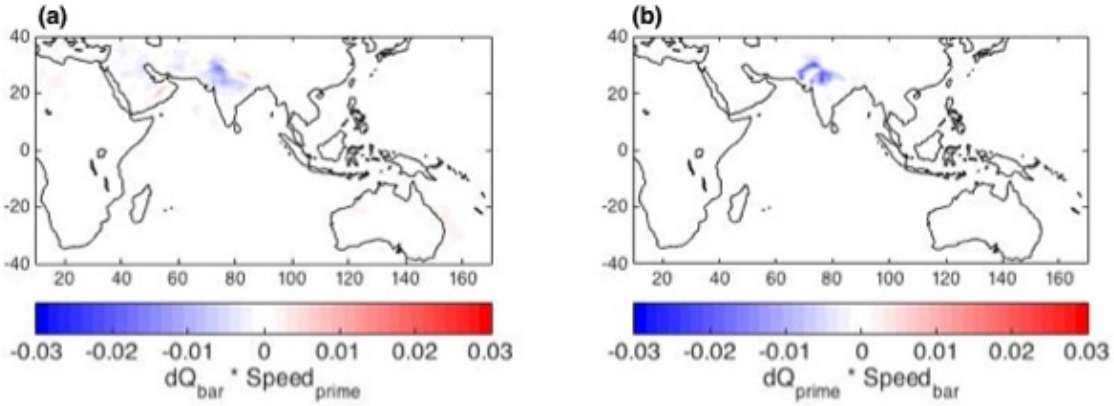

Figure 2.10: *ET' decomposition into (a) wind-driven and (b) thermally-driven components, as determined by the full 60-member IRRIG ensemble mean May values for each term.*

These two effects, increased runoff and a reduction in the wind-driven component of ET, combine to limit the impact of land surface changes on the overlying atmosphere. These may represent model deficiencies to some extent, but may also constitute important negative feedbacks between irrigation, ET, and precipitation.

2.4 Summary and conclusions

The addition of explicit irrigation schemes within GCMs is a recent phenomenon, with potential atmospheric consequences that have not yet been fully explored, and methodological considerations that are quickly evolving. In this study, we have used the irrigation-enabled CESM to assess the impact of Indian irrigation on the hydroclimate surrounding the region both locally and non-locally, and investigated the realism of the irrigation module in CLM4. To our knowledge, this is the first instance of a hindcast ensemble approach being used to study irrigation. This methodology helpfully minimizes internal variability (at least at short lead times), which has been noted for its obscuring role in determining the effects of irrigation [*Thiery et al.,* 2017]. It also allows for the identification of initial synoptic conditions that lead to differing non-local impacts of irrigation.

Locally, we find the expected response of increased ET and decreased surface temperatures. The impact on local precipitation is also roughly in line with expectations set forth by previous studies; irrigation during the pre-monsoon period over India enhances local precipitation, likely as a result of increased moisture recycling [*Saeed et al.*, 2009; *de Vrese et al.*, 2016].

Tightly controlled hindcast simulations with irrigation enabled over India also lead to robust non-local precipitation changes, though the response is found to be highly sensitive to different synoptic conditions. For example, we find decreases in precipitation over parts of the Arabian Sea in the May 15th ensemble, and increases in rainfall over the Eastern

Ghats region in the May 20th ensemble, but these changes are unique to a single sub-ensemble and do not appear in the others. On longer, sub-seasonal time scales, the primary impact of Indian irrigation is an increase in precipitation off of the east coast of China, suggesting potential interactions with the Meiyu-Baiu rainband that may be important in CESM for bridging irrigation impacts to climatic time scales.

Our findings indicate an irrigation-induced ET increase was potentially limited by an unrealistic response of the land surface to irrigation in the CLM4 framework, wherein higher irrigation amounts primarily increase surface runoff rather than soil moisture and subsequently ET. In our focus region of India, more than 60% of irrigation water runs off at the surface over the full study period, suggesting a suspiciously large irrigation inefficiency. Though we have not closed the water and energy budgets to determine precisely where the model is failing, we suspect this to be an excessive amount of runoff, as has been noted in previous studies attempting to apply irrigation within the CLM4 framework, indicating a consistent infiltration limitation in this particular model [*Sacks et al.*, 2009; *Huang and Ullrich*, 2016]. This is further supported by additional offline experiments we have performed over the Central Valley of California, where runoff is observed to be less than 1 mm/month by *Sorooshian et al.* [2014] but systematically exceeds that value on a daily basis in CLM4 (*Fig. A.2*).

We also find that the portion of irrigation water that *is* able to infiltrate the surface has a tendency to drain through the upper levels of the soil column quickly, so that the majority of the roots are inefficiently exposed to elevated soil moisture, thus damping the

transpiration portion of ET increases caused by irrigation. We thus suspect that this version of CLM4 may be unable to realistically partition irrigation water between ET and runoff as has been found by others where observational constraints are rich [*Sacks et al.*, 2009; *Huang and Ullrich*, 2016], but acknowledge that further observational validation over India would be needed to confirm or deny. It is also worth noting that the irrigation scheme neglects groundwater availability constraints, an active frontier of next generation land model development [*Leng et al.*, 2014], which can be important in the study region [*Siebert et al.*, 2010]. This study can be viewed as isolating the impact of irrigation on rainfall and simulated subsurface hydrology in the absence of groundwater pumping. Additional differences in results could have resulted from the addition of an interactive ocean, which was not included in this experiment design but may result in modified local circulations as a result of feedbacks impacting land-sea temperature gradients. Despite these limitations, the results shown here indicate a capacity for statistically significant modifications of non-local precipitation as a result of irrigation. Although the IRRIG experiment is possibly an underestimate of these impacts as a consequence of the large runoff fraction, the IRRIG2X simulations hedge against this bias by applying a larger irrigation flux, resulting in a larger surface response despite consistently large runoff.

These findings speak to complex, model-specific trade-offs in improving optimal irrigation module design. The CLM4 irrigation scheme is appealing in part because of its realism in the way water is applied – it mimics a sprinkler irrigation system by applying the water as effective precipitation to the land surface (bypassing interception), and is applied during a reasonable time frame each day (four hours in the early morning, when evaporative losses

are lowest). This mimics the practice of farmers in a realistic infiltration environment. However, the throttling of ET by enhanced surface runoff and rapid topsoil drainage suggests that realistic irrigation *application* does not necessarily equate to a realistic *response* of the land surface nor associated forcing to the atmosphere. It could be argued that the ultimate purpose of irrigation, from the perspective of both farmers and the simulated atmosphere, is to un-throttle ET by removing soil water limitations on photosynthesis. From this view, it may be important to fix root causes of limits to infiltration in CLM4, and/or strategically sacrifice realism in the surface application methodology, for instance by artificially prolonging the period over which irrigation is applied beyond four morning hours or increasing the fraction of irrigated area. This could hedge against an infiltration inefficiency that currently obstructs surface-applied irrigation from actually filling the sub-surface soil moisture deficit that defines its target amount.

In this study, the ensemble hindcast approach has the advantage of reducing internal variability such that robust effects of irrigation on non-local precipitation and associated bridge mechanisms could be identified at synoptic-to-subseasonal time scales. However, our analysis was limited to only a subsample of synoptic conditions that could be tested, leaving open interesting questions about climatological impacts. In future experiments, it would be well worth examining a complementary hindcast design that uses a wider range of initial conditions. Meanwhile, our results suggest that the typical methodology of analyzing impacts of irrigation in long, free-running climate simulations might benefit from clustering by synoptic state, which could enhance their detectability while revealing a wide range of physical pathways through which changes may occur.

2.5 Acknowledgements

This study was conducted with funding from the Department of Energy (DE-SC0012152). Kooperman also acknowledges support from an NSF Postdoctoral Research Fellowship (AGS-1349579) and from the Gordon and Betty Moore Foundation (GBMF3269). This work used resources provided by the National Energy Research Scientific Computer Center, a DOE Office of Science User Facility that is supported by the Office of Science of the U.S. Department of Energy under Contract No. DE-AC02-05CH11231, as well as resources provided by the Extreme Science and Engineering Discovery Environment, which is supported by NSF Grant OCI-1053575, under allocation TG-ATM120034. Data from the experiments used in this study are available by request from personal archive. We extend our thanks to both Min-Hui Lo and Ray Anderson for helpful conversations regarding this work, as well as to three anonymous reviewers and the editor for their valuable feedback.

Chapter 3

Identifying the effect of plant-physiological responses to rising CO_2 on global streamflow

Adapted from:

Fowler, M.D., G.J. Kooperman, J.T. Randerson, and M.S. Pritchard, 2019: Identifying the effect of plant-physiological responses to rising CO_2 on global streamflow. Under review at *Nature Climate Change*.

Abstract

River flow statistics are expected to change as a result of increasing atmospheric CO_2, but uncertainty in Earth System Models (ESMs) is high. While ESM biases in precipitation and its response to climate change are important sources of uncertainty, here we show the influence of plant stomatal conductance feedbacks can cause large changes in flood extremes and seasonal discharge and must therefore also be better constrained in land-surface models. We identify a distinct plant-physiological fingerprint on annual peak, low, and mean discharge throughout the tropics and identify four river basins (the Amazon, Parana, Congo, and Yangtze) where physiological responses dominate radiative responses to rising CO_2. This work highlights the roles of plants in controlling water flow through the land-surface and identifies locations where streamflow observations may be useful for better constraining the strength of the plant-physiological response at regional to continental scales.

3.1 Introduction

The effects of climate change on the hydrologic cycle will likely alter river networks and floodplains globally. Improving our understanding of the drivers behind these changes is critical for increasing confidence in projections of future flow extremes. If, for example, the main driver of basin-wide hydrologic change is a result of atmospheric responses to CO_2 increases, then model development efforts should focus on improving the representation of precipitation in ESMs, which is frequently noted as a critical component of flood projection uncertainty [*Dankers and Feyen*, 2008; *Hirabayashi et al.*, 2013; *Eisner et al.*, 2017; *Shkolnik et al.*, 2018]. The ability of plant-physiological changes (i.e. stomatal closure at high CO_2) to

modify extreme runoff, however, has only recently received attention [*Kooperman et al.*, 2018b]. We posit that such ecosystem effects could be just as important as precipitation for streamflow extremes, consistent with known first-order impacts on *mean* runoff and discharge [*Gedney et al.*, 2006; *Betts et al.*, 2007; *Cao et al.*, 2010; *Lemordant et al.*, 2018], thus also requiring significant model improvement efforts to reduce uncertainty.

The atmospheric (radiative) effects of rising CO_2 have been widely studied. Global mean precipitation is expected to increase, with the most extreme rates projected to intensify even more than the Clausius-Clapeyron rate [*Allan and Soden*, 2008; *Zhang et al.*, 2013; *Kooperman et al.*, 2016]. Regionally, more frequent/intense precipitation can contribute to more soil saturation, leading to higher streamflow or more frequent flooding. This is of particular concern in the tropics, where a multi-model ensemble suggests an increase in the frequency and intensity of heavy precipitation despite mean decreases [*Chou et al.*, 2012].

However, atmospheric processes may not be the sole driver of streamflow changes in some regions. As the concentration of CO_2 rises, many plants respond by closing their stomata, which can lower the amount of water lost through transpiration [*Leipprand and Gerten*, 2006; *Cao et al.*, 2010; *Swann et al.*, 2016]. While this effect may be offset at mid-latitudes by increased leaf area, the physiological response of stomata is an important mechanism regulating changes in evapotranspiration in densely forested tropical regions [*Kooperman et al.*, 2018a]. Decreases in transpiration and increases in water use efficiency can lead to

higher antecedent soil moisture, and as a consequence, streamflow may increase even without a shift in precipitation statistics.

The relative roles of future radiative vs. plant-physiological responses in regulating extreme and seasonal streamflow changes have not been previously quantified. In part, this is due to the highly uncertain magnitude of the physiological response in observations, related to the difficulty of directly observing such changes over sufficiently long periods of time [*Hovenden and Newton*, 2018] and across a large range of sites [*Campbell et al.*, 2017]. Incorporating sparse observations into global-scale ESMs has led to wide variance in representation [*De Kauwe et al.*, 2013], with subsequent effects on river discharge further hampered by the lack of sophisticated river routing models in most ESMs. The goals of this study are thus two-fold: first, to assess the extent to which plant-physiological effects modulate global flood frequency and seasonal peak/low flow relative to radiatively driven changes; and second, to identify river basins where plant responses are dominant and thus where efforts to constrain the strength of the net physiological effects in nature (i.e., through carbon enrichment experiments [*Ainsworth and Long*, 2004; *Norby et al.*, 2016] or regional simulations attempting to match observed streamflow changes) may prove most fruitful.

3.2 Methods

3.2.1 Methods summary

To separate the atmospheric and plant responses to elevated CO_2, we conduct a series of four fully-coupled ESM experiments using the Community Earth System Model with

biogeochemistry enabled (CESM1-BGC) [*Hurrell et al.*, 2013; *Lindsay et al.*, 2014], which are validated against flood and streamflow estimates from established CMIP5 RCP8.5 multi-model means by *Hirabayashi et al.* [2013] (hereafter *H13*) and *Koirala et al.* [2014] (hereafter *K14*). Leaf area in the Community Land Model (CLM4; *Lawrence et al.* [2011]) increases with enhanced CO_2 but no dynamic vegetation is represented (consistent with most CMIP5/6 models), which could limit a potential buffering effect from changes in forest area and associated evapotranspiration. The transpiration reduction in CLM4 may also be overestimated relative to observations [*De Kauwe et al.*, 2013; *DeAngelis et al.*, 2016; *Keller et al.*, 2017], though the large spread among observational sites and comparison to other ESMs suggest that the model is not an extreme outlier [*Swann et al.*, 2016].

In three sensitivity experiments, CO_2 was increased to quadruple its pre-industrial value (*CTRL*; 285 ppm) at a rate of 1% yr^{-1}. This increasing concentration was applied to the atmosphere and land in *FULL*, only the atmosphere in *RAD*, and only the land in *PHYS*, following the C4MIP experimental protocol [*Friedlingstein et al.*, 2006; *Arora et al.*, 2013] (where *PHYS* and *RAD* refer to the simulations' forcing rather than a specific mechanism in the complex regional responses). These experiments were extended for 50 years at constant 1140 ppm CO_2. We used daily runoff from the last 30 years of each (*CTRL, FULL, PHYS,* and *RAD*) to hydrodynamically downscale river discharge using the Catchment-Based Macroscale Floodplain model (CaMa) [*Yamazaki et al.*, 2011]. This choice allows consistency with *H13*, but our main findings are insensitive to expanding to 50 years (*Fig. B.1*). Though human management of rivers is not included in our analysis, we have confirmed that CaMa captures the geographic diversity of annual average streamflow

(Section 2.3.3 and *Fig. B.2*) and that *PHYS*-induced ecosystem responses are consistent with previous studies (Section B.1 and *Fig. B.3*).

To estimate flood frequency, we fit the 30-year time series of annual maximum discharge at every location to an extreme value distribution (here, the Generalized Extreme Value; GEV) to compute the return period of a flood magnitude equivalent to the 100-year flood in pre-industrial conditions (hereafter the $CTRL_{100}$ flood), following *H13*. We consider flood changes relative to this baseline return period of 100 years; regions with increased (decreased) flooding thus have future return periods less (greater) than 100 years. We limit our analysis to signals that are significant at 95% as measured across a large bootstrap ensemble (Section 3.2.3).

3.2.2 CESM experiments

The four CESM1-BGC simulations include fully active atmosphere (CAM4; [*Neale et al.* [2010]), land (CLM4; *Lawrence et al.* [2011]), ocean (POP2; *Smith et al.* [2010]), and sea ice (CICE4; *Hunke and Lipscomb* [2010]) components, as described in *Kooperman et al.* [2018b]. *CTRL* was initialized from spun-up pre-industrial conditions with a fixed CO_2 concentration of 285 ppm, which was maintained for 50 years. Three additional experiments (i.e., *FULL, RAD,* and *PHYS*) were then initialized from the end of *CTRL* to test the flood response to quadruple the amount of CO_2. In these simulations the CO_2 concentration increased at 1%/year over a 140-year period and was then held fixed for an additional 50 years. In *RAD* and *PHYS*, the land and atmosphere, respectively, experience the original 285 ppm of CO_2 rather than the increased value of 1140 ppm when they are not

the targeted response pathway, while in *FULL* both the land and atmosphere experienced the increased value. Global runoff from these 1˚ resolution simulations are interpolated to 0.5˚ via a bi-linear cubic spline before being used in the CaMa model.

3.2.3 Hydrodynamic downscaling and extreme value curve fitting

For downscaling coarse resolution ESM output, we use the CaMa-Flood model (version 3.6.2), which uses daily runoff to generate high resolution streamflow by solving a hydrodynamic flow equation [*Yamazaki et al.*, 2011]. This method of downscaling is well established in recent literature [*Hirabayashi et al.*, 2008, 2013; *Pappenberger et al.*, 2012; *Koirala et al.*, 2014; *Shkolnik et al.*, 2018] and produces a reasonably accurate global river flow pattern [*Yamazaki et al.*, 2011; *Hirabayashi et al.*, 2013]. Using runoff instead of precipitation as the driving boundary condition accounts for CO_2 impacts on both precipitation and evapotranspiration, while our experiment design allows us to separate the radiative (*RAD*) and plant-physiological (*PHYS*) contributions to runoff changes. To ensure that CESM1-generated runoff is able to produce reasonable streamflow estimates when paired with CaMa, we compare *CTRL* river discharge with observations from 30 large river basins, as reported by the Global Runoff Data Centre (GRDC). We take the same approach as in H13, choosing 30 river basins that meet spatial (areas larger than 150,000 km^2) and temporal requirements (at least 20 years of data in the modern period of 1970-2000). Computing the correlation between the two datasets provides an estimate of how well the model can simulate streamflow (*Fig. B.2*). The reasonably good agreement provides some confidence that CESM is a useful tool for exploring future changes in streamflow originating from radiative and physiological impacts of rising CO_2.

We consider two extreme value distributions to fit annual maximum discharge to, the Gumbel and the Generalized Extreme Value (GEV). The pattern of flood frequency shifts created from this fitting is found to be insensitive to the choice of distribution, though the magnitude of the changes can vary significantly between the two (*Fig. B.1*). As a result, we focus here only on the regional distribution of changes and the relative contributions of *PHYS* and *RAD* to that pattern. These metrics are insensitive to the choice of curve fit.

We choose the GEV here based on its simulation of less extreme frequency shifts and a reasonable value of the global average probability plot correlation coefficient (0.90). The GEV was then used to find the shape (ξ), location (μ), and scale (σ) parameters to estimate river discharge, *F(x)*:

$$F(x) = \exp\left(-\left(1 + \xi\frac{(x-\mu)}{\sigma}\right)^{-\frac{1}{\xi}}\right) \tag{3.1}$$

The statistical fit to this distribution is carried out independently at each location and for each of the four experiments. The magnitude of a given flood (U_T) can then be determined based on return period (T) by inverting the CDF of the GEV above:

$$U_T = \mu + \frac{\sigma}{\xi}\left(-\ln\left(1 - \frac{1}{T}\right)^{-\xi} - 1\right) \tag{3.2}$$

This is used to estimate the magnitude of the $CTRL_{100}$ flood. *Equation 3.2* is then solved for T to determine the frequency of a flood with the $CTRL_{100}$ magnitude in each of the enhanced CO_2 experiments. Statistical confidence is built by limiting our analysis to signals that are significant at the 95% level, measured by a large bootstrap that is produced by randomly sampling with replacement the actual 30-year annual maxima time series at each location and repeating the GEV fit 1,000 times.

3.2.4 Defining grid cells as *RAD*-driven, *PHYS*-driven, or multiply stressed

To better isolate regions with flood increases that are driven by the atmospheric response (*RAD*-driven), the plant response (*PHYS*-driven), or by a combination of the two (multiply stressed), each grid cell is sorted based on agreement between the three experiments. *RAD* and *PHYS* flood frequency increases must both be at least 20% of the increase in *FULL* for a region to qualify as multiply stressed. Otherwise, the location is assigned to the driver with the larger change between the two. This practice is first carried out at the 0.25˚ CaMa-Flood resolution but is then scaled to the 1˚ CESM grid by identifying the mode of drivers within each larger CESM grid cell. Note that although the Nile region is particularly noticeable as a multiply stressed region (shown in blue in *Fig. 3.1e*), it is not selected for detailed analysis due to the high aridity of the region.

3.3 Results and discussion

3.3.1 Physiological and radiative effects on extreme flooding

To confirm that our use of a single ESM produces flood shift patterns comparable to an established multi-model ensemble, we compared the resulting return period in *FULL* (*Fig.*

3.1a) with the CMIP5 analysis of *H13 (Fig. 3.1b*). Though the magnitude of return period varies between the two, and in fact varies based on how the extreme value distribution itself is defined (section 3.2.3), the sign is reassuringly consistent -- 78.3% of locations in *FULL* show flood changes in the same direction as *H13*. In both cases, the $CTRL_{100}$ flood occurs at least twice as frequently over much of the tropics (dark blue shading in *Fig. 3.1*). Flood frequency decreases instead throughout Western Europe, the Eastern Amazon, and parts of North America (red shading in *Fig. 3.1*), where reduced mean precipitation (Eastern Amazon) or less spring snow melt (high latitudes) tends to reduce runoff extremes.

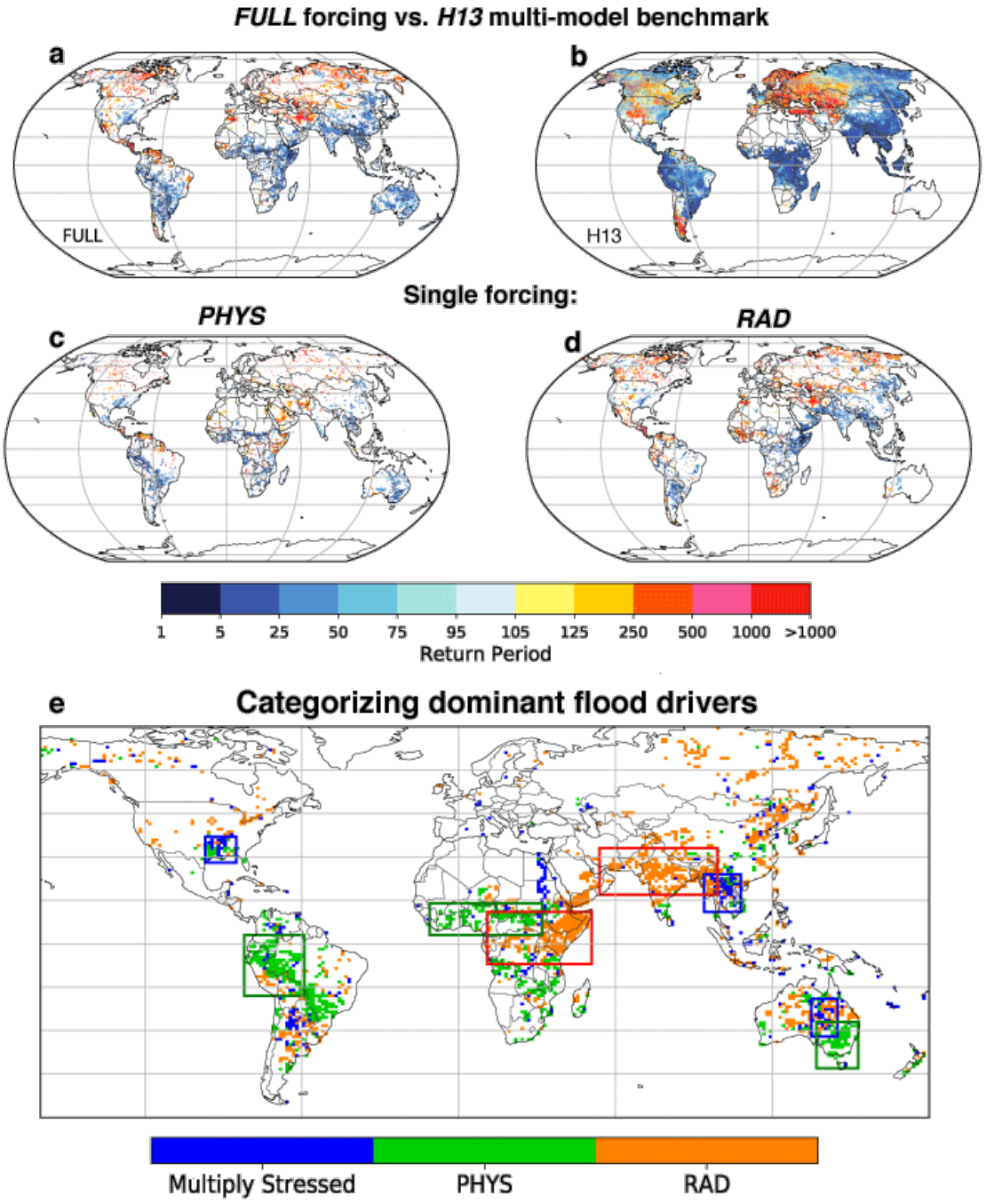

Figure 3.1: *Frequency of the pre-industrial 100-year flood under elevated CO_2 and its drivers. (a) Return period of the historical 100-year flood in FULL vs. (b) the results of H13 for a multi-model average under RCP8.5 forcing (H13 Figure 1; dry regions masked). (c) PHYS and (d) RAD as individual drivers of flood responses in FULL. (e) Regional categorization of flood increases as primarily PHYS-driven (green), RAD-driven (orange), or a combination of both*

(blue) based on their contributions to the return period of the $CTRL_{100}$ flood in FULL. Results omitted in (a, c-e) where insignificant at 95% confidence (see text).

Flood shifts in *FULL* are shown to be a result of both physiologically- (*Fig. 3.1c*) and radiatively- (*Fig. 3.1d*) driven changes in return period, while changes of similar magnitude are induced by either mechanism alone. Over the Western Amazon, for example, increased flooding is primarily plant-driven, where dynamical mountain-forest interactions result in basin-wide precipitation rearrangement [*Kooperman et al.*, 2018a]. Increased flooding over much of South Asia is a result of radiatively-forced changes, potentially due to intensification of the Indian summer monsoon rain [*Christensen et al.*, 2013]. A third class of region can be defined by concurrent changes in both *PHYS* and *RAD*, thus dividing the globe into three flood-driving regimes: *PHYS*-driven, *RAD*-driven, and multiply stressed (*Fig. 3.1e*).

Eight regions with broadly consistent drivers are defined by rectangles in *Figure 3.1e* and analyzed further to determine the cause of increased flooding (Section B.2 and *Tables B.1-B.3*). For multiply stressed regions (blue rectangles in *Fig. 3.1e*), *PHYS* leads to more frequent flooding through increased soil moisture, which we interpret as a direct effect of CO_2-induced transpiration decline (*Fig. B.3*) since it occurs despite increases in plant productivity, leaf area and surface shortwave radiation, which would tend to dry the soil (*Table B.1 and Fig. B.3*). When only the atmosphere responds to rising CO_2 (*RAD*), increased precipitation is the most important driver given the inability of other variables such as snowmelt, which is already near zero in these regions during the flood season, to explain the increased flooding (*Table B.1*). This is also true of regions defined as primarily

radiatively-driven (orange rectangles in *Fig. 3.1e; Table B.2*), consistent with the expectation that warmer temperatures promote higher mean precipitation and/or more frequent extremes, which can increase the likelihood of flooding.

Regions with plant-driven flood changes (green rectangles in *Fig. 3.1e*) experience more frequent flooding not only as a result of increased soil moisture via *direct* stomatal closure, but also through *indirect* precipitation effects, including mean precipitation increases over the Western Amazon (Section B.2 and *Table B.3*) – in turn a result of complex interactions between surface energy partitioning, vertical vapor transport by planetary boundary layer turbulence, and lateral vapor advection by regional orographic flow [*Skinner et al.*, 2017; *Kooperman et al.*, 2018a; *Richardson et al.*, 2018; *Langenbrunner et al.*, 2019].

3.3.2 Detecting a plant-physiological effect on annual streamflow metrics

Although CESM produces a striking physiological effect on floods, uncertainties in stomatal responses to CO_2 are large. Beyond a handful of regional ecosystems that have been subjected to free air carbon fertilization experiments [*Nowak*, 2017; *Hovenden and Newton*, 2018], data are sparse, notably in the tropics; extending direct measurements to span a sufficient range of climates to constrain the magnitude of the stomatal response in ESMs is untenable. This motivates the need for indirect observable proxies of the plant-physiological effect on streamflow in nature, as originally suggested by *Gedney et al.* [2006]. If the same processes that produce large changes in extreme floods also modulate annual streamflow statistics, these -- being more readily observable -- could provide a useful metric for constraining net ecosystem responses to rising CO_2.

We thus investigate the seasonal cycle of streamflow, identifying broad regions and specific river basins where the *PHYS* effect rivals *RAD* contributions to *FULL*. Following *K14*, we compute annual mean (Q_{mean}), peak (Q_{peak}), and low flows (Q_{low}) for each river gridcell based on daily discharge, where seasonal extrema are defined as the 5th and 95th percentile flow rates annually, averaged to climatology.

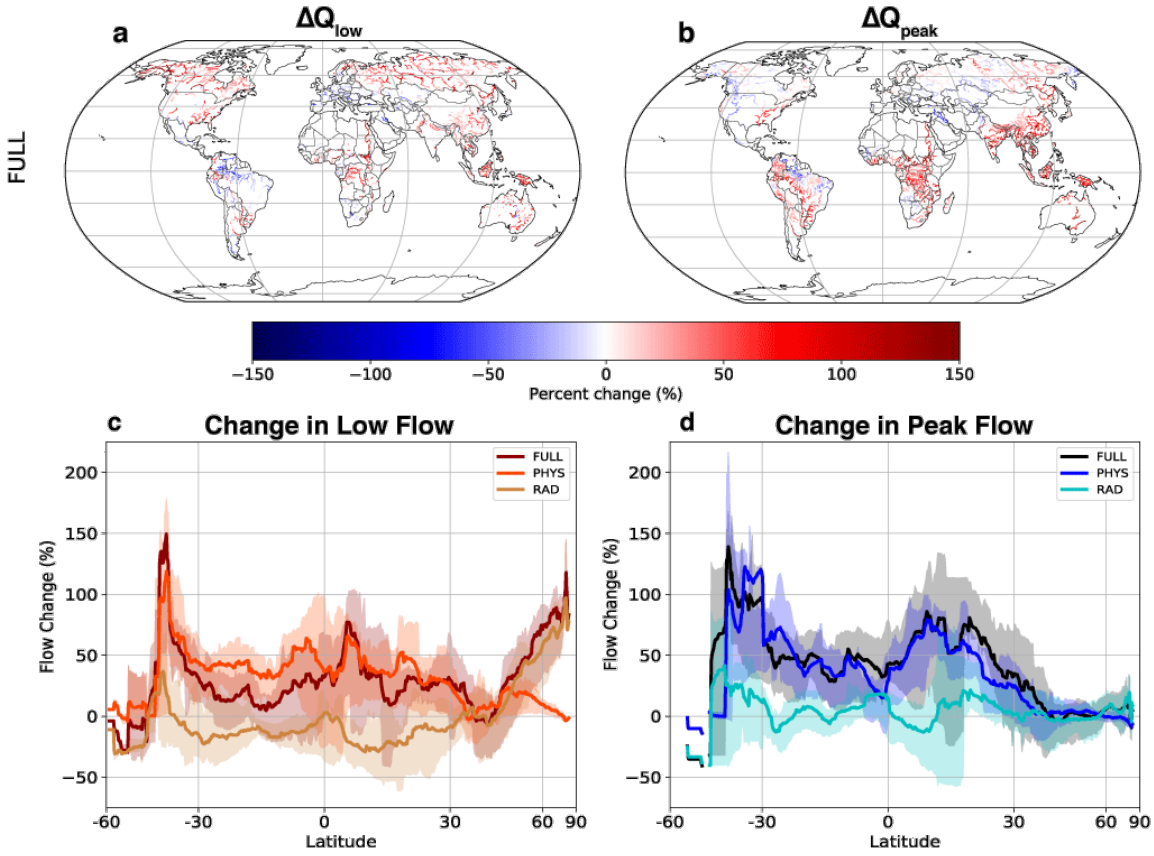

Figure 3.2: *Changes in seasonal streamflow. (a,b) Percent change from CTRL in low and peak streamflow for FULL; regions with CTRL Q_{low} discharge less than 50 or Q_{peak} less than 500 $m^3 s^{-1}$ masked (Fig. B.5). (c,d) Latitudinal decomposition of FULL into PHYS and RAD smoothed 5° running mean; shading denotes zonal variability as the interquartile range.*

We confirm the validity of CESM by comparing our results (*Fig. 3.2a,b*; *Fig. B.4*) with CMIP5 mean changes from *Figure 1* of *K14*. Despite some quantitative and regional differences (*Fig. B.6*), *FULL* agrees well with the overall pattern of the CMIP5 average – 79.2%, 80.5%, and 68.0% of river gridcells in our experiment agree on the sign of Q_{mean}, Q_{peak}, and Q_{low} changes respectively. In general, Q_{peak} increases over much of the globe. Exceptions to this trend occur in high-latitude western Europe and western North America (*Fig. 3.2b*) where strong polar-amplified warming in *RAD* reduces peak snowmelt rates contributing to earlier and lower peak discharge during spring (*Fig. B.7, B.8*), consistent with increases in the ratio of precipitation falling as rain rather than snow (*Fig. B.9*; changes in timing are discussed in more detail below). In the Eastern Amazon, declines are again linked to reduced mean precipitation [*Skinner et al.*, 2017; *Kooperman et al.*, 2018a; *Richardson et al.*, 2018; *Langenbrunner et al.*, 2019].

Consistent with *K14,* increases in Q_{low} tend to be largest at northern latitudes in *FULL* (*Fig. 3.2c*) due to *RAD* forcing (*Fig. B.7*), which increases high latitude mean precipitation and the fraction falling as rain (*Fig. B.9*). This result fits well with a general understanding of the drivers that control peak and low flows regionally; at high latitudes, Q_{peak} is often related to snowmelt, which is heavily influenced by *RAD* but very little by *PHYS*, which instead plays a larger role in the heavily vegetated and sunlit tropics. Responses for Q_{mean} were found to be quantitatively weaker but qualitatively similar to Q_{peak} (*Fig. B.4)*.

Plant-physiology is again a controlling factor for these streamflow shifts. *PHYS* plays a major role in driving dramatic Q_{low} increases throughout densely populated low latitude

regions (*Fig. 3.2a,c*). This occurs largely as a result of higher soil moisture (*Fig. B.10, B.11*), though the ability of plants to alter precipitation is also important in some tropical forest regions. *RAD* tends to reduce Q_{low} throughout the subtropics due to warming induced increases in evaporative demand (*Fig. B.10*) but is overwhelmed by physiological effects in the zonal mean. *PHYS* also contributes to increases in Q_{low} across high-latitude continental interiors; interestingly, this signal is strongest towards the southern edge of the boreal forest, i.e. decreasing with latitude, opposite to the polar-amplified warming effect of *RAD* and associated snow-rain transitions *(Fig. B.7, B.9).* This might suggest the potential for an identifiable fingerprint of the physiological effect in unmanaged high latitude river basins, with the caveat that radiative controls tend to overwhelm the *FULL* response poleward of 45˚N: in the transition zone between *PHYS*- and *RAD*-dominated Q_{low} regimes, the influence of rising CO_2 on ecosystem processes allows for increasing vegetation cover in *PHYS*, yet transpiration reductions overwhelm these changes causing soil moisture to increase, with a sharp boundary at the southern edge of the boreal forest region (*Fig. B.3, B.10*).

Systematic increases in Q_{peak} equatorward of 45˚N are mostly controlled by plant responses. Unlike Q_{low} though, radiatively-driven responses are nearly neutral in the zonal mean (*Fig. 3.2d, Fig*. *B.7*). In the tropics and subtropics, *PHYS* is first-order to changing annual streamflow cycles across most land area. However, close to the poles, the relative importance of *PHYS* again declines; this geographic disparity is summarized by pattern correlations in *Table B.4*.

3.3.3 Quantifying radiative and physiological contributions to basin-level streamflow changes

Our analysis allows us to separate the relative contributions of *PHYS* and *RAD* to changes in discharge for large river basins. Though we carry out a linear decomposition on 32 basins (*Figure B.12*), we limit our attention to 18 in which the relative effects of *PHYS* and *RAD* on *FULL* are additive for mean, peak, or low flow. In these basins, the residual of the following decomposition is small, suggesting the response of *FULL* can be well explained by a linear combination of individual drivers,

$$\frac{\Delta FULL}{CTRL} = \frac{\Delta PHYS}{CTRL} + \frac{\Delta RAD}{CTRL} + \varepsilon \qquad (3.3)$$

Where $\Delta FULL$, $\Delta PHYS$, and ΔRAD are the basin-averaged differences in streamflow from *CTRL,* and ε is the residual, computed as the root mean square error between $\Delta FULL$ and the sum of $\Delta PHYS$ and ΔRAD across the 30-year ensemble (*Fig. B.13* and *Tables B.5-B.7*). If $\Delta PHYS + \Delta RAD$ is larger than ε, the effects are considered to be roughly additive and the results of the decomposition are included below (*Fig. 3.3*).

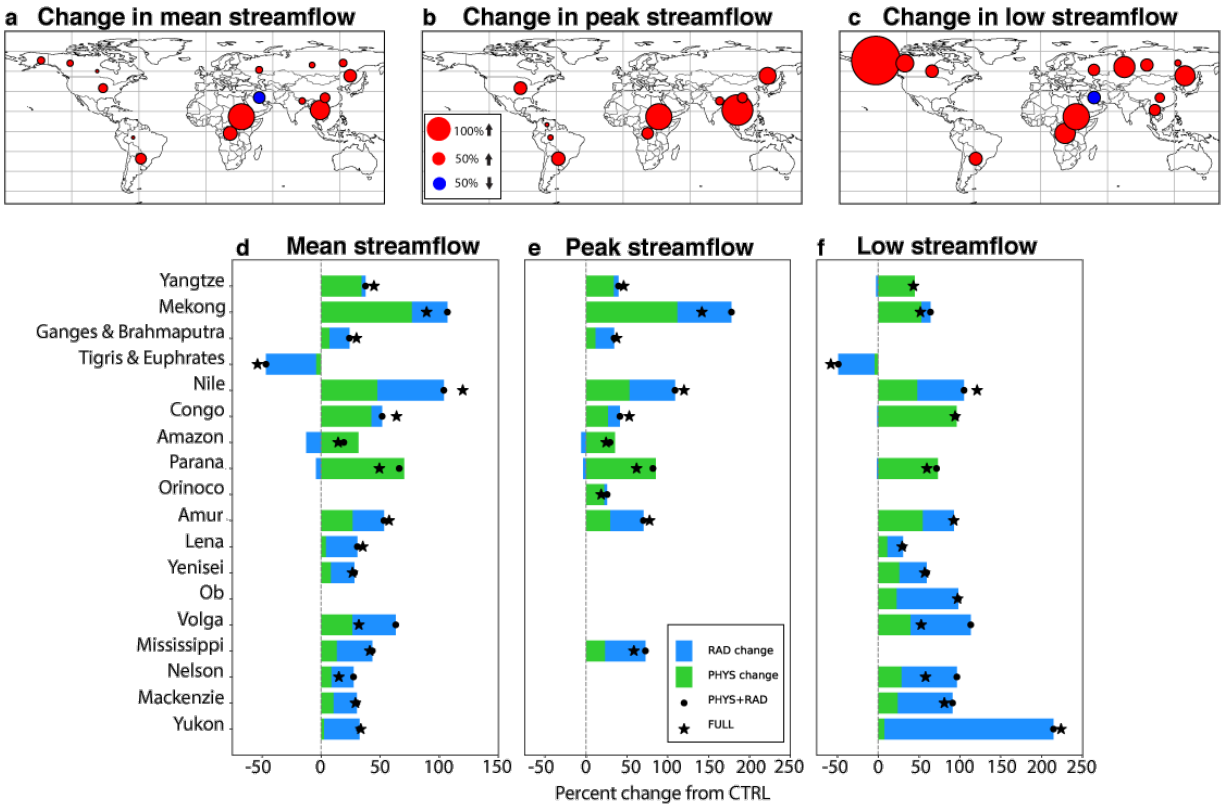

Figure 3.3: *Basin-level streamflow changes. FULL changes in (a) Q_{mean}, (b) Q_{peak}, and (c) Q_{low} relative to CTRL. (d-f) The contributions of ΔPHYS and ΔRAD to ΔFULL flow changes. Black stars represent the FULL percent change from CTRL (as shown by shaded circles in a-c), and black circles represent the sum of ΔPHYS and ΔRAD. Colored bars indicate the ΔPHYS* (green) *+ ΔRAD (blue) percent changes that support the total.*

The primary driver of streamflow change can be identified by the dominant color of the basin's bar in the bottom row of *Figure 3.3*, with the magnitude of *FULL* indicated by the overall size of the circles in the top row. Again, basin responses are driven by *PHYS*, *RAD*, or a combination of both: Mekong Q_{mean} and Q_{low} increases are primarily plant-driven, while the Yukon is almost exclusively radiatively-driven. The Nile, Amur, and Volga shift due to the combined effect of drivers.

Four basins stand out as nearly exclusively plant-driven – the Amazon, Parana, Congo, and Yangtze. Here, *FULL* increases in Q_{mean}, Q_{peak}, or Q_{low} are driven solely by the plant response. Annual streamflow cycles in those basins reveal a systematic effect of *PHYS* to raise streamflow, which controls changes in *FULL* despite opposing changes in *RAD* (*Fig. 3.4*).

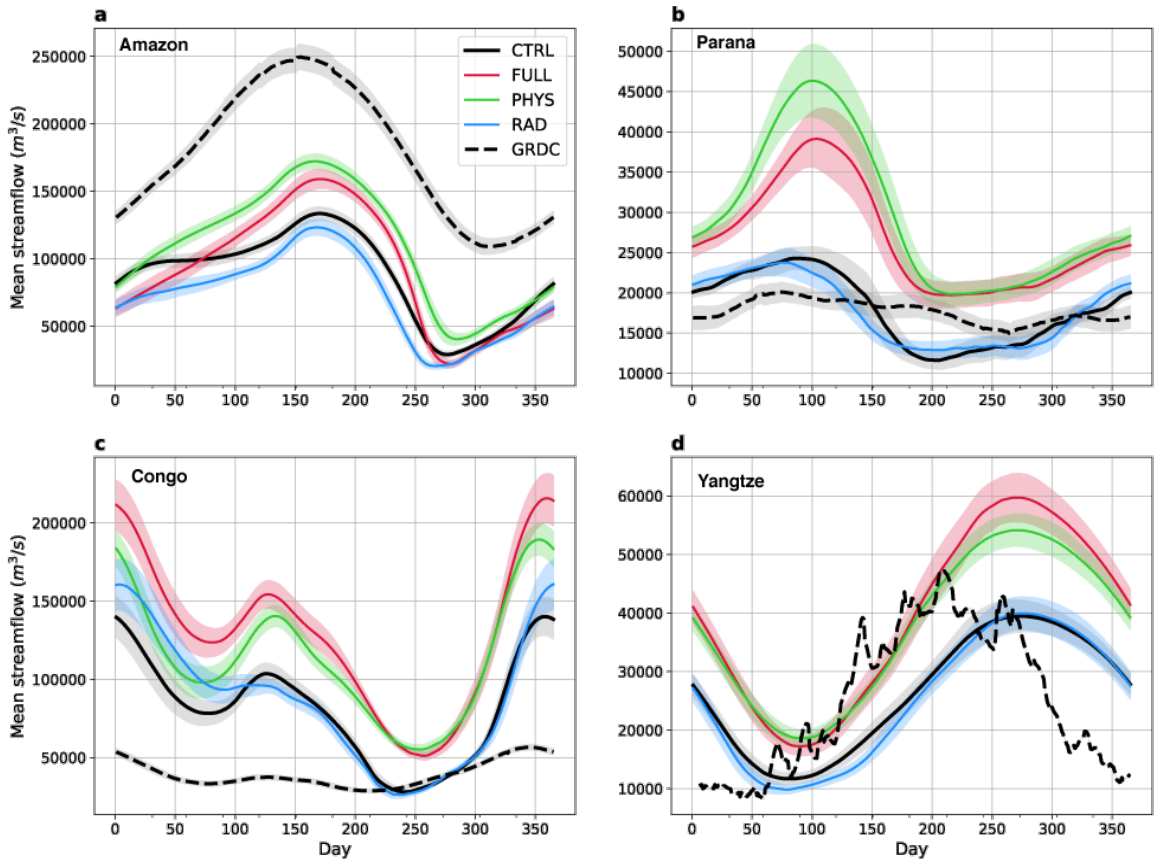

Figure 3.4: *Average annual streamflow cycles at river outlets in PHYS-dominated basins. Area-weighted average streamflow annual cycles near the outlets of each river. Dashed black lines represent nearby GRDC station data (all available years in the period 1970-2005) while colored lines show modeled streamflow, where all grid cells within a quarter degree of the GRDC station have been averaged together. Error bars correspond to twice the standard error of discharge over the 30-year period.*

Despite obvious disagreements between the streamflow simulated in our pre-industrial *CTRL* and 1970-2005 observed river discharge (colored vs. dashed lines in *Fig. 3.4*), there is

little reason to expect good agreement in experiments such as these. Both *CTRL* and *FULL* suffer from regional precipitation biases, including an Amazon dry bias, typical of most ESMs [*Yin et al.*, 2013; *Mehran et al.*, 2014; *Lintner et al.*, 2017; *Sakaguchi et al.*, 2018]. Precipitation in that basin is 27-39% lower than observed during the period of peak streamflow (*Fig. B.14)*, consistent with the underestimation of Amazon streamflow (*Fig. 3.4a*). Too much precipitation falls over the Congo during most months (*Fig. B.14*), consistent with streamflow overestimation there (*Fig. 3.4c*). Additionally, CaMa does not account for human management of river systems, which may cause disagreement in the Parana, which has a number of large dams [*FAO*, 2016] that may damp its seasonal amplitude.

Nevertheless, despite strongly varying bias structures in each basin, the effect of reduced stomatal conductance is a systematic increase in streamflow across all months that is common to all four basins. This consistency adds confidence that the streamflow response to *PHYS* is a robustly simulated signal, in line with the observational findings of *Gedney et al.* [2006] despite the fact that they did not allow for leaf area changes [*Gerten et al.*, 2008]. For these basins, the impact of *PHYS* is mostly an increase in streamflow magnitude, with little change in the timing of peak and low flows. We note, however, that this is not the case in all basins analyzed (*Fig. B.15*), which indicate that *PHYS*-induced changes can influence seasonal phase in some regions outside the tropics.

3.4 Conclusions

Improved understanding of the physical mechanisms behind streamflow and flood frequency changes is critical for future ecosystem planning and management. Here, for the first time, we have linked ESM experiments that isolate the plant-physiological from radiative effects of CO_2 on runoff to a hydrodynamic model that predicts their consequences for streamflow globally. Flood frequency analysis shows that plant-physiological effects on the terrestrial water cycle are a first order control on future shifts of the 100-year flood.

Despite the major role of plants in the evolution of hydrological extremes under CO_2 forcing in CESM demonstrated here, the coupling between water and carbon cycles in modern land-surface models remains poorly constrained. To help address this source of uncertainty and complement sparse observational constraints, we use the model to identify fingerprints of plant-physiological effects in observable metrics of annual streamflow. For low flows, the results show a competition in which the radiative effect tends to reduce but the physiological effect tends to increase seasonal flow minimums throughout low latitudes. At high latitudes, the relatively smaller net plant effect on low flow expresses itself with an opposing meridional gradient to the polar-amplifying radiative effect across boreal forest watersheds. For peak flows, the plant response is the main driver of future changes throughout most low latitudes. Given this, we encourage more investigation of such fingerprints across multiple independent hydrodynamically downscaled ESMs, towards the hope of using observed streamflow to constrain the magnitude of buffered ecosystem responses to CO_2 in nature. Our results also suggest a need to assess the plant-

physiological response's capacity to shift streamflow seasonality at the basin scale. The effect of the plant-physiological response on hydrologic extremes across timescales is often overlooked in future climate projections, but this work highlights the need to assess these effects more explicitly moving forward.

3.5 Acknowledgements

M.D.F. and M.S.P. acknowledge primary support from the Department of Energy Early Career Program (DE-SC0012152) and additional support from the NSF (AGS-1734164) and NASA MIRO (NNX15AQ06A). G.J.K. and J.T.R. acknowledge support from the Gordon and Betty Moore Foundation (GBMF3269) and the RUBISCO science focus area (SFA) supported by Regional & Global Climate Modeling (RGCM) Program in Climate and Environmental Sciences Division (CESD) of DOE's Office of Science. G.J.K. also acknowledges support from the DOE Regional and Global Model Analysis (RGMA) Program (DE-SC0019459). CESM simulations were run and archived at the NCAR Computational and Information Systems Laboratory on Yellowstone (P36271028). Analysis was run in part on XSEDE supported systems Stampede2 (TG- *ATM160016)* and Comet (TG-ASC150024).

Chapter 4

Regional MJO modulation of West Pacific tropical cyclones driven by multiple transient controls

Abstract

The Madden-Julian Oscillation (MJO) is widely acknowledged for its ability to modulate West Pacific tropical cyclones (TCs), though a complete understanding of the underlying mechanisms remains uncertain. Previous attribution to relative humidity increases associated with the convective center are at odds with the more dynamical factors suggested as dominant in new genesis potential indices and high-resolution modeling studies. Here we revisit the ability of the MJO to modulate West Pacific TCs through a strategy that initially avoids the use of a genesis index or aggregation in space/time. We reveal two distinct stationary modes of TC modulation, one in the West-Central Pacific and a particularly strong signal in the South China Sea. The latter is heavily modulated not by relative humidity or shear in isolation, but by a transient progression of environmental factors that ultimately enhance genesis for an extended period in the region.

4.1 Introduction

Understanding how slow modes of tropical weather modulate tropical cyclone (TC) activity is critical to disaster preparedness in today's climate as well as planning for climate impacts in a warmer world. This is especially true in the West Pacific, home to more TCs than any other basin [*Zhao et al.*, 2015a; *Ramsay*, 2017] and the majority of human impacts -- more than 90% of the global population exposed to TCs live in Asia, with population growth alone suggesting an 85% increase in exposure by 2030 [*Handmer et al.*, 2012].

The West Pacific is also home to the Madden-Julian Oscillation (MJO), a slow-moving (30-60 day) packet of anomalous tropical wave activity, which can alter cyclogenesis by

modifying large scale environmental factors such as relative humidity and vertical wind shear [*Frank and Roundy*, 2006; *Wu and Takahashi*, 2018; *Zhao and Li*, 2018]. This oscillation is also projected to amplify significantly in the future by state-of-the-art climate models [*Arnold et al.*, 2014, 2015; *Adames et al.*, 2017; *Maloney et al.*, 2019]. The relationship between the MJO and West Pacific TCs today must therefore be well understood to determine what an intensification could mean for future TC risk.

But although the MJO has long been recognized to alter TC formations in the West Pacific [*Liebmann et al.*, 1994; *Kim et al.*, 2008; *Camargo et al.*, 2009; *Huang et al.*, 2011; *Klotzbach*, 2014], there is disagreement as to why. Prior to the late 2000s, a majority of studies invoked the oscillation's dynamic effects, which can include reductions in vertical wind shear or supportive vorticity anomalies that favor cyclogenesis [*Liebmann et al.*, 1994; *Maloney et al.*, 2000; *Hall et al.*, 2001]. A landmark study by *Camargo et al.* [2009] shifted this paradigm to focus instead on the thermodynamic effects of the MJO based on their decomposition of four key factors to the MJO's TC modulation through the Genesis Potential Index (GPI) [*Emanuel and Nolan,* 2004]. Their results argue for the dominance of the MJO's humidity envelope, as opposed to its shear or vorticity anomalies. This control-by-humidity argument (with varying degrees of secondary vorticity support) has prevailed in subsequent attempts to test causality through analogous GPI decompositions [*Huang et al.*, 2011; *Zhao et al.*, 2015a, 2015b; *You et al.*, 2018; *Zhao and Li*, 2018]. Such studies have since been challenged for their strong reliance on GPI as an index of causation, given its known limitations. The index exhibits a few biases relative to observations (i.e., showing anomalously positive values even in regions/seasons where no or few TCs are observed)

[*Tippett et al.*, 2011; *Bruyère et al.*, 2012], and *Wang and Moon* [2017] and *Moon et al.* [2018] argue that since GPI is based on climatology, it may be incapable of accurately capturing the intraseasonal TC variability associated with the MJO. *Moon et al.* [2018] thus developed a new intraseasonal genesis index for the West Pacific, suggesting a variety of dynamical factors as most important for determining cyclogenesis. Some high resolution modeling studies have also suggested dynamic controls as dominating over humidity [*Oouchi et al.*, 2009; *Kim et al.*, 2014].

In addition, many of the above studies employ various forms of pragmatic information loss via spatial aggregation, smoothing in space-time, and filtering that in hindsight could obscure subregional details of the underlying MJO/TC relationship. One symptom is that the MJO's modulation of TCs appears to be unsatisfyingly sensitive to details of how the MJO itself is defined, at least in studies that spatially aggregate the MJO's effects to large (100˚E-180˚W) basin-scales (*Table 4.1*). While such aggregation can be tempting to avoid sampling limitations given the relatively small number of TCs that have formed in each MJO phase, it is incongruous with the horizontal scales of the MJO's individual vorticity and thermodynamic anomalies. Meanwhile, even studies that take pains to avoid spatial aggregation suffer from information loss due to aggregation in time (e.g. grouping MJO phases into pairs) and smoothing in space and/or time [i.e., *Camargo et al.,* 2009; *Huang et al.*, 2011], or filtering to intraseasonal timescales [*Moon et al.,* 2018]. Such methodological issues may yet belie the complexity of how thermodynamic and dynamic effects conspire within certain subregions of the West Pacific to underpin the essence of MJO/TC modulation.

Table 4.1: Summary of methods and findings of the MJO-TC relationship in the West Pacific.

	Favorable (unfavorable) phases for TCs	**MJO indexing method**	**Filter boundaries for the MJO**	**Season considered (years)**
Huang et al. [2011]	Varies by region/season	EOFs of 30-90 day Lanczos filtered OLR, carried out in individual seasons and regions	100˚E-180˚E, (MJ) 10˚S-30˚N, (JAS) 10˚S-30˚N, (OND) 20˚S-20˚N	May-Dec, split seasonally (1979-2008)
Li and Zhou [2013]	1+2 (5+6)	EOF of 30-60 day bandpass filtered OLR	0˚-30˚N and 100˚E-180˚E	June-November (1975-2010)
Zhao et al. [2015b]	4-6 (1-3)	EEOF[1] of TRMM rainfall observations, which are bandpass filtered for 10-90 days	Analysis carried out with a lag of 31 days and a domain of 20˚S-30˚N and 60˚E-180˚E	May – October (1998-2012)
Klotzbach [2014]	6-7 (3-4)	RMM[2] Index	Assuming classical RMM definition: 15˚S-15˚N	June-November (1979-2012)
Klotzbach and Oliver [2015]	5+6 and 7+8 (1+2 and 3+4)	RMM Index + *Oliver and Thompson* (2012) reconstructed MJO back to 1905	Assuming classical RMM definition: 15˚S-15˚N	June-November (1945-2012)
You et al. [2018]	(RMM) 5-7, (EAWNP ISO-1[3]) 3-5, (BSISO-1[4]) 1, 7-8	20-70 day oscillation based on the RMM, EAWNP ISO-1 Index, and BSISO-1 Index	Assuming classical definitions: (RMM) 15˚S-15˚N	May-October (1982-2016)

[1] Extended Empirical Orthogonal Function
[2] Realtime Multi-variate MJO index [*Wheeler and Hendon*, 2004]
[3] East Asian and Western North Pacific Intraseasonal Oscillation [*Lin* 2013]
[4] Boreal Summer Intraseasonal Oscillation [*Lee et al.,* 2013]

			(EAWNP ISO-1) 10°S to 40°N, 90° to 150°E (BSISO-1) 10°S–40°N, 40°–160°E	

In light of this context (i.e. the surprising sensitivity of MJO-TC modulation to how the MJO is defined; the unresolved debate on its controls; critiques of using GPI alone; and the potential for information loss from smoothing or aggregation) – the goal of this study is to re-visit the investigation of *Camargo et al.* [2009] with three new twists. First, we use a novel explicit cyclone downscaling framework that results in thousands of synthetic TC tracks as an independent test. That is, before decomposing genesis *potential* to infer causality, we assess its validity versus explicit genesis under each phase of the MJO by creating a robust sample of synthetic TCs. Second, we impose another test of credibility based on the hypothesis that robust signals of MJO-TC modulation should be mostly insensitive to the choice of MJO index. Third, we avoid where possible potential sources of information loss through aggregation or filtering/smoothing, under the hypothesis that MJO-TC modulation may be a highly nonlinear process that is prone to happening within preferential hotspots, via a complex, time-evolving sequence of both dynamic and thermodynamic factors that might be otherwise obscured.

The results that follow will generally confirm these hypotheses and argue that West Pacific MJO-TC modulation in the current climate is not predominately controlled by either dynamics or thermodynamics alone, but rather by unsteady transient contributions from both, and preferentially within certain regions. An especially distinct geographic action

center is found in the South China Sea, where the MJO strongly modulates cyclogenesis by a progression of favorably reduced shear, followed by increased potential intensity, and finally relative humidity.

4.2 Data and methods

We separately define the MJO based on two commonly used indices: the Real-time Multivariate MJO (RMM) index [*Wheeler and Hendon,* 2004] and the OLR-only MJO Index (OMI) [*Kiladis et al.,* 2014] as retrieved from the Australian Bureau of Meteorology (http://www.bom.gov.au/climate/mjo/) and the US Earth System Research Laboratory (https://www.esrl.noaa.gov/psd/mjo/), respectively. Our working hypothesis is that, if the essential geographic structure of wind and humidity anomalies based on those two indices are not radically different at relatively large scales (confirmed in *Fig. C.1-C.3*), then neither should resulting derived metrics of MJO-TC interaction. In each case, days with an active MJO are identified when their amplitude meets or exceeds one standardized unit, and are included in analysis if they occur in the TC season of June-November [*Li and Zhou*, 2013; *Klotzbach*, 2014] during 1983-2013.

To create a set of expanded TC statistics that allow us to avoid aggregation, we use a prognostic TC track and intensity forecast model, developed at MIT by Kerry Emanuel with output from WindRiskTech LLC (http://www.windrisktech.com) [*Emanuel et al.*, 2006]. The model randomly seeds initial disturbances as weak warm-core vortices within a high-resolution atmosphere-ocean coupled framework, and has been successfully used in a number of previous studies [*Emanuel et al.*, 2008, 2010]. In its default use case, the MIT

model is built to ingest monthly averages of environmental variables to delineate the mean annual cycle, which is incompatible with application to faster intraseasonal variations. We overcome this challenge by creating separate annual cycle climatologies for each phase of the MJO. That is, we group days with an observed active MJO by their calendar month and MJO phase, resulting in a series of month-phase pairs that allow for the creation of eight separate phase-specific annual climatologies (Section C.1).

For each day in a phase-specific climatology, the following environmental variables are retrieved from ERA-Interim Reanalysis (ERA-I) [*Dee et al.,* 2011] and averaged as necessary: monthly means of sea surface temperature (SST), atmospheric profiles of temperature and humidity, and daily averages of zonal winds at 850 and 250 hPa. The MIT model uses these conditions to produce a set of 4,000 synthetic TC tracks in the West Pacific for each phase of the MJO as defined by both RMM and OMI. This much larger sample size allows us to move satisfyingly beyond basin-wide analysis of observed storms and purely environmental analysis.

The MIT model has been widely used and validated across a range of studies in other applications [*Emanuel et al,* 2008, 2010; *Emanuel* 2010; *Daloz et al,* 2015; *Sobel et al.,* 2019]. However, since this is the first attempt to apply the model to understand *intraseasonal* scale TC oscillations by the MJO, its performance is also confirmed here independently by comparing the MJO Phase 1-8 average from the downscaling results to both observations and GPI (*Fig. C.4-C.6*). Overall, the model shows good agreement with observations and represents an improvement over GPI in a few key features, particularly

with respect to spatial gradients in cyclogenesis. In a set of best track records from 1979-2015, there is a sharp northward boundary on tropical storm formations near 20-25˚N and a decrease in cyclogenesis eastward of 160-170˚E, both of which are well captured in the MIT model while GPI exhibits a distinct high bias in the northern third of the basin (*Fig. C.4, C.5)*. The downscaling itself has a few biases as well, including weaker cyclogenesis in the South China Sea and a southeastward shift of peak genesis compared to observations (*Fig. C.5*), but it captures well the overall TC region and its boundaries. Beyond its spatial realism, the MIT model can also capture seasonal shifts in the location of genesis, indicating a northward propagation of the most active development region between May and September that aligns with observations but is less well defined in GPI (*Fig. C.6*). As a whole then, this method stands as a reasonable one for assessing MJO modulation of cyclogenesis in the West Pacific, with improvements relative to relying solely on environmental GPI analysis.

4.3 Results

The MIT model's composite statistics reveal two stationary geographic action centers of especially strong MJO-TC modulation -- one located in the eastern half of the basin (the West-Central Pacific; Region 5 in *Fig. 4.1*) and one in the western half (the South China Sea region; Region 1 in *Fig. 4.1*), both of which exhibit strong MJO-based modulation of genesis density but at different phases. The results confirm that at sub-basin scales the MJO exhibits consistent patterns of TC modulation that are, for the most part, independent of how exactly the index underpinning the oscillation is defined (i.e., similar patterns in left vs. right column of *Fig. 4.1*). Interestingly, the patterns also suggest a more complicated

modulation of cyclogenesis than a straightforward eastward propagation following the MJO's humidity envelope, as suggested by previous studies [*Camargo et al.*, 2009; *Satoh et al.*, 2012; *Camargo and Wing*, 2016]. Instead, the two action centers here are enhanced independently during opposing phases, while the intervening regions remain relatively insensitive to the MJO's passage.

During the early and late phases of the MJO (Phases 1-2 and 7-8), simulated genesis density is particularly enhanced in the West-Central Pacific, defined as 160˚E-180˚W (Region 5) in *Figure 4.1*, where it is otherwise suppressed in Phases 3-6. Regions 1-3, which encompass the South China Sea and the Philippine Sea, are instead favored during these intermediate stages of the MJO, with the strongest levels of genesis density occurring there in Phases 2-5 as the convective center of the MJO clears the Maritime Continent. As a result, the West Pacific does not respond in a single consistent way to MJO forcing, but instead alternates where TCs are favored between the geographic extremes of the basin, while the middle portion (particularly Region 4; 140˚E-160˚E) maintains relatively consistent genesis density that is only weakly affected by the oscillation.

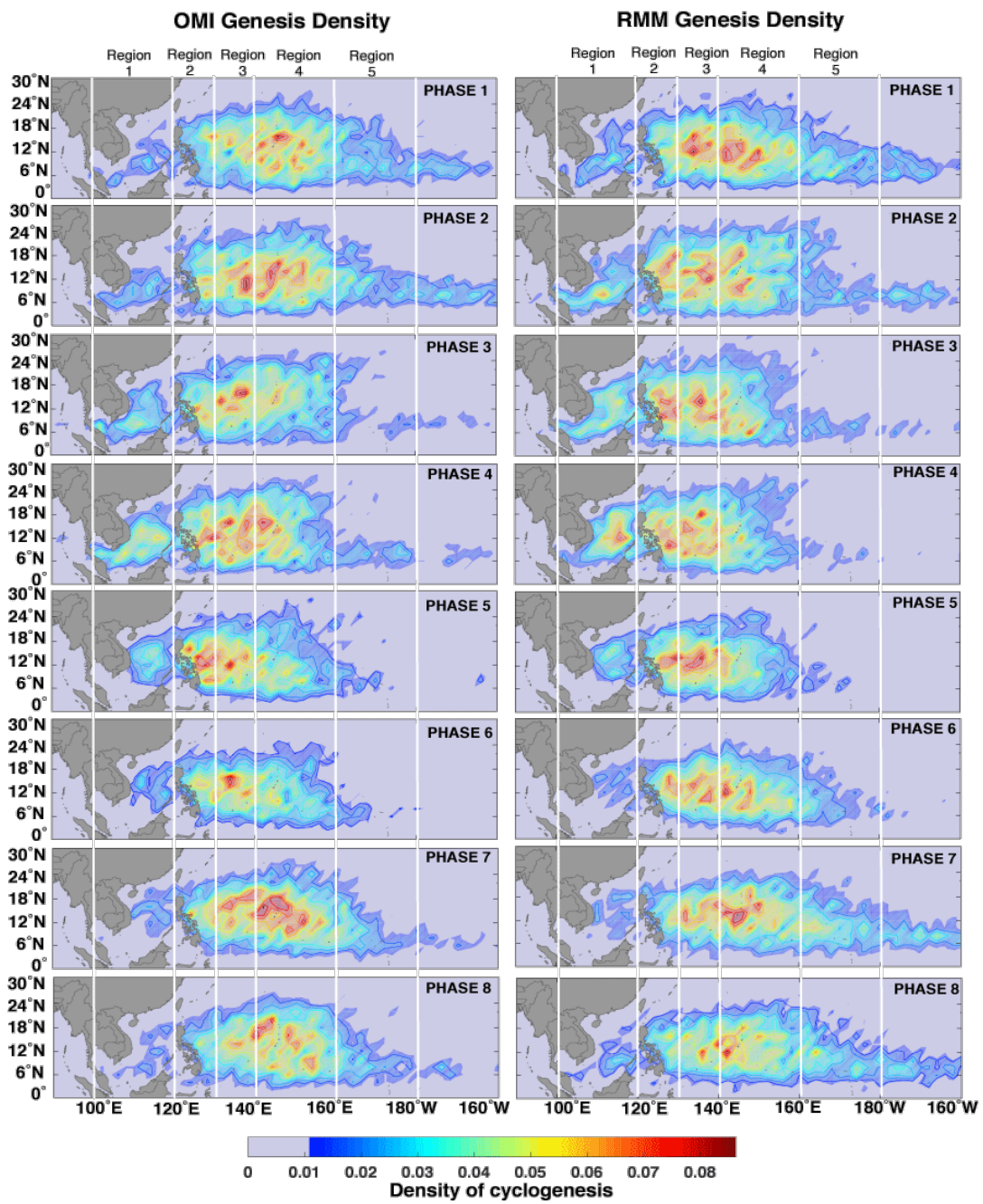

Figure 4.1: *Genesis density of MIT model generated storms in each phase of the MJO as defined by RMM (right) and OMI (left) during the active season (Jun-Nov). Boundaries of each sub-domain are marked in white.*

A propagation of the MJO's cyclogenesis modulation in directions other than straight eastward has been previously suggested by *Zhao et al.* [2015b] and *Huang et al.* [2011],

though the exact pattern suggested by each is different from the modes found here and in some respect from each other. *Zhao et al.* [2015b] find a northward propagation of TC genesis throughout Phases 4-8, while *Huang et al.* [2011] note a northeastward shift in genesis during Phases 1+2 and 3+4 relative to 7+8. Here, with substantially more TC tracks (albeit synthetic ones), we find the dominant pattern is better described not as a coherent propagation in any one direction, but rather as a set of two stationary modes wherein the MJO favors cyclogenesis either near the South China Sea (Phases 2-5) or the West-Central Pacific (Phases 1-2, 7-8).

To investigate the mechanisms responsible for these subregional patterns of TC modulation, we test whether the classical definition of GPI by *Emanuel and Nolan* [2004] produces congruent results with the MIT model. Though certainly prone to a number of limitations, including an inability to capture the multiple fine spatial details associated with cyclogenesis in the basin (*Fig. C.4-C.6*), GPI remains one of the most widely used indices for understanding the drivers of TC variability (which cannot be discerned through the MIT model output). We therefore limit our analysis to the region of 5-20˚N to avoid GPI's high bias in the northern portion of the West Pacific. Our working hypothesis is that if GPI alone reproduces the same subregional essence of the more explicit MIT modeling results, then it is likely reasonable to use in understanding which of its constituent factors,

$$GPI = |10^5\eta|^{\frac{3}{2}} \times \frac{H^3}{50} \times \frac{(V_{pot})^3}{70} \times (1 + 0.1V_{shear})^{-2} \qquad (4.1)$$

drive the MJO's modulation. In Equation (4.1), η is the 850 hPa absolute vorticity (s^{-1}), H is the 600 hPa relative humidity (%), V_{pot} is the maximum potential intensity (m s^{-1}), and V_{shear} is the vertical wind shear between 850 and 250 hPa (m s^{-1}). To calculate GPI, we follow the same procedure used for driving the MIT model by deriving eight separate annual cycle climatologies (at daily resolution) for each of its constituent variables, i.e. one for each phase of the MJO. Then, to estimate which MJO phase anomalies in GPI are statistically significant, we create a 100-member bootstrap ensemble of these yearly files to expose issues of sampling uncertainty.

To determine the contributions of each term to the overall GPI, we follow *Li et al.* [2013] and *Zhao and Li* [2018] in defining a differential based on the log form of the above equation:

$$\delta GPI = (\delta T1 \times \overline{T2} \times \overline{T3} \times \overline{T4}) + (\delta T2 \times \overline{T1} \times \overline{T3} \times \overline{T4}) + (\delta T3 \times \overline{T1} \times \overline{T2} \times \overline{T4}) + (\delta T4 \times \overline{T1} \times \overline{T2} \times \overline{T3}) \quad (4.2)$$

Where *T1-T4* correspond to each of the four terms above, overbars denote the mean (i.e. the average over all eight phases of the MJO in Jun-Nov within the phase climatology), and δ denotes the phase-specific deviation. The bootstrap ensemble mean GPI anomaly (δGPI) results are plotted in *Figure 4.2a* for each phase of the MJO and each of the five regions assessed (*Fig. 4.2b*).

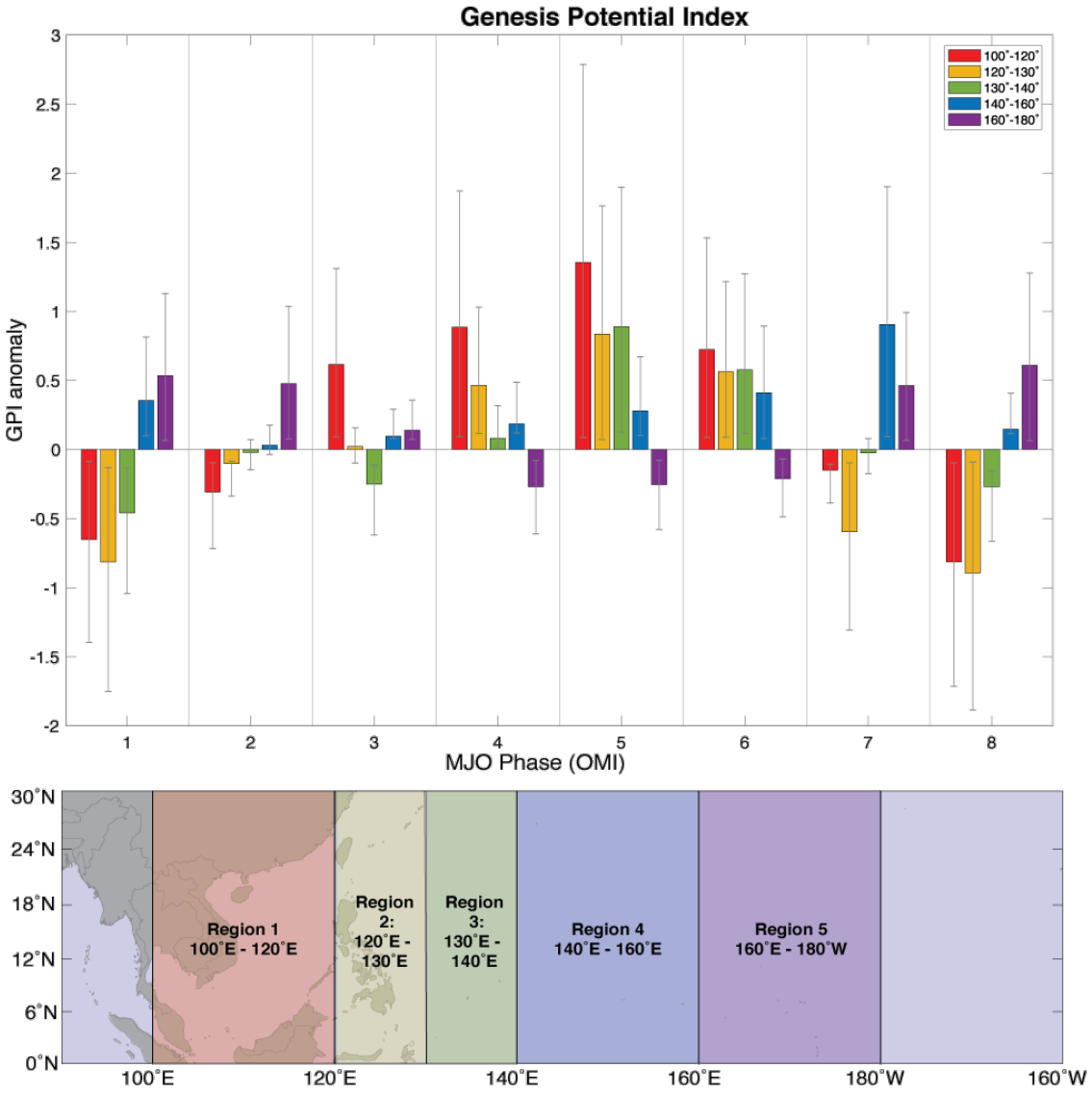

Figure 4.2*: (a) Anomalous GPI for each phase of the OMI-defined MJO (x-axis), relative to the Phase 1-8 mean, as computed in Equation 4.2. Each of the five regions outlined in (b) are assessed independently, shown as colored bars in (a), which represent the mean of the 100-member bootstrap for the TC season of June-November with error bars corresponding to the 25th and 75th percentiles of that analysis.*

Reassuringly, this GPI analysis reveals a similar pattern of TC modulation relative to the MIT model downscaling results (*Fig. C.7*). Again, there appear to be two distinct modes of modulation separated into east and west action centers. In the West-Central Pacific (purple

bars of *Fig. 4.2a*), the MJO enhances GPI in Phases 1-2 and 7-8, indicating an environment that is more favorable for cyclogenesis than during Phases 4-6. The western part of the basin (red, yellow, and green bars in *Fig. 4.2a*), however, shows the largest positive GPI anomalies in Phases 3-6 instead, suppressing genesis potential in Phases 1-2 and 7-8. As with the MIT model results, swapping RMM for OMI as the MJO index does not change these key features of the GPI decomposition (*Fig. C.8)*, thus passing our credibility test for a robust subregional signal of MJO-TC modulation. Based on this robustness and given that the strong agreement between it and MIT modeling results is unlikely to be a coincidence, we proceed assuming the GPI-based decomposition of relevant environmental factors is a reasonable approach for understanding the specific drivers of cyclogenesis modulation by the MJO.

We are now equipped to address the main question: why does the MJO preferentially modulate cyclogenesis in these hotspots? We begin with the South China Sea since, in both the MIT downscaling and GPI analysis, Region 1 stands out as being especially sensitive to MJO phase. It exhibits the largest range of GPI anomalies, and the downscaled genesis density shows one of the largest differences between mid- and early/late- phases of the MJO in this region as well.

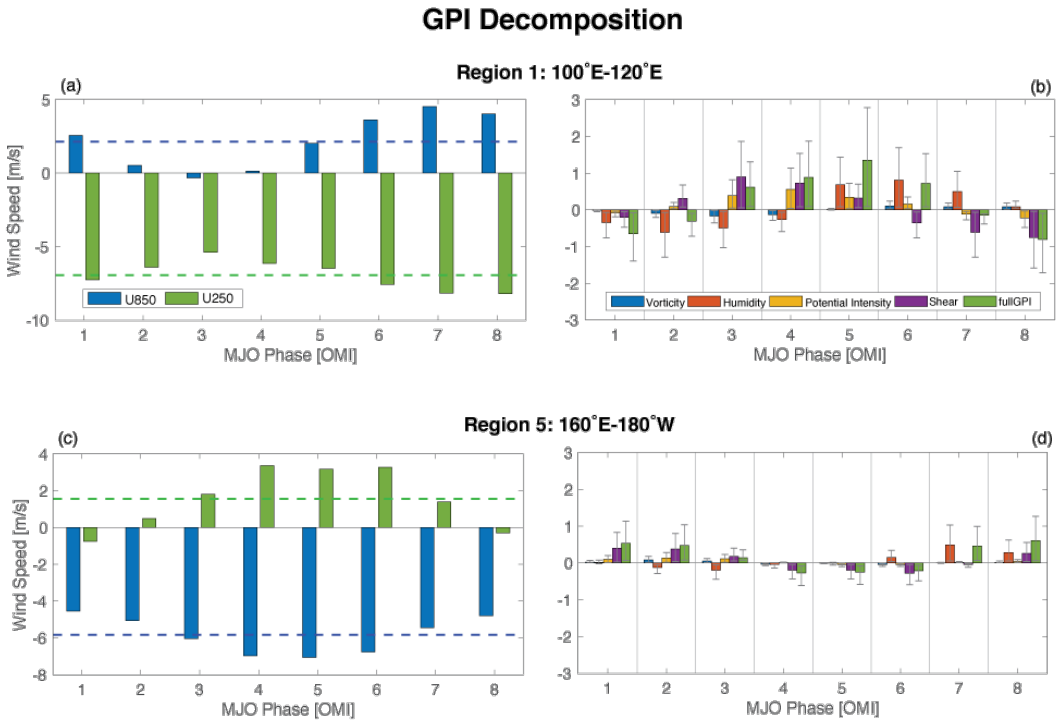

Figure 4.3*: (Left hand side) Average 850 (blue) and 250 mb (green) winds in the 100-member bootstrap ensemble for each phase of the MJO; dashed lines represent the Phase 1-8 mean. (Right hand side) Average GPI decomposition from Equation 4.2 for each phase of the MJO, taken from the 100-member bootstrap ensemble. Error bars correspond to the 25th and 75th percentiles as in Figure 4.2. These averages are taken for each region over the TC season of June-November.*

Assessing the individual drivers of GPI and the background winds at upper and lower levels suggests reasons why the South China Sea region is uniquely situated to be highly responsive to both convective and circulation anomalies associated with the MJO (*Fig. 4.3a, b*). Since this region is characterized by weak background low-level wind speeds (blue dashed line in *Fig. 4.3a*), the arriving sheared circulation anomaly is able to induce a reduction of the 850 mb zonal winds to near zero beginning in Phase 2. Beyond the straightforward effects of this reduced shear in promoting cyclogenesis, even before GPI increases (purple and green bars, respectively, in *Fig. 4.3b*), the drop in absolute low-level wind speed is especially important. Reduced winds reduce evaporative cooling and

turbulent mixing (i.e. reducing ocean mixed layer depths) – factors that can lead to a regional increase in SST anomalies (*Fig. C.9*), especially since ahead of the arrival of the convectively active portion of the MJO, i.e. during Phases 1-2, a positive OLR anomaly (i.e. clear skies) resides over the South China Sea (*Fig. C.1*). Together, these effects ultimately act to increase potential intensity support for cyclogenesis beginning in Phase 3 (yellow bars in *Fig. 4.3b; Fig. C.9*). This succession of increasing GPI support, first from shear and then potential intensity, is succeeded by the arriving relative humidity anomaly of the MJO, which increases in Phase 5, and acts to further support and sustain enhanced GPI through Phase 6 (orange bars in *Fig. 4.3b*).

The South China Sea region stands out as having the strongest trifold support from these successive drivers of regional GPI. While Regions 2 and 3 just to the east behave similarly in terms of sharing the same canonical GPI support led initially by reduced shear, followed by potential intensity and lastly relative humidity increases (*Fig. C.10*), they do not exhibit nearly as large of a total GPI modulation by the MJO as Region 1. We infer that the South China Sea region is special because it is situated geographically at an important location relative to the background Walker Cell, such that the MJO-induced reduction in shear coincides with near-zero low-level wind speeds. Together with clear skies this can support stronger, more sustained SST anomalies (*Fig. C.9*), leading to especially favorable conditions for MJO modulation of cyclogenesis through the potential intensity term, in addition to support from the shear and relative humidity.

In contrast, the second geographic action center in the West-Central Pacific (Region 5) shows a distinctly different cause of MJO-based GPI modulation (*Fig. 4.3d*). In a reversal of the previously described pattern, relative humidity increases are now the leading force of increased GPI during Phases 7-8 rather than the trailing one. Enhanced favorability for cyclogenesis is then sustained through Phases 1-2 by reductions in wind shear due to a reduction or reversal in upper level winds (*Fig. 4.3c*). Region 4 exhibits similar phasing – GPI is more heavily favored in the early and late phases of the MJO through similar mechanisms (*Fig. C.10*). But as in the case of MIT model genesis density, GPI anomalies remain consistently positive there throughout the MJO's lifecycle, making it difficult to conclude definitively that the MJO exerts a primary control on cyclogenesis in the region.

4.4 Discussion and conclusions

The boreal summer MJO has often been noted for its ability to modulate West Pacific cyclogenesis [*Liebmann et al.*, 1994; *Kim et al.*, 2008; *Camargo et al.*, 2009; *Huang et al.*, 2011; *Klotzbach*, 2014]. But disagreement on the drivers of that modulation, inconsistent signals depending on how the MJO is defined when its statistics are spatially aggregated, and questions about the limitations of GPI, have all limited robust conclusions about the underlying processes and their geographic details. Here, we have revisited the issue by making use of a quasi-explicit TC downscaling framework as well as multiple MJO index credibility testing, to identify new robust subregional action centers and understand their causality.

Our results are at odds with the paradigm that the MJO primarily influences TC genesis through relative humidity support in ways that propagate coherently alongside the MJO itself [*Camargo et al.*, 2009; *Satoh et al.*, 2012; *Camargo and Wing*, 2016]. In contrast, genesis density from the MIT model indicates a more complicated pattern of modulation in which distinct geographic action centers within the West Pacific respond disproportionately to the passage of the MJO and for different reasons. Two particular hotspots are modulated out of phase with one another, with the West-Central Pacific most active during Phases 1-2 and 7-8, while the South China Sea region is most active during Phases 3-5. The regions between these (120˚E-160˚E) remain generally favorable for cyclogenesis throughout the MJO's lifecycle.

In hindsight, these two stationary modes may be visible in previous studies as well. The phasing of the South China Sea favorability is roughly consistent with (though beginning a bit earlier than) *Camargo et al.* [2009] (their *Fig. 4*) and *Huang et al.* [2011] (their *Fig. 8*), and close inspection shows hints of a West-Central Pacific favorability region towards the beginning/ending phases of the MJO as well. *Kim et al.* [2014], in a high-resolution modeling study, found that increases in South China Sea cyclogenesis began in their simulated Phases 3+4 – a bit earlier than in raw observations but broadly in line with what we find.

To identify the mechanisms behind the MJO modulation observed in each action center, we employ a GPI decomposition similar to *Camargo et al.* [2009], given that GPI validates successfully against more explicit TC downscaling. We break tradition with most past

studies by intentionally avoiding spatial smoothing, space-time filtering, and especially MJO multi-phase aggregation. This helps reveal unsteady regional chronologies in which multiple GPI contributors vary rapidly by MJO phase while working in concert to amplify the overall anomaly. We readily acknowledge that there are limitations with all GPI-based approaches. *Tippett et al.* [2011], for example, note that GPI may be enhanced even in regions or seasons when TCs aren't observed. Such bias may be amplifying the West-Central Pacific signal, which is stronger in GPI than in the MIT model results, though the signal is still at least present in the downscaled genesis density and thus appears to be robust in its existence if questionable in amplitude.

The South China Sea region stood out in our analysis as the most prone to TC modulation by the MJO. Cyclogenesis there is strongly enhanced during the middle of the MJO's lifecycle via a reduced shear packet that precedes the convective anomaly. Due to favorable background low level winds, this can result in a local increase in SSTs, presumably due to strong interactions with surface ocean heat content linked to both wind anomaly-induced surface flux shutdown (and thermocline shoaling) as well as clear skies (anomalous sunlight) ahead of the arriving MJO. The resulting increase in potential intensity helps sustain positive GPI anomalies throughout Regions 1-3, before giving way to relative humidity support. This happy coincidence of three successive avenues of support for cyclogenesis is unique to the far western part of the Pacific basin and may explain why the decks are stacked there for an especially strong MJO modulation action center. Meanwhile, our findings support the view that both dynamic *and* thermodynamic factors are critical for MJO modulation of cyclogenesis in the West Pacific, particularly in the South China Sea. It is

interesting that the MJO's influence on potential intensity is found to play a non-negligible role for increasing GPI in this region, as this pathway is not typically emphasized as important. Future studies that examine the impacts of an amplified MJO on cyclogenesis in the West Pacific will thus likely benefit from doing so within a fully-coupled modeling framework that allows for evolving SSTs.

4.5 Acknowledgements

This study was conducted with primary funding from the Department of Energy Early Career Program (DE-SC0012152) and additional support from the NSF (AGS-1734164) and NASA MIRO (NNX15AQ06A). We extend our thanks to WindRiskTech LLC and Kerry Emanuel for his generation of the downscaling results and for helpful conversations regarding this work. The authors also thank Jim Randerson for helpful suggestions that served to greatly improve the manuscript.

Chapter 5

Conclusion

This dissertation is broadly motivated by the need to better understand current and future changes to the water cycle and its extremes. I have thus addressed three distinct points of interest: the effects of irrigation on non-local precipitation, the role of plant responses to rising CO_2 in altering future streamflow extremes across a range of scales, and the effects of the Madden-Julian Oscillation (MJO) on tropical cyclone (TC) formations in the West Pacific. The results from each study are summarized below, in addition to suggestions for future work based on these findings.

5.1 Non-local precipitation responses to irrigation

In Chapter 2, I addressed the impacts of irrigation on non-local precipitation with a focus on the Indian subcontinent, a particularly heavily irrigated and productive region. India is the second largest producer of agricultural products in the world, where irrigation accounts for 84% of total water use in the country while the agricultural sector as a whole employs more than half the population [*Dhawan*, 2017]. But despite the widespread and critically important role of irrigation in the nation, its impacts on non-local rainfall remain debated. In a particularly notable study on the topic, *de Vrese et al.* [2016] suggested that

irrigation in this region could have impacts in places as far away as Africa and Australia. Here, I have added to the debate surrounding the ability of irrigation to alter remote hydroclimates through the application of a novel ensemble approach.

The use of a wide hindcast ensemble has a number of benefits relative to previous attempts to constrain the relationship between precipitation and irrigation at long distances. This methodology has the important advantage of beating down internal variability, which is increasingly recognized for its ability to play a significant obscuring role in single model experiments [*Deser et al.*, 2012, 2014; *Kay et al.*, 2015; *Thiery et al.*, 2017] like those carried out by *de Vrese et al.* [2016] and *Lo and Famiglietti* [2013]. The number of ensembles used here -- 60 total members that span three initialization dates -- is particularly large and is made possible by a focus on short timescales (45 days each) rather than long climatological ones spanning multiple decades. This timescale also offers the benefit of being able to observe high frequency teleconnection mechanisms between Indian irrigation and potential non-local rainfall responses that operate on fast timescales.

This approach reveals a surprising sensitivity of the remote precipitation response to initialization date. Depending on the initial synoptic conditions, irrigation in northern India can alter precipitation over the Bay of Bengal, the Eastern Ghats region, or even the East China Sea. Such signals are found to be robust across sub-ensemble members (sets of 20 for each date) and amplify coherently when the level of irrigation is increased, suggesting that they are indeed robust despite their synoptic sensitivity. But those rainfall shifts are only observable at short lead times (the first 1-2 weeks). After that, internal variability grows to

dominate the signal and most remote precipitation changes lose their statistical significance (though the response in the Meiyu-Baiu region provides an exception to that generalization).

Overall, the findings at fast timescales suggests the importance of additional hindcast-style ensemble experiments to compliment longer running climatological studies of irrigation's effects on non-local precipitation. Ideally, individual experiments would be designed to allow irrigation only in pre-defined regions (only in India for one set of experiments, the Central Valley for another, etc.) to isolate individually driven responses. This task should span an array of GCMs to understand not only the role of internal variability but also the possible range of multi-model spread, which remains unconstrained on the topic of irrigation-precipitation interactions today. The underlying mechanism behind the sensitivity of remote precipitation responses to atmospheric synoptic conditions when irrigation is applied is also of interest. Further analysis will be required to link individual rainfall patterns to Indian irrigation under various environmental conditions and to better understand how and why that variability exists.

5.2 Flood and streamflow responses to future plant-physiological changes

In Chapter 3, I assessed the relative ability of the plant-physiological response to rising CO_2 to alter flooding and streamflow relative to the radiative response. That is, the transpiration, leaf area index (LAI), and subsequent soil moisture changes that arise from reduced stomatal conductance and carbon fertilization were compared against the

temperature and precipitation responses of the atmosphere under CO_2 concentrations that were four times larger than pre-industrial levels. The relative importance of these two effects has not been adequately addressed in the context of hydrologic extremes previously.

One of the reasons for the relative dearth of studies on this topic is the volume of ongoing debate surrounding plant responses to rising CO_2. Its effects on streamflow in particular remain highly uncertain for much of the globe. *Gedney et al.* [2006] were among the first to suggest that effects of plant-physiological changes were already observable in global discharge records, while others argued that precipitation changes were dominant instead if the carbon fertilization effect of increased LAI was also properly accounted for [*Piao et al.*, 2007; *Gerten et al.*, 2008]. More recently, observed streamflow declines in Australia have been linked to the carbon fertilization effect, suggesting its dominance over stomatal conductance changes in particularly dry regions [*Ukkola et al.*, 2016; *Trancoso et al.*, 2017]. But the overall strength of each effect remains unclear in observations, highlighting the need for additional extended experiments to properly constrain the strength of both plant responses at global scales.

Despite the amount of uncertainty surrounding the future vegetation response, it is essential to understand its potential to alter future streamflow and high-impact flood events. Projections of changes in these terrestrial hydrologic components are critical to infrastructure planning and mitigation and are often made with the caveat of significant uncertainty surrounding the driving force of precipitation due to GCM biases (i.e.,

Hirabayashi et al. [2013]), but rarely acknowledge similar uncertainty in soil moisture changes driven by plant-physiology. In this chapter, I show that it is equally important to constrain the land surface changes used to build these projections as it is to improve the atmospheric model component. Flood responses are in fact found to be of comparable magnitude when forced by either the physiological or radiative changes alone, while more observable streamflow extremes can occur almost exclusively as a result of plant responses. Particularly for the heavily vegetated and sunlit tropics, including these effects is thus of first order importance for properly representing the range of possible futures in river projections.

There are, however, a few caveats on this work. Most critically, the findings of which basins respond most strongly to the physiological effect and the magnitude of that response is based on only a single model, and a single iteration at that. Confidence is built through comparing CMIP5 multi-model means with the Community Earth System Model (CESM) experiment that allows both CO_2 response pathways to be active (*FULL*), which indicates that the total climate change response is at least reasonable. But the range of possible simulated physiological and radiative responses are not placed in the context of additional models due to limited data availability. Daily runoff is a relatively rare output to have been saved in the IPCC's C4MIP campaign thus far, at least for all four of the experiments needed to duplicate the experiment design used here. It is thus recommended that additional GCMs begin saving daily output for critical components of the land model such as this. It would also be valuable to assess the strength of the plant-physiological effect in simulations that can more accurately represent the precipitation distribution, as in super-parameterized

versions of CESM, to focus more directly on vegetation response uncertainty without potentially biasing its importance as the result of a known drizzle problem in the atmospheric component of the model.

A number of additional observational studies will also likely be necessary to better constrain the magnitude of the plant responses to rising CO_2 across a wider range of spatial and temporal scales than are available today. Four tropical river basins in particular are suggested in Chapter 3 as potentially promising locations for this endeavor – the Amazon, Parana, Congo, and Yangtze. Additional carbon enrichment experiments there or regional modeling efforts that aim to match observed streamflow changes to various levels of land and atmospheric forcing could better constrain the plant-physiological effect in nature and aid its inclusion in land surface models.

5.3 Present day TC modulation in the West Pacific by the MJO

In Chapter 4, I explored how the MJO can alter TC formations in the West Pacific. Though the topic has received considerable attention previously, a number of open questions remain regarding the mechanisms behind the modulation. Debates have continued on what it is about the MJO that results in its ability to strongly affect cyclogenesis in the basin; it could be the enhanced relative humidity associated with its convective envelope, in which case regions of enhanced TC formations could be expected to propagate eastward along with the MJO itself as suggested by a number of studies that have made use of the Genesis Potential Index (GPI) [*Huang et al.*, 2011; *Zhao et al.*, 2015a, 2015b; *You et al.*, 2018; *Zhao and Li*, 2018]. But the modulation could also result from dynamic changes induced by the

overall circulation anomaly rather than the MJO's convection, which include reductions of vertical wind shear and the creation of favorable vorticity anomalies that tend to encourage TC formations [*Liebmann et al.*, 1994; *Maloney et al.*, 2000; *Hall et al.*, 2001; *Tippett et al.*, 2011; *Wang and Moon*, 2017; *Moon et al.*, 2018].

Through a novel downscaling framework, I suggest that the story is in fact more complicated than previously suggested by either argument alone. Sets of thousands of synthetic TC tracks generated from environmental conditions indicative of each phase of the MJO individually helps remove the need for spatial or temporal aggregation (as in *Camargo et al.,* [2009]; *Huang et al.*, [2011]; *Moon et al.*, [2018]) that could mask regionally varying signals and their transient controls. The results of Chapter 4 suggest that instead of a straightforward eastward propagating signal of cyclogenesis with the MJO as suggested previously [*Camargo et al.*, 2009; *Satoh et al.*, 2012; *Camargo and Wing*, 2016], the oscillation influences West Pacific TCs through two distinct stationary modes centered on opposite sides of the basin that are favored out of phase with one another. The South China Sea region and West-Central Pacific hotspots are confirmed across two definitions of the MJO (a source of apparent previous disagreement at basin levels; see *Table 4.1*) and in regional GPI analysis, which provides insight to the underlying mechanisms behind this pattern.

The South China Sea is found to be uniquely situated so as to be especially susceptible to the passage of the MJO. Climatologically weak near-surface winds reduce their speeds even further to near-zero in Phase 2 of the oscillation as vertical wind shear declines, reducing

turbulent mixing and evaporative cooling of the surface ocean layer, increasing sea surface temperatures (SSTs). This enhances initial SST increases driven by suppressed convection in the region during Phases 1-2 to increase potential intensity beginning in Phase 3, of which SST is a key component. Both shear and potential intensity support help to increase anomalous GPI in the region during Phases 3-4, before the arrival of the convective packet and its enhanced relative humidity, which act to sustain the positive GPI anomaly through Phase 6.

It is worth acknowledging, however, that this mechanism of MJO-TC modulation is based on a single genesis potential metric; an expansion to additional indices or a more detailed statistical analysis of a wide array of environmental variables could help support the existence of transient controls between dynamic and thermodynamic factors. It also remains to be seen if similar signals of MJO modulation are present in the current generation of climate models. This task will be especially important given the projected amplification of the MJO in state-of-the-art climate models [*Arnold et al.*, 2014, 2015; *Chang et al.*, 2015; *Adames et al.*, 2017; *Wolding et al.*, 2017; *Maloney et al.*, 2019].

Multiple studies now suggest that MJO-related precipitation will intensify, often explained by increases in the vertical moisture gradient, which make convective heating anomalies more efficient at building up and holding moisture in the atmosphere, and by increases in vertical velocity within the convectively active region [*Arnold et al.*, 2014; *Chang et al.*, 2015; *Maloney et al.*, 2019]. A number of studies have also suggested that MJO events could become more frequent, increase their propagation speed, and expand further eastward into

the Central and East Pacific regions [*Arnold et al.*, 2014; *Adames et al.*, 2017; *Maloney et al.*, 2019]. The latter effect – an expansion eastward of the MJO's convective center – could have especially interesting consequences in light of the MJO-TC action center highlighted there in Chapter 4. Though only a relatively small number of storms have been observed in the West-Central Pacific during active MJO events thus far, global warming simulations have suggested an expansion of genesis into the region due to changes in El Niño characteristics [*Yokoi et al.*, 2009], which may allow the MJO modulation to project more clearly onto observations there in the coming decades. In general, given the existence of transient controls on the MJO-TC relationship and the phase/regional dependency of that modulation, it will be important to carefully analyze West Pacific TC signals at sub-basin scales to determine the overall effect of an amplified MJO on cyclogenesis.

Bibliography

Adames, A. F., D. Kim, A. H. Sobel, A. Del Genio, and J. Wu (2017), Changes in the structure and propagation of the MJO with increasing CO_2, *J. Adv. Model. Earth Syst.*, *9*, 1–18, doi:10.1002/2017MS000913.

Ainsworth, E. A., and S. P. Long (2004), What have we learned from 15 years of free-air CO_2 enrichment (FACE)? A meta-analytic review of the responses of photosynthesis, canopy properties and plant production to rising CO_2, *New Phytol.*, *165*(2), 351–372, doi:10.1111/j.1469-8137.2004.01224.x.

Allan, R. P., and B. J. Soden (2008), Atmospheric warming and the amplification of precipitation extremes, *Science*, *321*(5895), 1481–1484, doi:10.1126/science.1103215.

Alter, R. E., Y. Fan, B. R. Lintner, and C. P. Weaver (2015), Observational evidence that Great Plains irrigation has enhanced summer precipitation intensity and totals in the Midwestern US, *J. Hydrometeorol.*, *16*, 1717–1736, doi:10.1175/JHM-D-14-0115.1.

Anderson, R. G., M.-H. Lo, and J. S. Famiglietti (2012), Assessing surface water consumption using remotely-sensed groundwater, evapotranspiration, and precipitation, *Geophys. Res. Lett.*, *39*(16), doi:10.1029/2012GL052400.

Anderson, R. G., M. H. Lo, S. Swenson, J. S. Famiglietti, Q. Tang, T. H. Skaggs, Y. H. Lin, and R. J. Wu (2015), Using satellite-based estimates of evapotranspiration and groundwater changes to determine anthropogenic water fluxes in land surface models, *Geosci. Model Dev.*, *8*(10), 3021–3031, doi:10.5194/gmd-8-3021-2015.

Arnold, N. P., M. Branson, M. A. Burt, D. S. Abbot, Z. Kuang, D. A. Randall, and E. Tziperman (2014), Effects of explicit atmospheric convection at high CO_2, *PNAS*, *111*(30), 10943–10948, doi:10.1073/pnas.1407175111.

Arnold, N. P., M. Branson, Z. Kuang, D. A. Randall, and E. Tziperman (2015), MJO intensification with warming in the superparameterized CESM, *J. Clim.*, *28*(7), 2706–2724, doi:10.1175/JCLI-D-14-00494.1.

Arora, V. K. et al. (2013), Carbon–concentration and carbon–climate feedbacks in CMIP5 earth system models, *J. Clim.*, *26*, 5289–5314, doi:10.1175/JCLI-D-12-00494.1.

Barnston, a. G., and P. T. Schickedanz (1984), The effect of irrigation on warm season precipitation in the southern great plains, *J. Clim. Appl. Meteorol.*, *23*, 865–888,

doi:10.1175/1520-0450(1984)023<0865:TEOIOW>2.0.CO;2.

Betts, R. A. et al. (2007), Projected increase in continental runoff due to plant responses to increasing carbon dioxide, *Nature*, *448*, 1037–1041, doi:10.1038/nature06045.

Boucher, O., G. Myhre, and A. Myhre (2004), Direct human influence of irrigation on atmospheric water vapour and climate, *Clim. Dyn.*, *22*(6–7), 597–603, doi:10.1007/s00382-004-0402-4.

Bruyère, C. L., G. J. Holland, and E. Towler (2012), Investigating the use of a genesis potential index for tropical cyclones in the North Atlantic basin, *J. Clim.*, *25*, 8611–8626, doi:10.1175/JCLI-D-11-00619.1.

Camargo, S. J., and A. A. Wing (2016), Tropical cyclones in climate models, *WIREs Clim Chang.*, *7*, 211–237, doi:10.1002/wcc.373.

Camargo, S. J., M. C. Wheeler, and A. H. Sobel (2009), Diagnosis of the MJO modulation of tropical cyclogenesis using an empirical index, *J. Atmos. Sci.*, *66*(10), 3061–3074, doi:10.1175/2009JAS3101.1.

Campbell, J. et al. (2017), Assessing a new clue to how much carbon plants take up, *Eos*, *98*, doi:10.1029/2017EO075313.

Cao, L., G. Bala, K. Caldeira, R. Nemani, and G. Ban-Weiss (2010), Importance of carbon dioxide physiological forcing to future climate change, *PNAS*, *107*(21), 9513–9518.

Chang, C.-W. J., W.-L. Tseng, H.-H. Hsu, N. Keenlyside, and B.-J. Tsuang (2015), The Madden-Julian Oscillation in a warmer world, *Geophys. Res. Lett.*, *42*(14), 6034–6042, doi:10.1002/2015GL065095.

Chou, C., C. Chen, P. Tan, and K. T. Chen (2012), Mechanisms for global warming impacts on precipitation frequency and intensity, *J. Clim.*, *25*, 3291–3306, doi:10.1175/JCLI-D-11-00239.1.

Christensen, J. H. et al. (2013), Climate phenomena and their relevance for future regional climate change, in *Climate Change 2013: The Physical Science Basis. Contribution of Working Group I to the Fifth Assessment Report of the Intergovernmental Panel on Climate Change*, edited by T. F. Stocker, D. Qin, G.-K. Plattner, M. Tignor, S. K. Allen, J. Boschung, A. Nauels, Y. Xia, V. Bex, and P. M. Midgley, Cambridge University Press, Cambridge, United Kingdom and New York, NY, USA.

Cook, B. I., G. B. Bonan, and S. Levis (2006), Soil moisture feedbacks to precipitation in Southern Africa, *J. Clim.*, *19*(17), 4198–4206, doi:10.1175/JCLI3856.1.

Daloz, A.S. et al (2015), Cluster Analysis of Downscaled and Explicitly Simulated North Atlantic Tropical Cyclone Tracks, *J. Clim.*, *28*, 1333–1361, doi:10.1175/JCLI-D-13-

00646.1.

Dankers, R., and L. Feyen (2008), Climate change impact on flood hazard in Europe: An assessment based on high-resolution climate simulations, *J. Geophys. Res.*, *113*, doi:10.1029/2007JD009719.

Davis, K. F., M. C. Rulli, F. Garrassino, D. Chiarelli, A. Seveso, and P. D'Odorico (2017), Water limits to closing yield gaps, *Adv. Water Resour.*, *99*, 67–75, doi:10.1016/j.advwatres.2016.11.015.

DeAngelis, A., F. Dominguez, Y. Fan, A. Robock, M. D. Kustu, and D. Robinson (2010), Evidence of enhanced precipitation due to irrigation over the Great Plains of the United States, *J. Geophys. Res. Atmos.*, *115*(15), 1–14, doi:10.1029/2010JD013892.

DeAngelis, A. M., X. Qu, and A. Hall (2016), Importance of vegetation processes for model spread in the fast precipitation response to CO_2 forcing, *Geophys. Res. Lett.*, *43*(24), 12550–12559, doi:10.1002/2016GL071392.

Dee, D. P. et al. (2011), The ERA-Interim reanalysis: configuration and performance of the data assimilation system, *Q. J. R. Meteorol. Soc.*, *137*(656), 553–597, doi:10.1002/qj.828.

DeMott, C. A., J. J. Benedict, N. P. Klingaman, S. J. Woolnough, and D. A. Randall (2016), Diagnosing ocean feedbacks to the MJO: SST-modulated surface fluxes and the moist static energy budget, *J. Geophys. Res. Atmos.*, *121*(14), 8350–8373, doi:10.1002/2016JD025098.

Deser, C., R. Knutti, S. Solomon, and A. S. Phillips (2012), Communication of the role of natural variability in future North American climate, *Nat. Clim. Chang.*, *2*, 1–19, doi:10.1038/nclimate1562.

Deser, C., A. S. Phillips, M. A. Alexander, and B. V. Smoliak (2014), Projecting North American climate over the next 50 years: Uncertainty due to internal variability, *J. Clim.*, *27*(6), 2271–2296, doi:10.1175/JCLI-D-13-00451.1.

Doll, P., and S. Siebert (2002), Global modeling of irrigation water requirements, *Water Resour.*, *38*(4), doi:10.1029/2001WR000355.

Douglas, E. M., D. Niyogi, S. Frolking, J. B. Yeluripati, R. A. Pielke, N. Niyogi, C. J. Vörösmarty, and U. C. Mohanty (2006), Changes in moisture and energy fluxes due to agricultural land use and irrigation in the Indian Monsoon Belt, *Geophys. Res. Lett.*, *33*(14), 1–5, doi:10.1029/2006GL026550.

Eisner, S. et al. (2017), An ensemble analysis of climate change impacts on streamflow seasonality across 11 large river basins, *Clim. Change*, *141*(3), 401–417, doi:10.1007/s10584-016-1844-5.

Emanuel, K., and D. S. Nolan (2004), Tropical cyclone activity and the global climate system, in *26th Conference on Hurricanes and Tropical Meteorolgy*, pp. 240–241, Miami, FL.

Emanuel, K., S. Ravela, E. Vivant, and C. Risi (2006), A statistical deterministic approach to hurricane risk assessment, *Bull. Am. Meteorol. Soc.*, *19*, 299–314, doi:10.1175/BAMS-87-3-299.

Emanuel, K., R. Sundararajan, J. Williams, K. Emanuel, R. Sundararajan, and J. Williams (2008), Hurricanes and global warming: Results from downscaling IPCC AR4 simulations, *Bull. Am. Meteorol. Soc.*, *89*(3), 347–367, doi:10.1175/BAMS-89-3-347.

Emanuel, K. (2010), Tropical cyclone activity downscaled from NOAA-CIRES Reanalysis, 1908–1958, *J. Adv. Model. Earth Syst.*, *2*(1), 1, doi:10.3894/JAMES.2010.2.1.

Emanuel, K., K. Oouchi, M. Satoh, H. Tomita, and Y. Yamada (2010), Comparison of explicitly simulated and downscaled tropical cyclone activity in a high-resolution global climate model, *J. Adv. Model. Earth Syst.*, *2*, doi:10.3894/JAMES.2010.2.9.

FAO (2016), La Plata Basin, *AQUASTAT Main Database, Food Agric. Organ. United Nations*. Available from: http://www.fao.org/nr/water/aquastat/basins/la-plata/index.stm.

Frank, W. M., and P. E. Roundy (2006), The role of tropical waves in tropical cyclogenesis, *Mon. Wea. Rev.*, *134*, 2397–2417.

Friedlingstein, P. et al. (2006), Climate–carbon cycle feedback analysis: results from the C4MIP model intercomparison, *J. Clim.*, *19*(14), 3337–3353, doi:10.1175/JCLI3800.1.

Gedney, N., P. M. Cox, R. A. Betts, O. Boucher, C. Huntingford, and P. A. Stott (2006), Detection of a direct carbon dioxide effect in continental river runoff records, *Nature*, *439*, 835–838, doi:10.1038/nature04504.

Gerten, D., S. Rost, W. von Bloh, and W. Lucht (2008), Causes of change in 20th century global river discharge, *Geophys. Res. Lett.*, *35*(20), doi:10.1029/2008GL035258.

Hall, J. D., A. J. Matthews, D. J. Karoly, J. D. Hall, A. J. Matthews, and D. J. Karoly (2001), The modulation of tropical cyclone activity in the Australian region by the Madden-Julian Oscillation, *Mon. Weather Rev.*, *129*(12), 2970–2982, doi:10.1175/1520-0493(2001)129<2970:TMOTCA>2.0.CO;2.

Handmer, J. et al. (2012), Changes in impacts of climate extremes: human systems and ecosystems, in *A Special Report of Working Groups I and II of the Intergovernmental Panel on Climate Change*, edited by C. B. Field et al., pp. 231–290, Cambridge University Press, Cambridge, United Kingdom and New York, NY, USA.

Harding, K. J., and P. K. Snyder (2012), Modeling the atmospheric response to irrigation in the Great Plains. Part I: General impacts on precipitation and the energy budget, *J.*

Hydrometeorol., *13*(6), 1667–1686, doi:10.1175/JHM-D-11-098.1.

Harding, K. J., T. E. Twine, and Y. Lu (2015), Effects of dynamic crop growth on the simulated precipitation response to irrigation, *Earth Interact.*, *19*, doi:10.1175/EI-D-15-0030.1.

Hickler, T., B. Smith, I. C. Prentice, K. Mjofors, P. Miller, A. Arneth, and M. T. Sykes (2008), CO_2 fertilization in temperate FACE experiments not representative of boreal and tropical forests, *Glob. Chang. Biol.*, *14*(7), 1531–1542, doi:10.1111/j.1365-2486.2008.01598.x.

Hirabayashi, Y., S. Kanae, S. Emori, T. Oki, and M. Kimoto (2008), Global projections of changing risks of floods and droughts in a changing climate, *Hydrol. Sci. J.*, *53*(4), 754–772, doi:10.1623/hysj.53.4.754.

Hirabayashi, Y., R. Mahendran, S. Koirala, L. Konoshima, D. Yamazaki, S. Watanabe, H. Kim, and S. Kanae (2013), Global flood risk under climate change, *Nat. Clim. Chang.*, *3*(9), 816–821, doi:10.1038/nclimate1911.

Hohenegger, C., P. Brockhaus, C. S. Bretherton, and C. Schär (2009), The soil moisture-precipitation feedback in simulations with explicit and parameterized convection, *J. Clim.*, *22*(19), 5003–5020, doi:10.1175/2009JCLI2604.1.

Hovenden, M., and P. Newton (2018), Plant responses to CO_2 are a question of time, *Science*, *360*(6386), 263–264, doi:10.1126/science.aat2481.

Huang, P., C. Chou, and R. Huang (2011), Seasonal modulation of tropical intraseasonal oscillations on tropical cyclone geneses in the Western North Pacific, *J. Clim.*, *24*(24), 6339–6352, doi:10.1175/2011JCLI4200.1.

Huang, X., and P. A. Ullrich (2016), Irrigation impacts on California's climate with the variable-resolution CESM, *J. Adv. Model. Earth Syst.*, *8*, 1151–1163, doi:10.1002/2016MS000656.

Hunke, E. C., and W. H. Lipscomb (2010), *CICE: the Los Alamos Sea Ice Model Documentation and Software User's Manual Version 4.1 (Tech. Rep. LA-CC-06-012)*.

Hurrell, J. W. et al. (2013), The Community Earth System Model: A framework for collaborative research, *Bull. Am. Meteorol. Soc.*, *94*, 1339–1360, doi:10.1175/BAMS-D-12-00121.1.

Ivancic, T. J., and S. B. Shaw (2015), Examining why trends in very heavy precipitation should not be mistaken for trends in very high river discharge, *Clim. Change*, *133*, 681–693, doi:10.1007/s10584-015-1476-1.

Jiménez Cisneros, B. E., T. Oki, N.W. Arnell, G. Benito, J.G. Cogley, P. Döll, T. Jiang, and S.S.

Mwakalila (2014), Freshwater Resources, in *Climate Change 2014: Impacts, Adaptation, and Vulnerability. Part A: Global and Sectoral Aspects. Contribution of Working Group II to the Fifth Assessment Report of the Intergovernmental Panel on Climate Change*, edited by C. B. Field et al., pp. 229–269, Cambridge University Press, Cambridge, United Kingdom and New York, NY, USA.

De Kauwe, M. G. et al. (2013), Forest water use and water use efficiency at elevated CO_2: a model-data intercomparison at two contrasting temperate forest FACE sites, *Glob. Chang. Biol.*, *19*(6), 1759–1779, doi:10.1111/gcb.12164.

Keller, K. M. et al. (2017), 20th century changes in carbon isotopes and water-use efficiency: tree-ring-based evaluation of the CLM4.5 and LPX-Bern models, *Biogeosciences*, *14*(10), 2641–2673, doi:10.5194/bg-14-2641-2017.

Kiladis, G. N., J. Dias, K. H. Straub, M. C. Wheeler, S. N. Tulich, K. Kikuchi, K. M. Weickmann, and M. J. Ventrice (2014), A comparison of OLR and circulation-based indices for tracking the MJO, *Mon. Weather Rev.*, *142*(5), 1697–1715, doi:10.1175/MWR-D-13-00301.1.

Kim, D., M.-I. Lee, H.-M. Kim, S. D. Schubert, and J. H. Yoo (2014), The modulation of tropical storm activity in the Western North Pacific by the Madden-Julian Oscillation in GEOS-5 AGCM experiments, *Atmos. Sci. Lett.*, *15*(4), 335–341, doi:10.1002/asl2.509.

Kim, J.-H., C.-H. Ho, H.-S. Kim, C.-H. Sui, and S. K. Park (2008), Systematic variation of summertime tropical cyclone activity in the Western North Pacific in relation to the Madden–Julian Oscillation, *J. Clim.*, *21*(6), 1171–1191, doi:10.1175/2007JCLI1493.1.

Klotzbach, P. J. (2014), The Madden–Julian Oscillation's impacts on worldwide tropical cyclone activity, *J. Clim.*, *27*(6), 2317–2330, doi:10.1175/JCLI-D-13-00483.1.

Klotzbach, P. J., and E. C. J. Oliver (2015), Variations in global tropical cyclone activity and the Madden-Julian Oscillation since the midtwentieth century, *Geophys. Res. Lett.*, *42*(10), 4199–4207, doi:10.1002/2015GL063966.

Knutson, T. R., J. L. McBride, J. Chan, K. Emanuel, G. Holland, C. Landsea, I. Held, J. P. Kossin, A. K. Srivastava, and M. Sugi (2010), Tropical cyclones and climate change, *Nat. Geosci.*, *3*(3), 157–163, doi:10.1038/ngeo779.

Koirala, S., Y. Hirabayashi, R. Mahendran, and S. Kanae (2014), Global assessment of agreement among streamflow projections using CMIP5 model outputs, *Environ. Res. Lett.*, *9*(6), 1–11, doi:10.1088/1748-9326/9/6/064017.

Kooperman, G. J., M. S. Pritchard, M. A. Burt, M. D. Branson, and D. A. Randall (2016), Impacts of cloud superparameterization on projected daily rainfall intensity climate changes in multiple versions of the Community Earth System Model, *J. Adv. Model. Earth Syst.*, *8*, 1727–1750, doi:10.1002/2016MS000715.

Kooperman, G. J., Y. Chen, F. M. Hoffman, C. D. Koven, K. Lindsay, M. S. Pritchard, A. L. S. Swann, and J. T. Randerson (2018a), Forest response to rising CO_2 drives zonally asymmetric rainfall change over tropical land, *Nat. Clim. Chang.*, *8*(5), 434–440, doi:10.1038/s41558-018-0144-7.

Kooperman, G. J., M. D. Fowler, F. M. Hoffman, C. D. Koven, K. Lindsay, M. S. Pritchard, A. L. S. Swann, and J. T. Randerson (2018b), Plant-physiological responses to rising CO_2 modify simulated daily runoff intensity with implications for global-scale flood risk assessment, *Geophys. Res. Lett.*, *45*, 1–10, doi:10.1029/2018GL079901.

Krishnamurti, T. N., L. Stefanova, and M. Vasubandhu (2013), Madden Julian Oscillation, in *Tropical Meteorology: An Introduction*, pp. 143–168, Springer Atmospheric Sciences, New York.

Kueppers, L. M., and M. A. Snyder (2012), Influence of irrigated agriculture on diurnal surface energy and water fluxes, surface climate, and atmospheric circulation in California, *Clim. Dyn.*, *38*(5–6), 1017–1029, doi:10.1007/s00382-011-1123-0.

Kueppers, L. M., M. A. Snyder, and L. C. Sloan (2007), Irrigation cooling effect: Regional climate forcing by land-use change, *Geophys. Res. Lett.*, *34*(3), 1–5, doi:10.1029/2006GL028679.

Kundzewicz, Z. W. et al. (2014), Flood risk and climate change: global and regional perspectives, *Hydrol. Sci. J.*, *59*(1), 1–28, doi:10.1080/02626667.2013.857411.

Landsea, C., and S. Delgado (2017), What are the average, most, and least tropical cyclones occurring in each basin?, *Hurric. Res. Devision Atl. Oceanogr. Meteorol. Lab. - Freq. asked Quest.* Available from: https://www.aoml.noaa.gov/hrd/tcfaq/E10.html

Langenbrunner, B., M. S. Pritchard, G. J. Kooperman, and J. T. Randerson (2019), Why does Amazon precipitation decrease when tropical forests respond to increasing CO_2?, *Earth's Futur.*, *7*(4), 450–468, doi:10.1029/2018EF001026.

Lawrence, D. M. et al. (2011), Parameterization improvements and functional and structural advances in Version 4 of the Community Land Model, *J. Adv. Model. Earth Syst.*, *3*, 1–27, doi:10.1029/2011MS000045.

Lee, J.-Y., B. Wang, M. C. Wheeler, X. Fu, D. E. Waliser, and I.-S. Kang (2013), Real-time multivariate indices for the boreal summer intraseasonal oscillation over the Asian summer monsoon region, *Clim. Dyn.*, *40*, 493–509, doi:10.1007/s00382-012-1544-4.

Leipprand, A., and D. Gerten (2006), Global effects of doubled atmospheric CO_2 content on evapotranspiration, soil moisture and runoff under potential natural vegetation, *Hydrol. Sci. J.*, *51*(1), 171–185.

Lemordant, L., P. Gentine, A. S. Swann, B. I. Cook, and J. Scheff (2018), Critical impact of

vegetation physiology on the continental hydrologic cycle in response to increasing CO_2, *PNAS*, *115*(16), 4093–4098, doi:10.1073/pnas.1720712115.

Leng, G., M. Huang, Q. Tang, W. J. Sacks, H. Lei, and L. R. Leung (2013), Modeling the effects of irrigation on land surface fluxes and states over the conterminous United States: Sensitivity to input data and model parameters, *J. Geophys. Res. Atmos.*, *11*(17), 9789–9803, doi:10.1002/jgrd.50792.

Leng, G., M. Huang, Q. Tang, H. Gao, and L. R. Leung (2014), Modeling the effects of groundwater-fed irrigation on terrestrial hydrology over the conterminous United States, *J. Hydrometeorol.*, *15*(3), 957–972, doi:10.1175/JHM-D-13-049.1.

Leng, G., M. Huang, Q. Tang, and L. R. Leung (2015), A modeling study of irrigation effects on global surface water and groundwater resources under a changing climate, *J. Adv. Model. Earth Syst.*, *7*(3), 1285–1304, doi:10.1002/2015MS000437.

Levis, S., and W. Sacks (2011), *Technical descriptions of the interactive crop management model (CLM4CNcrop) and interactive irrigation models in version 4 of the Community Land Model.*

Li, R. C. Y., and W. Zhou (2013), Modulation of Western North Pacific tropical cyclone activity by the ISO. Part I: Genesis and intensity, *J. Clim.*, *26*(9), 2904–2918, doi:10.1175/JCLI-D-12-00210.1.

Li, Z., W. Yu, T. Li, V. S. N. Murty, and F. Tangang (2013), Bimodal character of cyclone climatology in the Bay of Bengal modulated by monsoon seasonal cycle, *J. Clim.*, *26*(3), 1033–1046, doi:10.1175/JCLI-D-11-00627.1.

Liebmann, B., H. H. Hendon, and J. D. Glick (1994), The relationship between tropical cyclones of the western Pacific and Indian Oceans and the Madden-Julian oscillation, *J. Meteor. Soc. Japan*, *72*, 401–411.

Lin, H. (2013), Monitoring and Predicting the Intraseasonal Variability of the East Asian–Western, *Mon. Wea. Rev.*, *141*, 1124–1138, doi:10.1175/MWR-D-12-00087.1.

Lindsay, K., G. B. Bonan, S. C. Doney, F. M. Hoffman, D. M. Lawrence, M. C. Long, N. M. Mahowald, J. Keith Moore, J. T. Randerson, and P. E. Thornton (2014), Preindustrial-control and twentieth-century carbon cycle experiments with the earth system model CESM1(BGC), *J. Clim.*, *27*, 8981–9005, doi:10.1175/JCLI-D-12-00565.1.

Lintner, B. R., D. K. Adams, K. A. Schiro, A. M. Stansfield, A. A. Amorim Rocha, and J. D. Neelin (2017), Relationships among climatological vertical moisture structure, column water vapor, and precipitation over the central Amazon in observations and CMIP5 models, *Geophys. Res. Lett.*, *44*(4), 1981–1989, doi:10.1002/2016GL071923.

Lo, M. H., and J. S. Famiglietti (2013), Irrigation in California's Central Valley strengthens

the southwestern U.S. water cycle, *Geophys. Res. Lett.*, *40*(2), 301–306, doi:10.1002/grl.50108.

Lohar, D., and B. Pal (1995), The effect of irrigation on premonsoon season precipitation over South West Bengal, India, *J. Clim.*, *8*, 2567–2570.

Madden, R. A., and P. R. Julian (1971), Detection of a 40–50 day oscillation in the zonal wind in the tropical Pacific, *J. Atmos. Sci.*, *28*(5), 702–708, doi:10.1175/1520-0469(1971)028<0702:DOADOI>2.0.CO;2.

Madden, R. A., and P. R. Julian (1972), Description of global-scale circulation cells in the tropics with a 40–50 day period, *J. Atmos. Sci.*, *29*(6), 1109–1123, doi:10.1175/1520-0469(1972)029<1109:DOGSCC>2.0.CO;2.

Maloney, E. D., D. L. Hartmann, E. D. Maloney, and D. L. Hartmann (2000), Modulation of Eastern North Pacific hurricanes by the Madden–Julian Oscillation, *J. Clim.*, *13*(9), 1451–1460, doi:10.1175/1520-0442(2000)013<1451:MOENPH>2.0.CO;2.

Maloney, E. D., Á. F. Adames, and H. X. Bui (2019), Madden–Julian Oscillation changes under anthropogenic warming, *Nat. Clim. Chang.*, *9*(1), 26–33, doi:10.1038/s41558-018-0331-6.

Martens, B., D. G. Miralles, H. Lievens, R. Van Der Schalie, R. A. M. De Jeu, D. Fernández-Prieto, H. E. Beck, W. A. Dorigo, and N. E. C. Verhoest (2017), GLEAM v3: satellite-based land evaporation and root-zone soil moisture, *Geosci. Model Dev*, *10*, 1903–1925, doi:10.5194/gmd-10-1903-2017.

Mehran, A., A. AghaKouchak, and T. J. Phillips (2014), Evaluation of CMIP5 continental precipitation simulations relative to satellite-based gauge-adjusted observations, *J. Geophys. Res. Atmos.*, *119*(4), 1695–1707, doi:10.1002/2013JD021152.

Meier, J., F. Zabel, and W. Mauser (2018), A global approach to estimate irrigated areas-a comparison between different data and statistics, *Hydrol. Earth Syst. Sci*, *22*, 1119–1133, doi:10.5194/hess-22-1119-2018.

Miralles, D. G., T. R. H. Holmes, R. A. M. De Jeu, J. H. Gash, A. G. C. A. Meesters, and A. J. Dolman (2011), Global land-surface evaporation estimated from satellite-based observations, *Hydrol. Earth Syst. Sci*, *15*, 453–469, doi:10.5194/hess-15-453-2011.

Moon, J.-Y., B. Wang, S.-S. Lee, and K.-J. Ha (2018), An intraseasonal genesis potential index for tropical cyclones during northern hemisphere summer, *J. Clim.*, *31*, 9055–9071, doi:10.1175/JCLI-D-18-0515.1.

Neale, R. B. et al. (2010), *Description of the NCAR Community Atmosphere Model (CAM 4.0)*.

Neale, R. B. et al. (2012), *Description of the NCAR Community Atmosphere Model (CAM 5.0).*

Norby, R. J. et al. (2016), Model-data synthesis for the next generation of forest free-air CO_2 enrichment (FACE) experiments, *New Phytol.*, *209*(1), 17–28, doi:10.1111/nph.13593.

Nowak, R. S. (2017), CO_2 fertilization: Average is best, *Nat. Clim. Chang.*, *7*(2), 101–102, doi:10.1038/nclimate3212.

Obermeier, W. A. et al. (2017), Reduced CO_2 fertilization effect in temperate C3 grasslands under more extreme weather conditions, *Nat. Clim. Chang.*, *7*(2), 137–141, doi:10.1038/nclimate3191.

Oleson, K. W. et al. (2010), *Technical description of version 4.0 of the Community Land Model (CLM)*.

Oouchi, K., A. T. Noda, M. Satoh, H. Miura, H. Tomita, T. Nasuno, and S. Iga (2009), A simulated preconditioning of typhoon genesis controlled by a boreal summer Madden-Julian Oscillation event in a global cloud-system-resolving model, *Sola*, *5*, 65–68, doi:10.2151/sola.2009-017.

Pal, J. S., and E. A. B. Eltahir (2001), Pathways relating soil moisture conditions to future summer rainfall within a model of the land-atmosphere system, *J. Clim.*, *14*(6), 1227–1242, doi:10.1175/1520-0442(2001)014<1227:PRSMCT>2.0.CO;2.

Pappenberger, F., E. Dutra, F. Wetterhall, and H. L. Cloke (2012), Deriving global flood hazard maps of fluvial floods through a physical model cascade, *Hydrol. Earth Syst. Sci.*, *16*(11), 4143–4156, doi:10.5194/hess-16-4143-2012.

Peel, M. C., and T. A. McMahon (2006), Continental runoff: A quality-controlled global runoff data set, *Nature*, *444*, 835–838, doi:10.1038/nature05481.

Pei, L., N. Moore, S. Zhong, A. D. Kendall, Z. Gao, and D. W. Hyndman (2016), Effects of irrigation on summer precipitation over the United States, *J. Clim.*, *29*, 3541–3558, doi:10.1175/JCLI-D-15-0337.1.

Peñuelas, J., J. G. Canadell, and R. Ogaya (2011), Increased water-use efficiency during the 20th century did not translate into enhanced tree growth, *Glob. Ecol. Biogeogr.*, *20*(4), 597–608, doi:10.1111/j.1466-8238.2010.00608.x.

Piao, S., P. Friedlingstein, P. Ciais, N. De Noblet-Ducoudré, D. Labat, and S. Zaehle (2007), Changes in climate and land use have a larger direct impact than rising CO_2 on global river runoff trends, *PNAS*, *104*(39), 15242–15247, doi:10.1080/00365590600620792.

Pielke, R. A., J. Adegoke, A. Beltrán-Przekurat, C. A. Hiemstra, J. Lin, U. S. Nair, D. Niyogi, and T. E. Nobis (2007), An overview of regional land-use and land-cover impacts on rainfall, *Tellus, Ser. B Chem. Phys. Meteorol.*, *59*(3), 587–601, doi:10.1111/j.1600-0889.2007.00251.x.

Puma, M. J., and B. I. Cook (2010), Effects of irrigation on global climate during the 20th century, *J. Geophys. Res. Atmos.*, *115*(16), 1–15, doi:10.1029/2010JD014122.

Ramsay, H. (2017), The global climatology of tropical cyclones, *Oxford Res. Encycl. Nat. Hazard Sci.*, 1–34, doi:10.1093/acrefore/9780199389407.013.79.

Reich, P. B., S. E. Hobbie, and T. D. Lee (2014), Plant growth enhancement by elevated CO_2 eliminated by joint water and nitrogen limitation, *Nat. Geosci.*, *7*(12), 920–924, doi:10.1038/ngeo2284.

Reich, P. B., S. E. Hobbie, T. D. Lee, and M. A. Pastore (2018), Unexpected reversal of C3 versus C4 grass response to elevated CO_2 during a 20-year field experiment, *Science*, *360*(6386), 317–320, doi:10.1126/SCIENCE.AAS9313.

Richardson, T. B. et al. (2018), Carbon dioxide physiological forcing dominates projected Eastern Amazonian drying, *Geophys. Res. Lett.*, *45*, doi:10.1002/2017GL076520.

Roser, M., H. Ritchie, and E. Ortiz-Ospina (2019), World population growth, *Publ. online OurWorldInData.org*. Available from: https://ourworldindata.org/world-population-growth

Sacks, W. J., B. I. Cook, N. Buenning, S. Levis, and J. H. Helkowski (2009), Effects of global irrigation on the near-surface climate, *Clim. Dyn.*, *33*(2–3), 159–175, doi:10.1007/s00382-008-0445-z.

Saeed, F., S. Hagemann, and D. Jacob (2009), Impact of irrigation on the South Asian summer monsoon, *Geophys. Res. Lett.*, *36*(20), doi:10.1029/2009GL040625.

Sakaguchi, K., L. R. Leung, C. D. Burleyson, H. Xiao, and H. Wan (2018), Role of troposphere-convection-land coupling in the Southwestern Amazon precipitation bias of the Community Earth System Model Version 1 (CESM1), *J. Geophys. Res. Atmos.*, *123*(16), 8374–8399, doi:10.1029/2018JD028999.

Satoh, M. et al. (2012), The Intra-Seasonal Oscillation and its control of tropical cyclones simulated by high-resolution global atmospheric models, *Clim. Dyn.*, *39*(9–10), 2185–2206, doi:10.1007/s00382-011-1235-6.

Segal, M., Z. Pan, R. W. Turner, and E. S. Takle (1998), On the potential impact of irrigated areas in North America on summer rainfall caused by large-scale systems, *J. Appl. Meteorol.*, *37*, 325–331, doi:10.1175/1520-0450-37.3.325.

Selman, C., and V. Misra (2016), The sensitivity of southeastern United States climate to varying irrigation vigor, *J. Geophys. Res. Atmos.*, *121*, doi:10.1002/2016JD025002.

Seneviratne, S. I. et al. (2012), Changes in climate extremes and their impacts on the natural physical environment, in *Managing the Risks of Extreme Events and Disasters to*

Advance Climate Change Adaptation, edited by C. B. Field et al., pp. 109–230, Cambridge University Press, Cambridge, UK, and New York, NY, USA.

Shkolnik, I., T. Pavlova, S. Efimov, and S. Zhuravlev (2018), Future changes in peak river flows across northern Eurasia as inferred from an ensemble of regional climate projections under the IPCC RCP8.5 scenario, *Clim. Dyn.*, *50*, 215–230, doi:10.1007/s00382-017-3600-6.

Siebert, S., J. Burke, J. M. Faures, K. Frenken, J. Hoogeveen, P. D??ll, and F. T. Portmann (2010), Groundwater use for irrigation - A global inventory, *Hydrol. Earth Syst. Sci.*, *14*(10), 1863–1880, doi:10.5194/hess-14-1863-2010.

Skinner, C. B., C. J. Poulsen, R. Chadwick, N. S. Diffenbaugh, and R. P. Fiorella (2017), The role of plant CO_2 physiological forcing in shaping future daily-scale precipitation, *J. Clim.*, *30*(7), 2319–2340, doi:10.1175/JCLI-D-16-0603.1.

van der Sleen, P., P. Groenendijk, M. Vlam, N. P. R. Anten, A. Boom, F. Bongers, T. L. Pons, G. Terburg, and P. A. Zuidema (2015), No growth stimulation of tropical trees by 150 years of CO_2 fertilization but water-use efficiency increased, *Nat. Geosci.*, *8*(1), 24–28, doi:10.1038/ngeo2313.

Smith, R. et al. (2010), *The Parallel Ocean Program (POP) Reference Manual (Tech. Rep. LAUR-10-01853)*.

Sobel, A. H., C.-Y. Lee, S. J. Camargo, K. T. Mandli, K. A. Emanuel, P. Mukhopadhyay, and M. Mahakur (2019), Tropical Cyclone Hazard to Mumbai in the Recent Historical Climate, *Mon. Wea. Rev.*, *147*, 2355–2366, doi:10.1175/MWR-D-18.

Sorooshian, S., J. Li, K. L. Hsu, and X. Gao (2011), How significant is the impact of irrigation on the local hydroclimate in Californias Central Valley? Comparison of model results with ground and remote-sensing data, *J. Geophys. Res. Atmos.*, *116*(6), 1–11, doi:10.1029/2010JD014775.

Sorooshian, S., A. Aghakouchak, and J. Li (2014), Influence of irrigation on land hydrological processes over California, *J. Geophys. Res. Atmos.*, *119*, 1–16, doi:10.1002/2014JD022232.

Stephens, G. L., T. L'Ecuyer, R. Forbes, A. Gettlemen, J. C. Golaz, A. Bodas-Salcedo, K. Suzuki, P. Gabriel, and J. Haynes (2010), Dreary state of precipitation in global models, *J. Geophys. Res. Atmos.*, *115*(24), 1–13, doi:10.1029/2010JD014532.

Sun, Y., S. Solomon, A. Dai, and R. W. Portmann (2007), How often will it rain?, *J. Clim.*, *20*(19), 4801–4818, doi:10.1175/JCLI4263.1.

Swann, A. L. S., F. M. Hoffman, C. D. Koven, and J. T. Randerson (2016), Plant responses to increasing CO_2 reduce estimates of climate impacts on drought severity, *PNAS*,

113(36), 10019–10024, doi:10.1073/pnas.1604581113.

Thiery, W., E. L. Davin, D. M. Lawrence, A. L. Hirsch, M. Hauser, and S. I. Seneviratne (2017), Present-day irrigation mitigates heat extremes, *J. Geophys. Res. Atmos.*, *122*, 1403-1422, doi:10.1002/2016JD025740.

Tippett, M. K., S. J. Camargo, and A. H. Sobel (2011), A poisson regression index for tropical cyclone genesis and the role of large-scale vorticity in genesis, *J. Clim.*, *24*, 2335–2357, doi:10.1175/2010JCLI3811.1.

Trenberth, K. (2011), Changes in precipitation with climate change, *Clim. Res.*, *47*(1), 123–138, doi:10.3354/cr00953.

Tuinenburg, O. A., R. W. A. Hutjes, T. Stacke, A. Wiltshire, and P. Lucas-Picher (2014), Effects of irrigation in India on the atmospheric water budget, *J. Hydrometeorol.*, *15*, 1028–1050, doi:10.1175/JHM-D-13-078.1.

UNISDR (2015), *Making development sustainable: The future of disaster risk management. Global assessment report on disaster risk reduction*, Geneva, Switzerland.

de Vrese, P., S. Hagemann, and M. Claussen (2016), Asian irrigation, African rain: Remote impacts of irrigation, *Geophys. Res. Lett.*, *43*(8), 3737–3745, doi:10.1002/2016GL068146.

de Vries, D. A. (1959), The influence of irrigation on the energy balance and the climate near the ground, *J. Meteorol.*, *16*, 256–270, doi:http://dx.doi.org/10.1175/1520-0469(1959)016<0256:TIOIOT>2.0.CO;2.

Wang, B., and J.-Y. Moon (2017), An anomalous genesis potential index for MJO modulation of tropical cyclone, *J. Clim.*, *30*(11), 4021–4035, doi:10.1175/JCLI-D-16-0749.1.

Wheeler, M. C., and H. H. Hendon (2004), An all-season real-time multivariate MJO index: Development of an index for monitoring and prediction, *Mon. Weather Rev.*, *132*(8), 1917–1932, doi:10.1175/1520-0493(2004)132<1917:AARMMI>2.0.CO;2.

Wigley, T. M. L., and P. D. Jones (1985), Influences of precipitation changes and direct CO_2 effects on streamflow, *Nature*, *314*, 149–152.

Woldemeskel, F., and A. Sharma (2016), Should flood regimes change in a warming climate? The role of antecedent moisture conditions, *Geophys. Res. Lett.*, *43*, 7556-7563, doi:10.1002/2016GL069448.

Wolding, B. O., E. D. Maloney, S. Henderson, and M. Branson (2017), Climate change and the Madden-Julian Oscillation: A vertically resolved weak temperature gradient analysis, *J. Adv. Model. Earth Syst.*, *9*,307-331, doi:10.1002/2016MS000843.

Wu, L., and M. Takahashi (2018), Contributions of tropical waves to tropical cyclone genesis over the western North Pacific, *Clim. Dyn.*, *50*(11–12), 4635–4649, doi:10.1007/s00382-017-3895-3.

Yamazaki, D., S. Kanae, H. Kim, and T. Oki (2011), A physically based description of floodplain inundation dynamics in a global river routing model, *Water Resour. Res.*, *47*(4), 1–21, doi:10.1029/2010WR009726.

Yin, L., R. Fu, E. Shevliakova, and R. E. Dickinson (2013), How well can CMIP5 simulate precipitation and its controlling processes over tropical South America?, *Clim. Dyn.*, *41*(11–12), 3127–3143, doi:10.1007/s00382-012-1582-y.

Yokoi, S., Y. N. Takayabu, and J. C. L. Chan (2009), Tropical cyclone genesis frequency over the western North Pacific simulated in medium-resolution coupled general circulation models, *Clim. Dyn.*, *33*, 665–683, doi:10.1007/s00382-009-0593-9.

You, L., J. Gao, H. Lin, and S. Chen (2018), Impact of the intra-seasonal oscillation on tropical cyclone genesis over the western North Pacific, *Int. J. Climatol.*, *39*, 1969-1984, doi:10.1002/joc.5927.

Zhang, C. (2005), Madden-Julian Oscillation, *Rev. Geophys.*, *43*(2), RG2003, doi:10.1029/2004RG000158.

Zhang, X., H. Wan, F. W. Zwiers, G. C. Hegerl, and S.-K. Min (2013), Attributing intensification of precipitation extremes to human influence, *Geophys. Res. Lett.*, *40*(19), 5252–5257, doi:10.1002/grl.51010.

Zhao, C., and T. Li (2018), Basin dependence of the MJO modulating tropical cyclone genesis, *Clim. Dyn.*, *52*, 6081–6096, doi:10.1007/s00382-018-4502-y.

Zhao, H., R. Yoshida, and G. B. Raga (2015a), Impact of the Madden–Julian Oscillation on Western North Pacific tropical cyclogenesis associated with large-scale patterns, *J. Appl. Meteorol. Climatol.*, *54*(7), 1413–1429, doi:10.1175/JAMC-D-14-0254.1.

Zhao, H., X. Jiang, and L. Wu (2015b), Modulation of Northwest Pacific Tropical Cyclone Genesis by the Intraseasonal Variability, *J. Meteorol. Soc. Japan*, *93*(1), 81–97, doi:10.2151/jmsj.2015-006.

Appendix A

Supplementary Information for Chapter 2

Adapted from:

Fowler, M.D., M.S. Pritchard, and G.J. Kooperman, 2018: Assessing the Impact of Indian Irrigation on Precipitation in the Irrigation-Enabled Community Earth System Model. *J. Hydrometeor.,* **19**, 427–443, https://doi.org/10.1175/JHM-D-17-0038.1.

© American Meteorological Society. Used with permission.

A.1: Double Irrigated Area Experiment

To assess the robustness of observed atmospheric responses to irrigation in India and to hedge against an intrinsic low bias in ET response to irrigation revealed in the IRRIG experiment (see Section 2.3.1), we generated a 60-member irrigation ensemble in which we double the amount of irrigated area per grid cell (IRRIG2X). Doubling was achieved by reducing the grid-cell-percentage of other plant functional types (PFTs) so as to maintain the ratio between them. An exception to this approach occurs when a doubling of irrigated area would fill the entire vegetated fraction of the grid cell; in those situations, the percentages of all other PFTs were set to zero and irrigated crops were allowed to fill all available vegetation space. This approach of doubling irrigated area was used as a way to simulate increased irrigation vigor, as manually increasing the irrigation rate itself (e.g., by tuning the F_{IRRIG} parameter) leads to enhanced surface runoff rather than increased soil moisture and evapotranspiration. In this fashion, despite the limitations of CLM4's surface water partitioning, the pair of experiments (IRRIG, IRRIG2X) can be viewed as bracketing a realistic magnitude of local ET irrigation response, and hence a realistic range of non-local impacts.

A.2: Climatological Simulations of Irrigation in California's Central Valley

An additional set of simulations was carried out to test the geographic resilience of our findings about irrigation infiltration efficiency, focusing on California's Central Valley. As in the case of the India experiments, irrigation was only enabled over the region of interest (in

this case, the Central Valley). Unlike India, we used long free-running simulations of duration. We evaluate three experiments designed to determine the atmospheric sensitivity to varying rates of irrigation, as well as a control simulation in which irrigation is not enabled. In IRRIG100, no modifications were made to the default behavior of the irrigation scheme apart from the geographic limitation discussed above. In two sensitivity experiments, IRRIG75 and IRRIG50, the model applies 75% and 50% of the water needed to meet the target soil moisture determined by *Eq. 1*. Each of the four simulations were run for 35-years, with the first five years discarded as spin-up. Averages over the Central Valley were only taken over grid cells with at least 10% irrigated area to avoid the inclusion of grid cells that are not traditionally considered part of the agricultural region.

Overall *Figures A.1* and *A.2* confirm that irrigation water is too tightly coupled to surface runoff and only weakly coupled to ET.

A.3: Supporting Figures

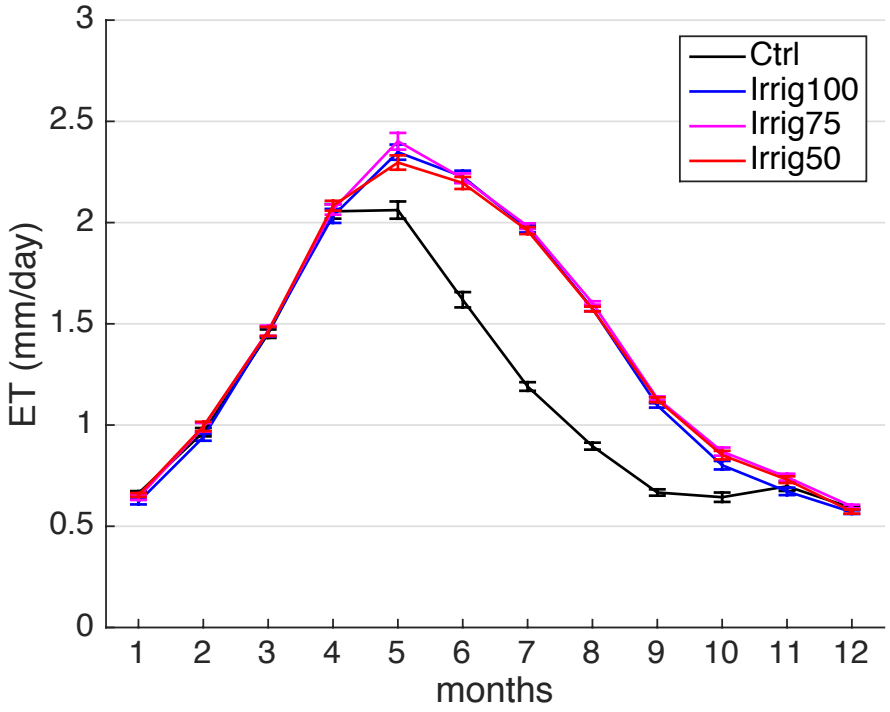

Figure A.1: *Annual cycle of evapotranspiration (ET) in California's Central Valley (defined as all grid cells with at least 10% irrigated area). Error bars represent the standard error of 30-year monthly averages. For comparison, see annual ET cycle in Figure 3c in Anderson et al. [2015], which shows an ET peak in late summer rather than late spring.*

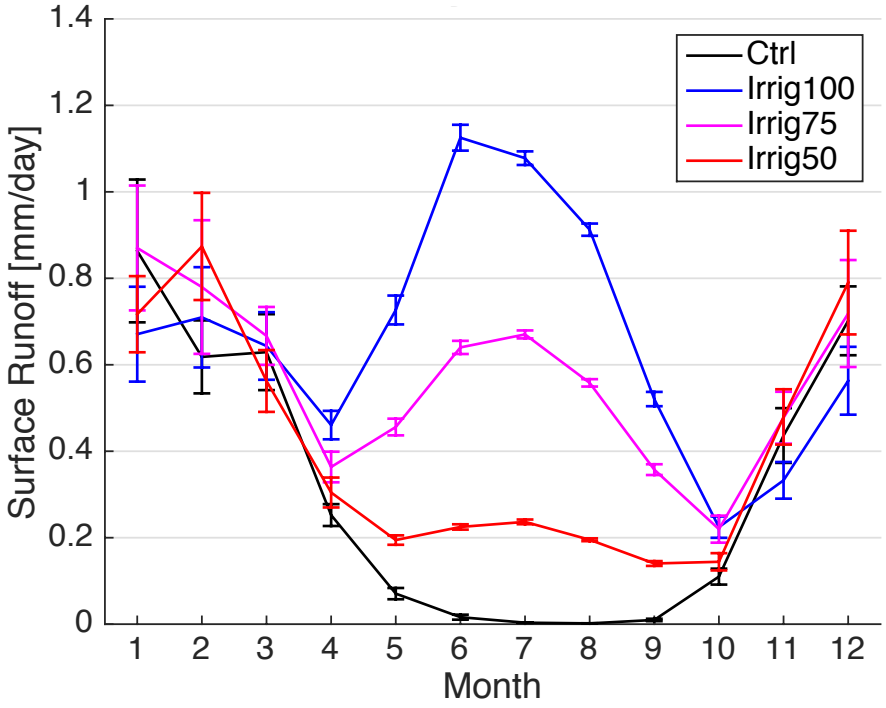

Figure A.2: *Annual cycle of surface runoff in California's Central Valley (defined as all grid cells with at least 10% irrigated area). Error bars represent the standard error of 30-year monthly averages. For comparison, Sorooshian et al. [2014] suggests that runoff during the summer months is less than 1 mm month^{-1}, while the IRRIG100 experiment experiences more than 1 mm day^{-1}.*

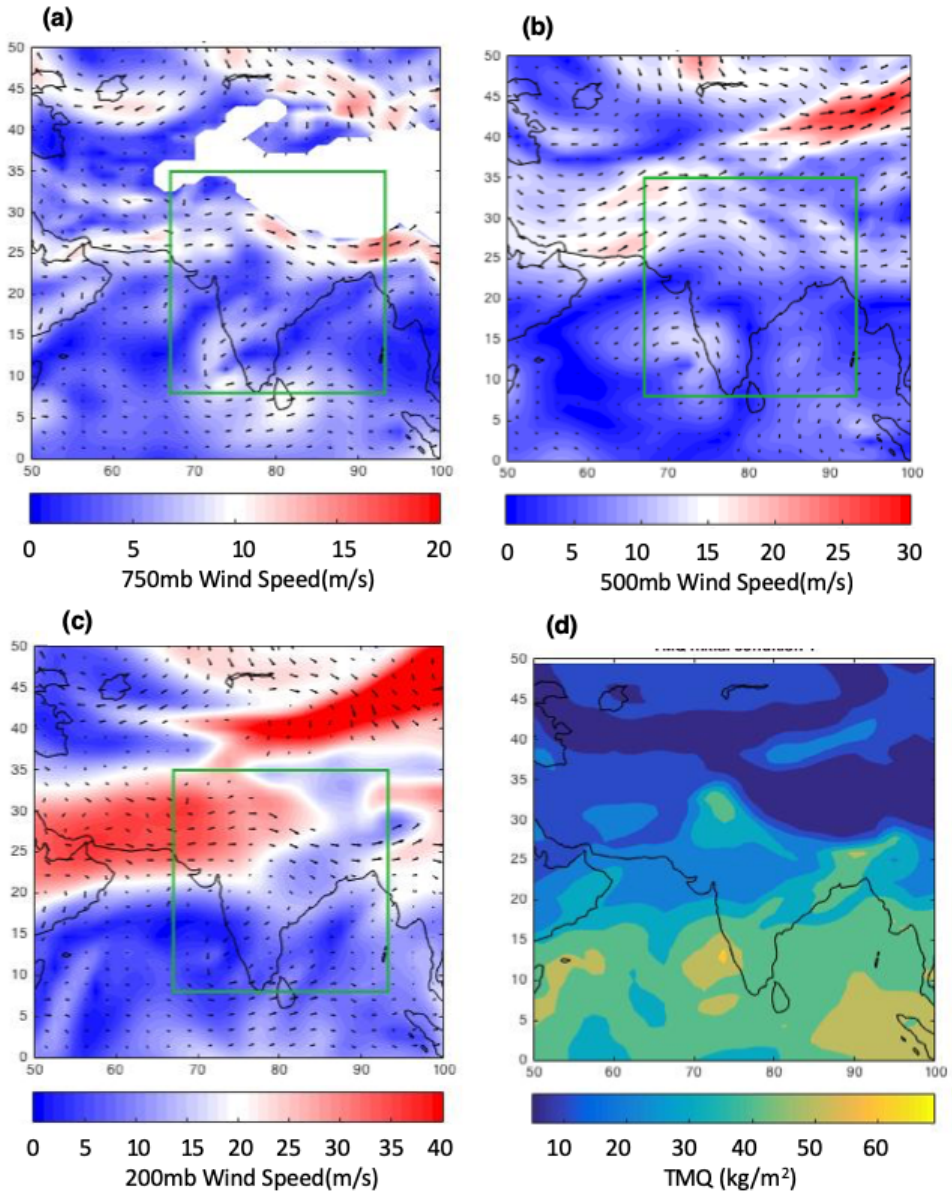

Figure A.3: *For the May 10th ensembles, initial (a) 750 hPa, (b) 500 hPa, and (c) 200 hPa wind field, with speed denoted by shading and direction by vectors. (d) Initial vertically integrated precipitable water field.*

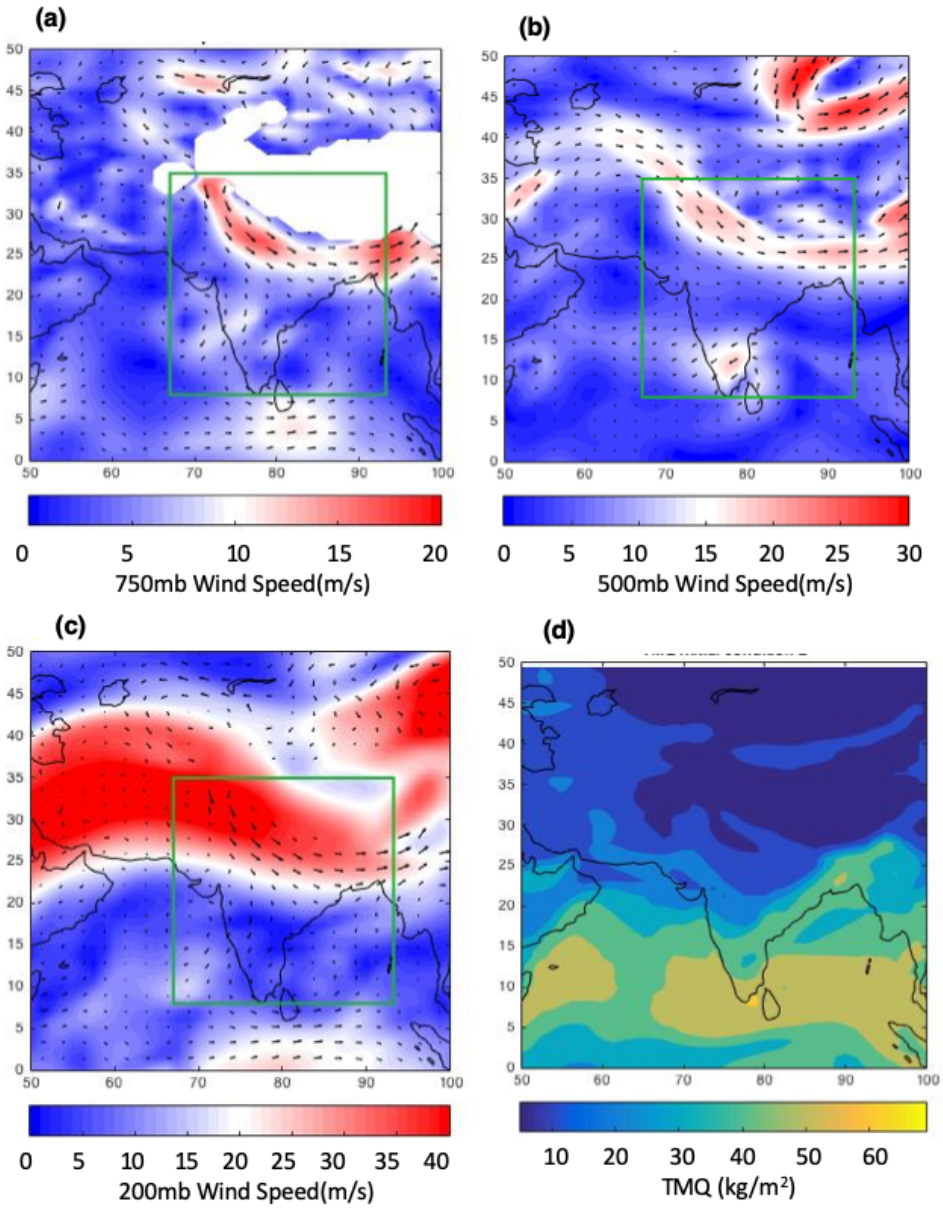

Figure A.4: *As in Figure A.3, but for the May 15th ensembles.*

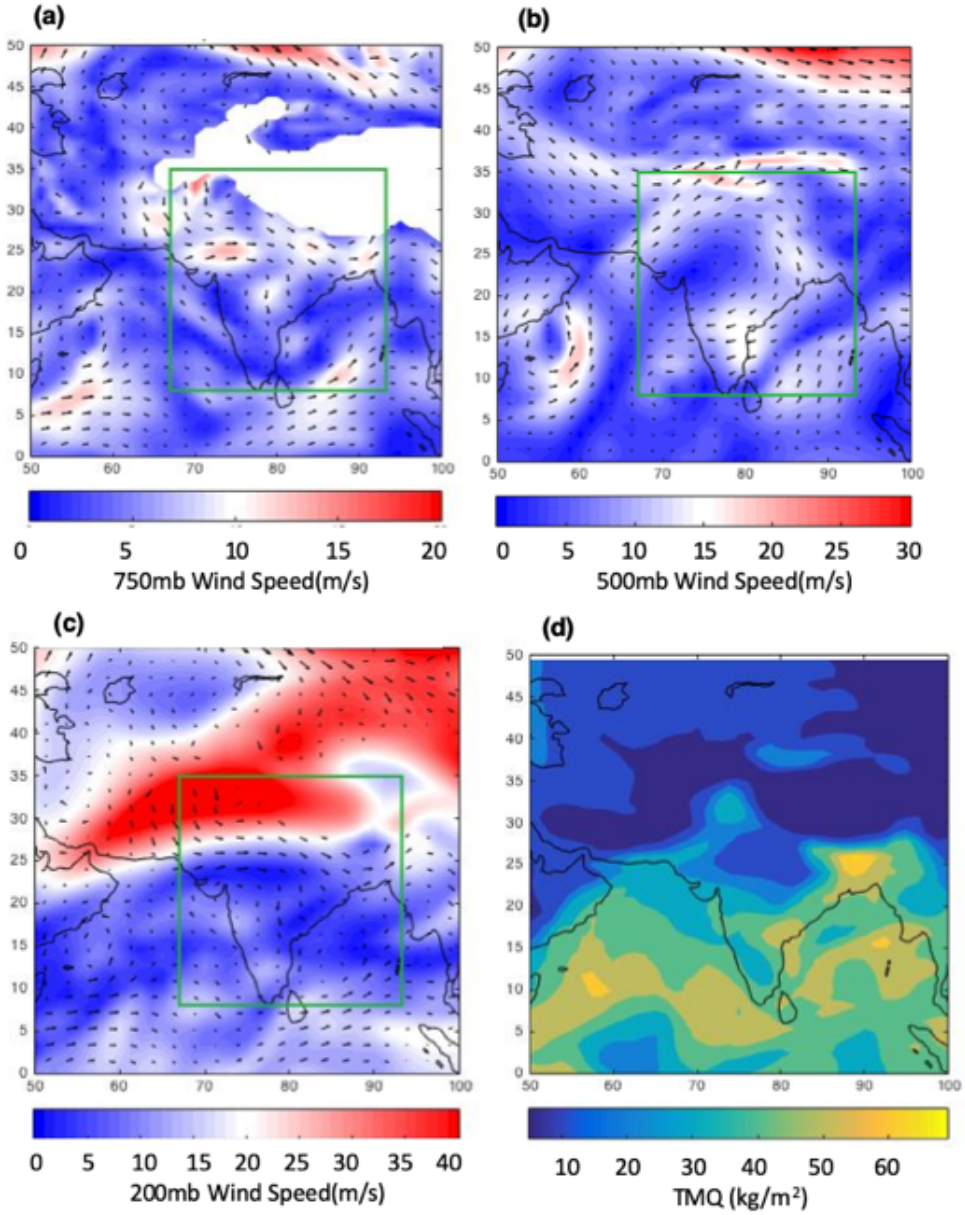

Figure A.5: *As in Figure A.3, but for the May 20th ensembles.*

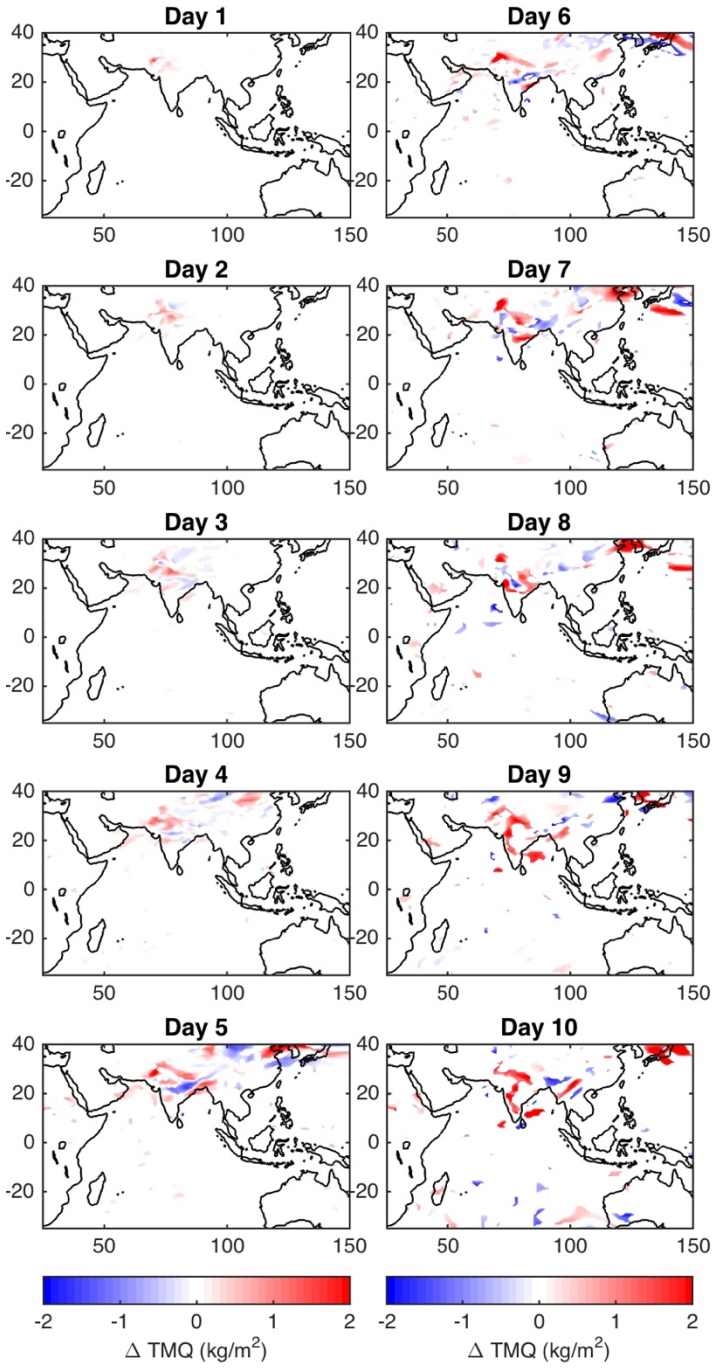

Figure A.6: *Time evolution of vertically integrated atmospheric water vapor (TMQ) in the May 10th IRRIG ensemble. Each panel shows the daily average difference in TMQ, averaged over 20 ensembles with the original amount of irrigated area. Shading is only applied to regions with statistically significant changes in TMQ.*

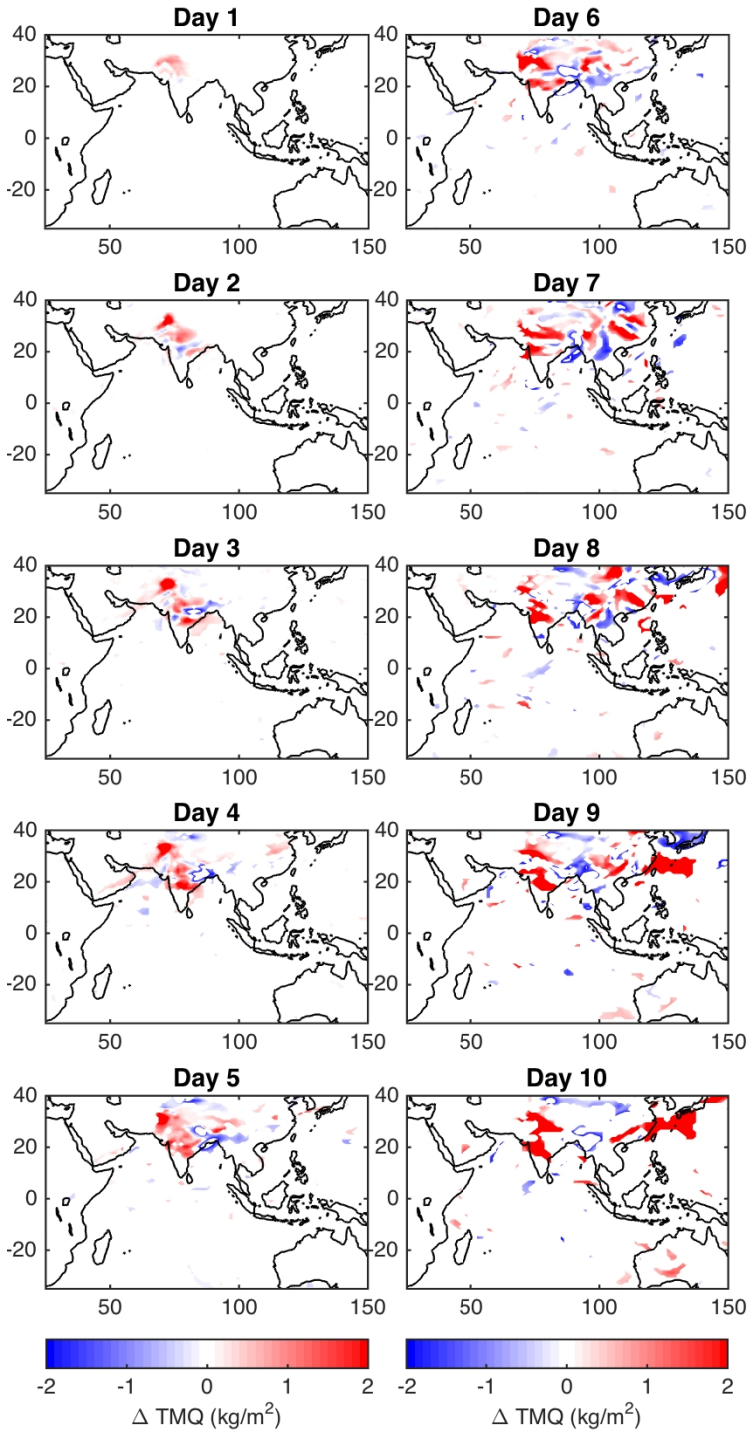

Figure A.7: *As in Figure A.6, but for the May 15th IRRIG ensemble.*

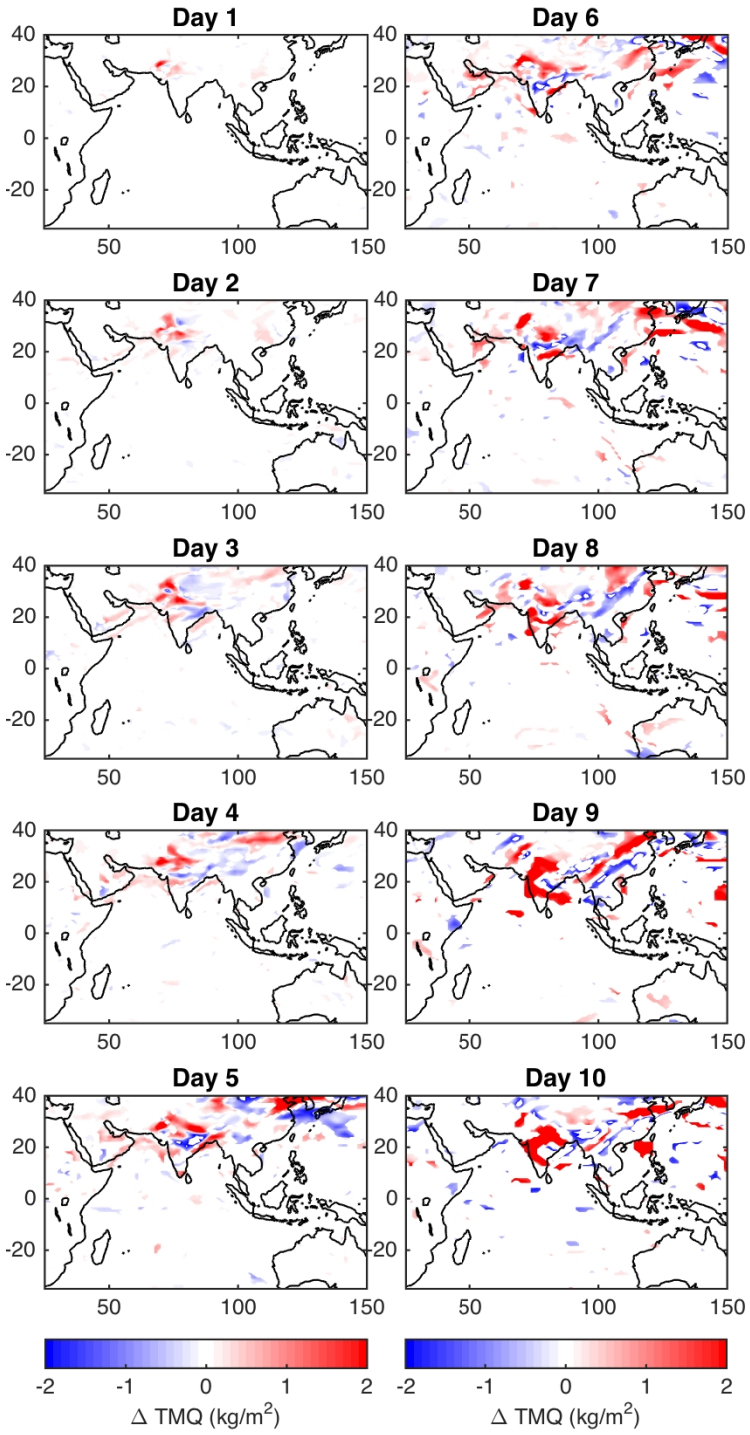

Figure A.8: *Time evolution of vertically integrated atmospheric water vapor (TMQ) in the May 10th IRRIG2x ensemble. Each panel shows the daily average difference in TMQ. Shading is only applied to regions with statistically significant changes in TMQ.*

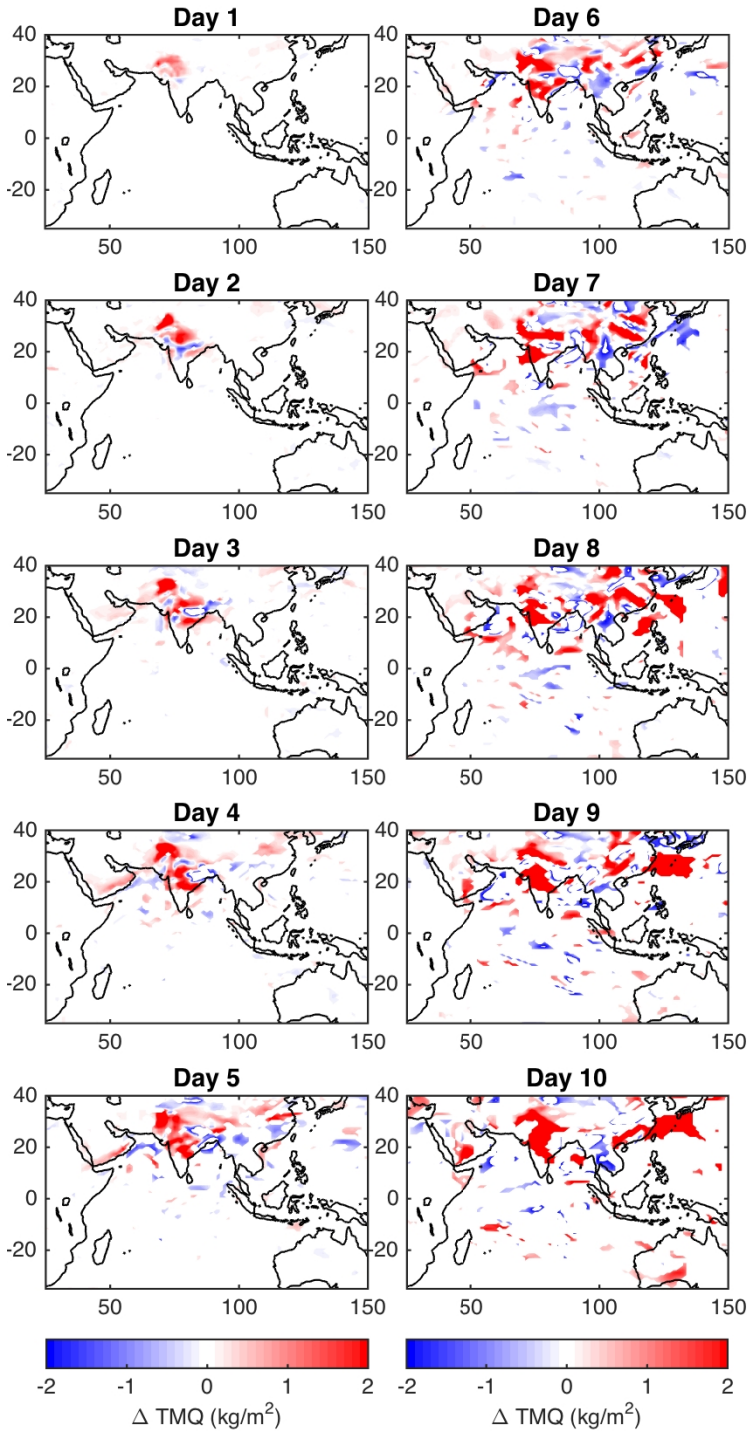

Figure A.9: *As in Figure A.8, but for the May 15th IRRIG2x ensemble.*

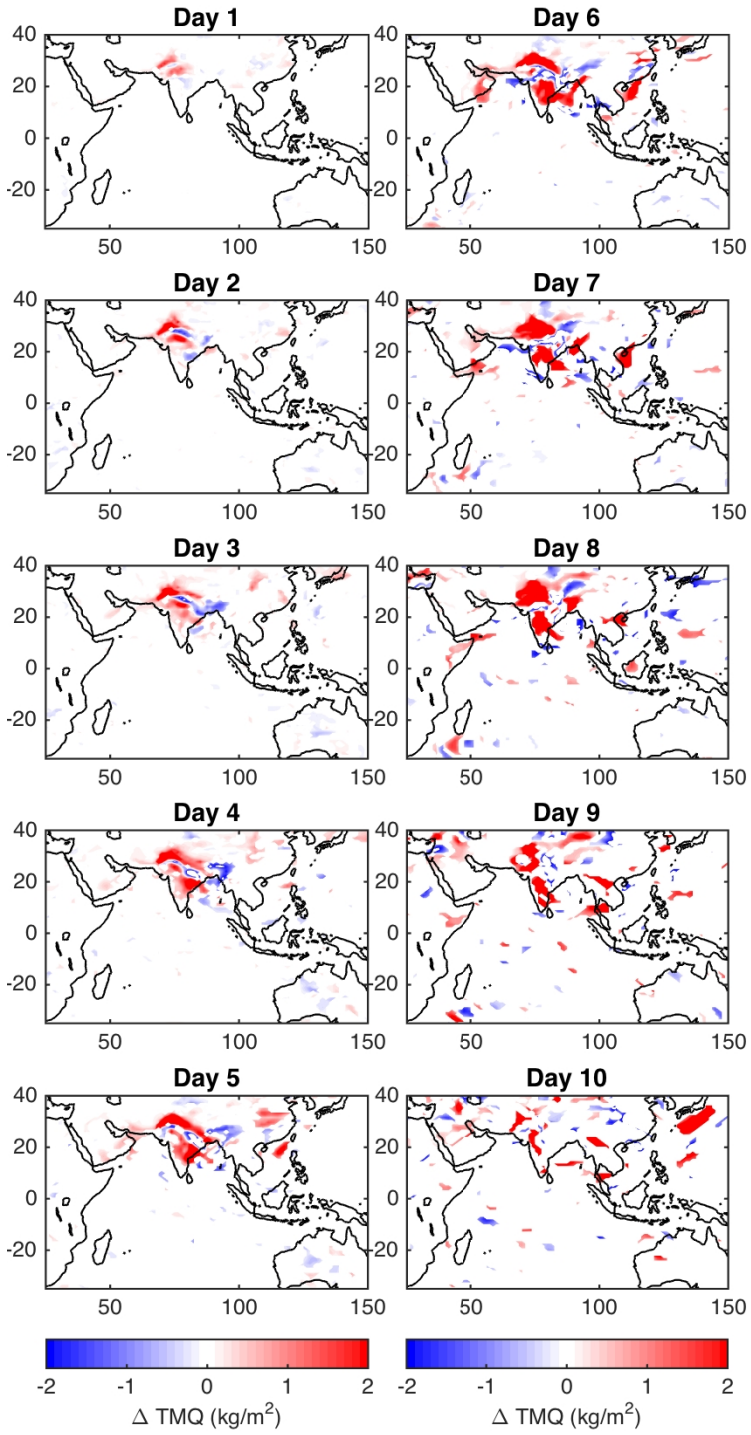

***Figure A.10**: As in Figure A.8, but for the May 20th IRRIG2x ensemble.*

Appendix B

Supplementary Information for Chapter 3

Adapted from:

Fowler, M.D., G.J. Kooperman, J.T. Randerson, and M.S. Pritchard, 2019: Identifying the effect of plant-physiological responses to rising CO_2 on global streamflow. Under review at *Nature Climate Change*.

B.1 Evapotranspiration and vegetation response

Changes in the three components of evapotranspiration (ET) and leaf area index (LAI) are presented in *Figure B.2*. As expected, the largest ET change in the *PHYS* simulations occur through decreased transpiration as a result of reduced stomatal openings in response to higher CO_2 concentrations [*Ainsworth and Long*, 2004; *De Kauwe et al.*, 2013]. *RAD*-driven changes in transpiration are also large, increasing throughout much of the world as rising temperatures increase atmospheric moisture demand; rising ground evaporation rates are present in this experiment as well, leading to overall large increases in ET at northern latitudes in *FULL (Fig. B.8*). Tropical reductions in *FULL* ET are instead primarily driven by *PHYS* transpiration changes, despite increased LAI in that simulation which would typically resist such a reduction.

These patterns agree well with the findings of past studies that have assessed the ability of *PHYS* and *RAD* to alter ET and LAI. *Skinner et al.* [2017] note the strong effect of physiological forcings in the tropics, which lead to decreased ET via transpiration reductions and ultimately alter local precipitation patterns in heavily forested regions. These changes are also in line with the multi-model response of ET presented in *Figure B.2* of *Swann et al.* [2016]– *FULL* decreases in ET over parts of the tropics are primarily a result of *PHYS*, while northern latitude increases are *RAD*-driven instead. Those changes occur despite increases in LAI in both *PHYS* and *FULL* for each of the 7 models assessed. The agreement between past studies and the changes simulated here lends confidence to the validity of the hydrological forcing that will be assessed in the main text.

B.2 Environmental drivers of flood increases

We assess changes in key flood-related variables to identify the primary cause of increased flood frequency for each domain outlined in *Figure 3.1e*, focusing just on time-mean state variables during peak flood season. Since flood seasonality is regionally variable, we first define regional calendar month boundaries that straddle the 30-year composite seasonal cycle's annual interval of maximum discharge. For multiply stressed regions, the period of interest in the Southeast US is defined as Mar-Aug (inclusive), Jun-Oct in Southeast Asia, and Dec-Apr in Central Australia. In the *PHYS*-driven regions, this is defined as Dec-Jun in the Western Amazon, May-Nov in Central Africa, and Nov-May in Southeast Australia. Lastly, for the two *RAD*-driven regions, we consider the period of Aug-Dec for the Horn of Africa, and Jun-Oct in the India/Middle East region.

Overall, for multiply stressed regions (*Table B.1*) the results of this process confirm our initial hypothesis that reduced stomatal conductance in *PHYS* leads to increased flooding by enhancing antecedent soil moisture conditions. When only the land surface is able to respond to higher CO_2 concentrations in *PHYS* (left column), precipitation changes are small and not significant in any region. Soil moisture, however, increases significantly in all regions, as expected when the water use efficiency of plants rises. Tellingly, this occurs despite a lack of detectable change in shortwave radiation and resistive increases in productivity (represented here by gross primary productivity, GPP), which responds to elevated CO_2 in ways that would tend to dry the soil rather than moisten it. In contrast, when only the atmosphere is allowed to respond to enhanced CO_2 (*RAD*; middle column of *Table B.1*), precipitation increases in all three multiply stressed regions while other

potentially important factors like snowmelt cannot explain the flood increase (i.e. statistically insignificant decreases in all regions). This increase of precipitation in the absence of other explanatory factors is also the case for regions that are driven almost exclusively by the *RAD* response, summarized in *Table B.2*. In regions that are primarily *PHYS*-driven in the *FULL* experiment, increased soil moisture is again found to be important, as was the case in multiply-stressed regions; however, in this case increases in precipitation over Western Amazon and Central Africa also contribute (*Table B.3; right column*) by rearranging precipitation patterns non-locally to these domains.

B.3 Supporting Figures and Tables

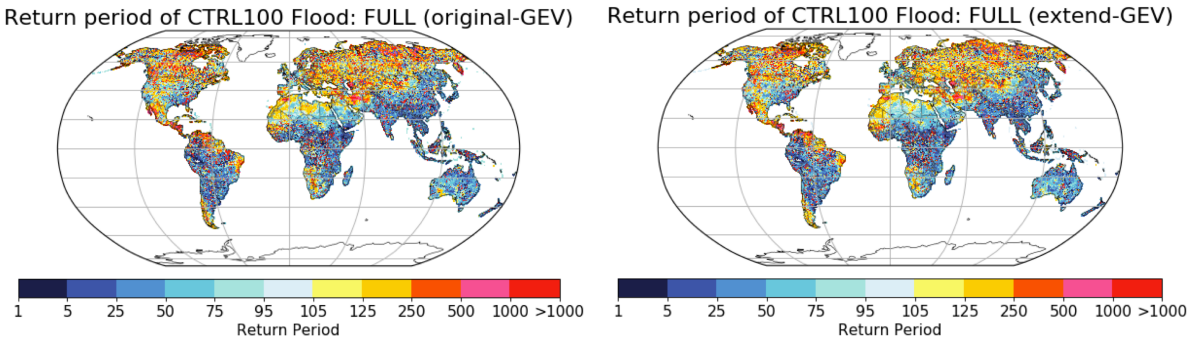

Figure B.1: *Comparison of the FULL flood return period created from (left) the original 30-year period used for analysis and (right) the full 50-year sample wherein CO_2 is still held steady at four times its pre-industrial amount.*

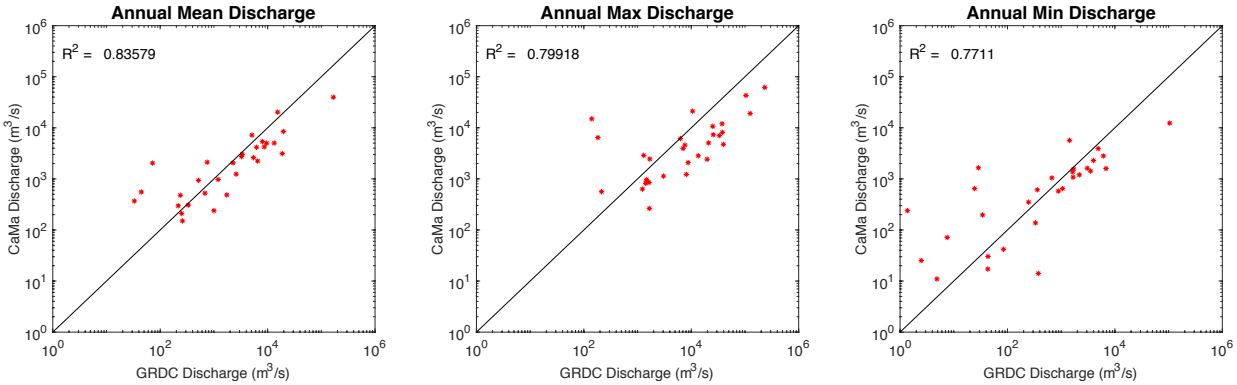

Figure B.2: *Validation of CaMa-simulated time-mean and annual extremum statistics as downscaled from CESM runoff in CTRL against observed GRDC streamflow across a selection of large river basins.*

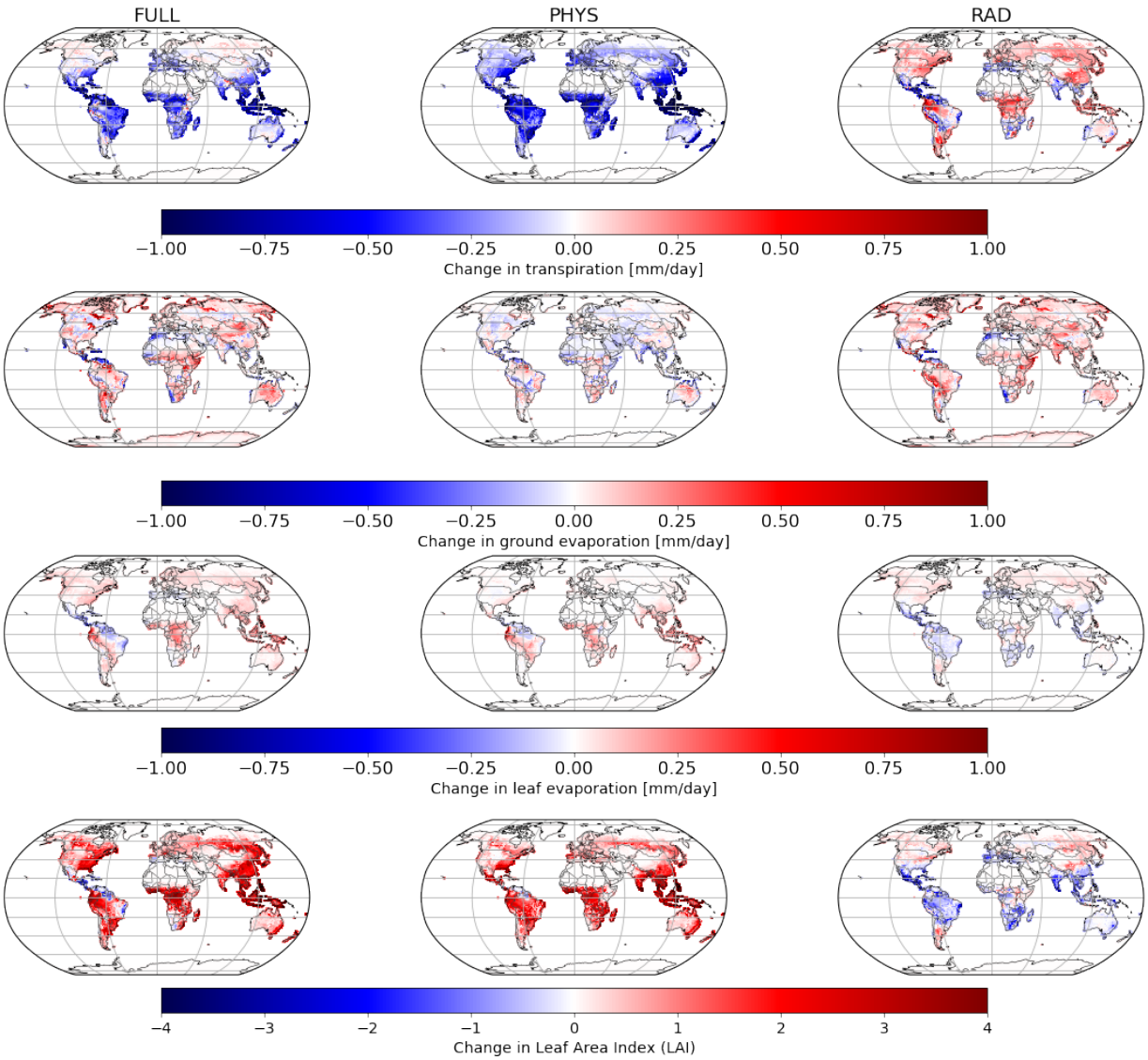

Figure B.3: *Changes (relative to* CTRL*) in transpiration, ground evaporation, leaf evaporation, and leaf area index.*

Multiply-stressed Regions									
	PHYS – CTRL			***RAD – CTRL***			***FULL – CTRL***		
	SE U.S.	**SE Asia**	**C. Aus**	**SE U.S.**	**SE Asia**	**C. Aus**	**SE U.S.**	**SE Asia**	**C. Aus**
Rain	-2.59	7.53	10.88	18.76	25.30	21.60	10.68	26.38	22.43
1m Soil Moisture	9.34	5.03	6.00	4.07	2.07	2.03	9.09	4.81	5.91
GPP	51.79	26.38	33.85	4.97	4.28	10.74	69.71	40.45	50.96
Surface Shortwave Radiation	2.18	1.17	-0.04	-2.78	-2.90	-1.04	-0.28	-1.29	-0.82
Snowmelt	73.32	-83.91	0.20	-90.70	-75.44	-16.09	-90.70	-75.44	-16.09
Runoff	104.89	78.42	65.74	92.85	82.32	68.89	132.68	110.49	109.89
ET	-13.80	-15.09	0.58	8.15	5.43	12.11	-4.23	-4.90	8.97
$CTRL_{100}$ Return Period	21.33	22.88	28.78	23.41	21.40	21.45	17.66	17.22	20.14

Table B.1: *(Top rows) Percent change in horizontally averaged climatological values of flood relevant state variables within the multiply stressed regions from Fig. 1 during their peak flood season (see text); (Bottom) return period of the $CTRL_{100}$ flood for the same regions. Values in black indicate significance at the 95% level (grey values are not significant). Flood season is Mar-Aug for the SE U.S., Jun-Oct for SE Asia, and Dec.-Apr for Central Australia.*

***RAD*-driven Regions**						
	PHYS – CTRL		***RAD – CTRL***		***FULL – CTRL***	
	India	**Horn of Africa**	**India**	**Horn of Africa**	**India**	**Hon of Africa**
Rain	1.29	-5.85	18.64	25.56	20.18	23.57
1m Soil Moisture	1.18	0.11	1.72	5.91	2.34	7.86
GPP	29.81	19.76	-2.92	11.73	43.18	41.96
Surface Shortwave radiation	1.00	4.13	-1.51	-4.78	-1.54	-2.13
Snowmelt	-29.25	3.78	-81.54	-7.58	-81.54	-7.58
Runoff	19.42	29.33	31.95	43.87	52.10	76.16
ET	-11.26	-11.49	3.89	15.85	-5.03	7.73
$CTRL_{100}$ Return Period	249.87	337.48	24.42	15.53	23.20	16.87

Table B.2: *As in Table B.1, but for RAD-driven regions. Flood season is defined as Jun-Oct for India and Aug-Dec for the Horn of Africa.*

***PHYS*-driven Regions**									
	PHYS – CTRL			***RAD – CTRL***			***FULL – CTRL***		
	W Amazon	**C. Africa**	**SE Aus.**	**W Amazon**	**C. Africa**	**SE Aus.**	**W Amazon**	**C. Africa**	**SE Aus.**
Rain	12.28	12.70	5.32	-1.15	-1.27	11.91	16.45	21.08	12.16
1m Soil Moisture	10.06	9.43	12.25	-4.60	-4.84	-2.90	7.13	9.41	6.22
GPP	27.54	19.21	56.34	-2.79	9.56	2.54	49.10	34.10	63.79
Surface Shortwave radiation	3.20	1.05	0.89	3.79	-2.74	-0.14	5.38	-3.19	1.39
Snowmelt	11.76	10.53	-6.32	11.02	-49.55	-26.86	11.02	-49.55	-26.86
Runoff	81.29	130.41	152.76	-24.80	-31.40	-14.94	50.03	131.26	74.59
ET	-9.13	-16.65	-2.96	8.21	7.12	8.81	2.81	-8.23	6.21
$CTRL_{100}$ Return Period	6.97	16.16	15.83	342.26	348.13	303.39	8.15	11.62	20.71

Table B.3: *As in Table B.1, but for PHYS-driven regions. Flood season is defined as Dec-Jun for W Amazon, May-Nov for Central Africa, and Nov-May for SE Australia.*

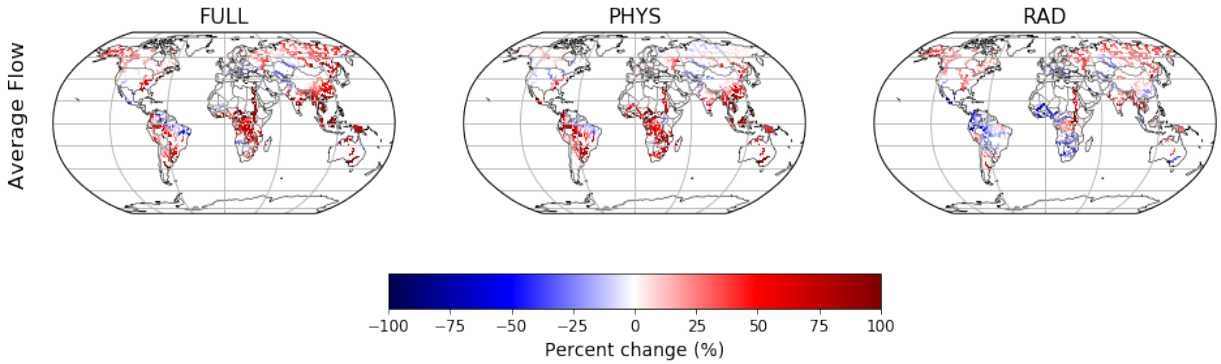

Figure B.4: *Changes in annual mean streamflow.*

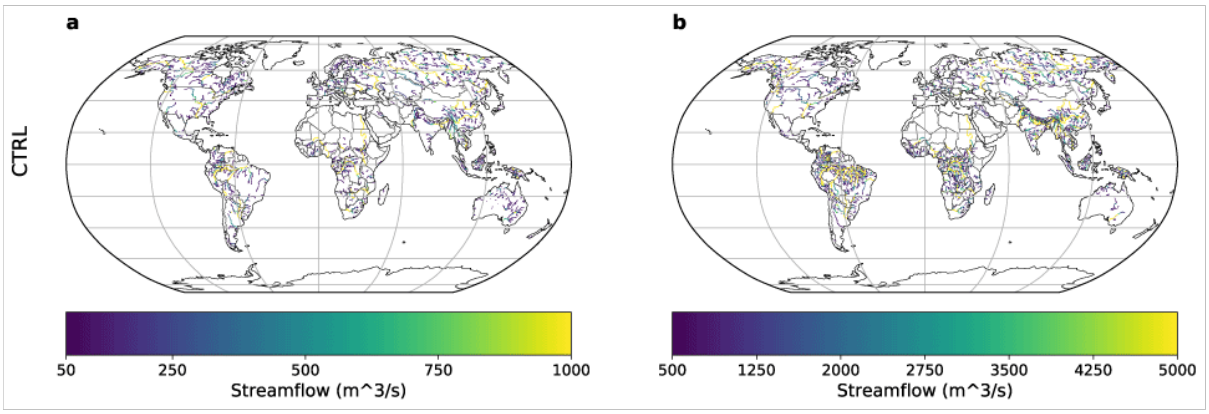

Figure B.5: *CTRL (a) Q_{low} and (b) Q_{high} for comparison against the changes presented in Figures 2 and S7*

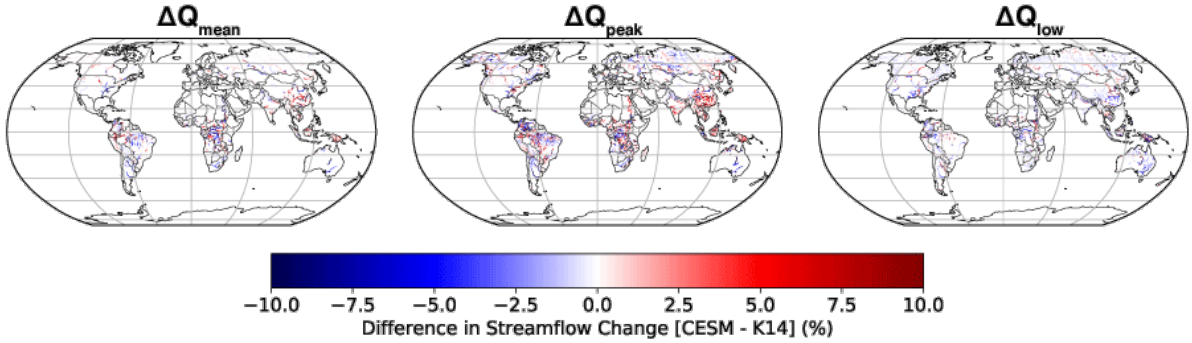

Figure B.6: *Percent difference between the streamflow change in the CESM* FULL *simulation and the CMIP5 RCP8.5 multi-model means in* K14. *Note that the color bar here is ten times smaller than that of Figure S4.*

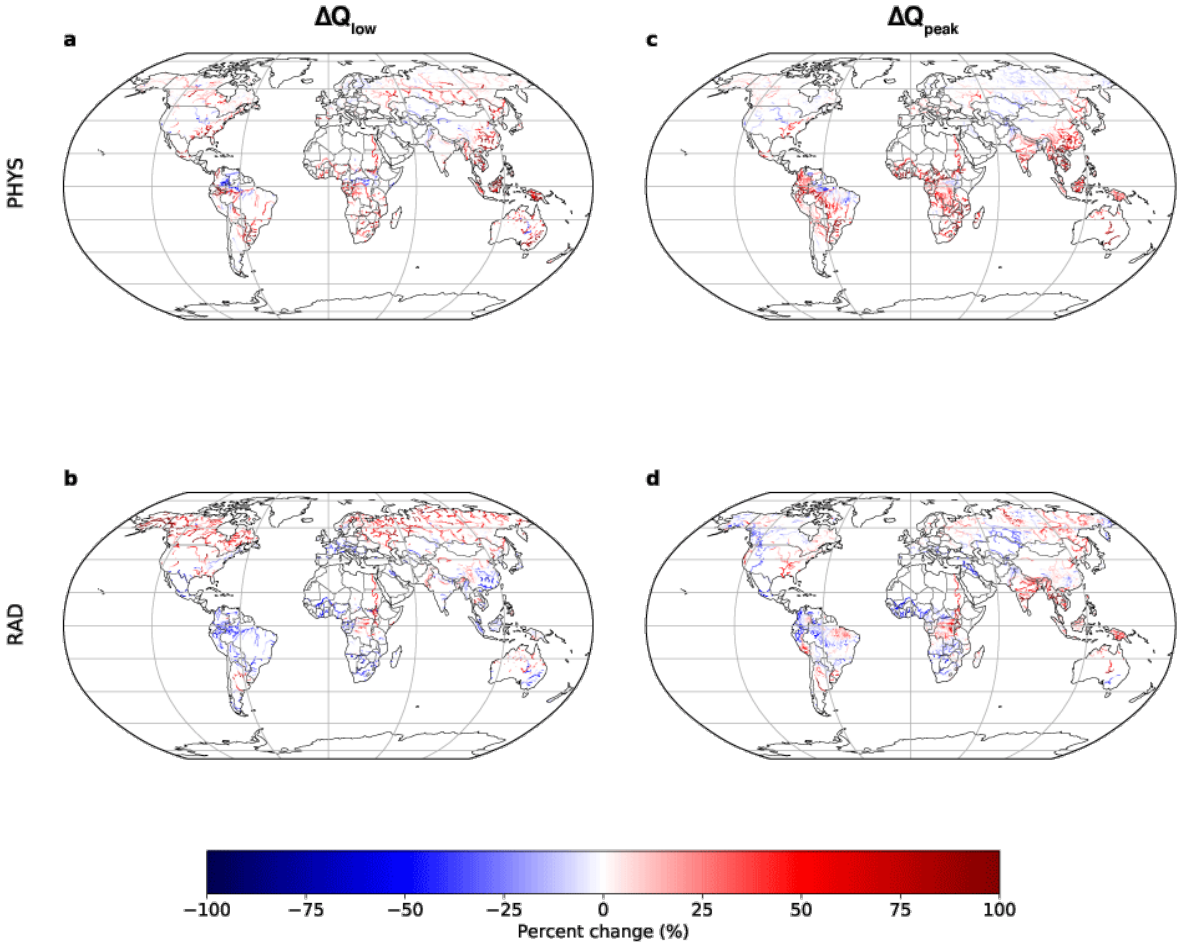

Figure B.7: *Change in (a,c) Qlow and (b,d) Qhigh for (a,b) PHYS and (c,d) RAD. Masking applied as in Figure 2.*

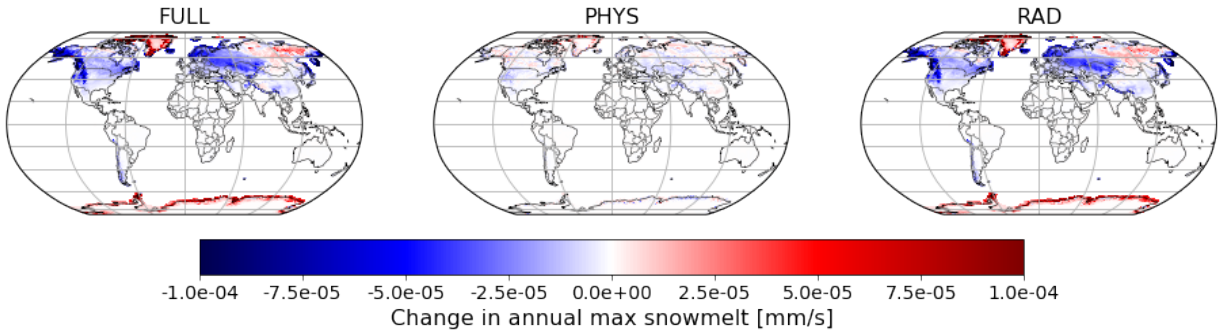

Figure B.8: *Changes in annual maximum snowmelt rates.*

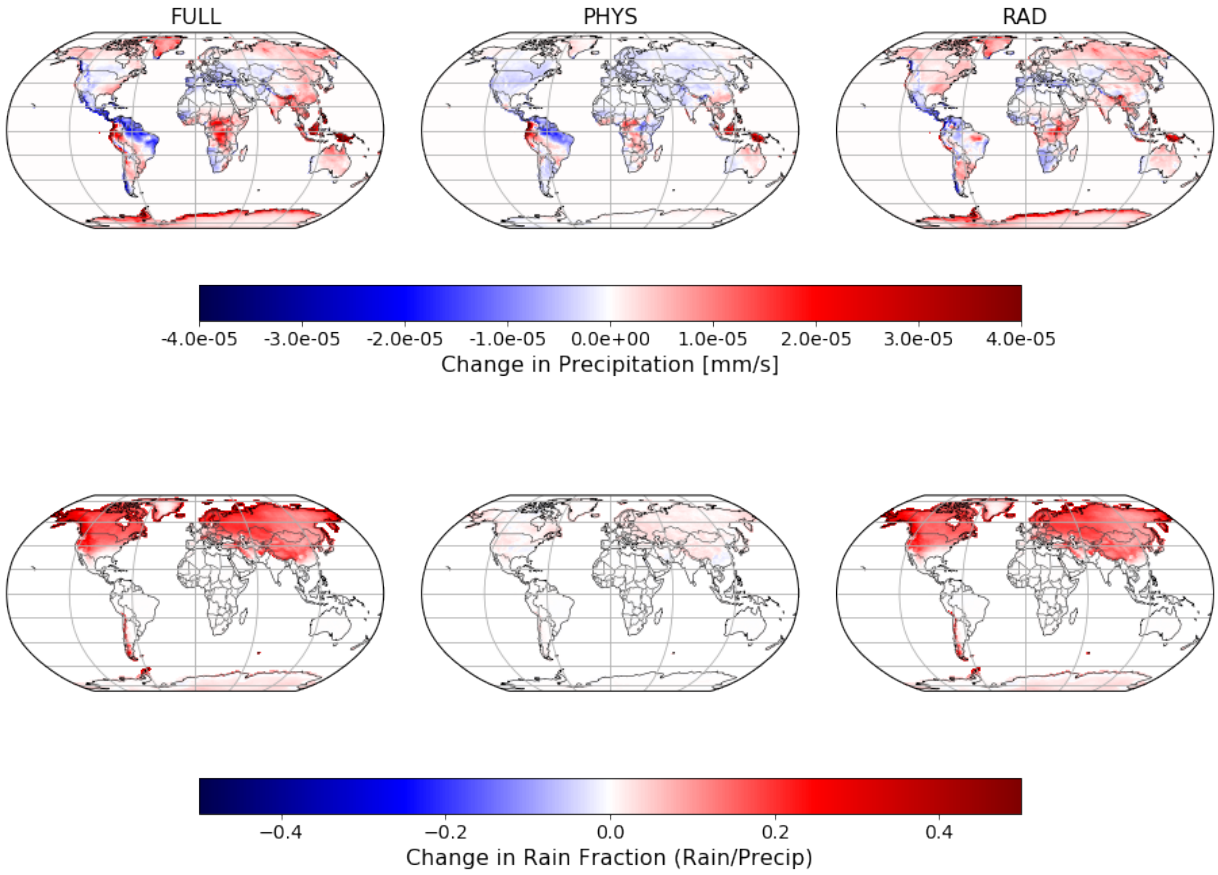

Figure B.9: *Change in average precipitation rate (top) and in the fraction of that rate that reaches the surface as rain instead of snow (bottom).*

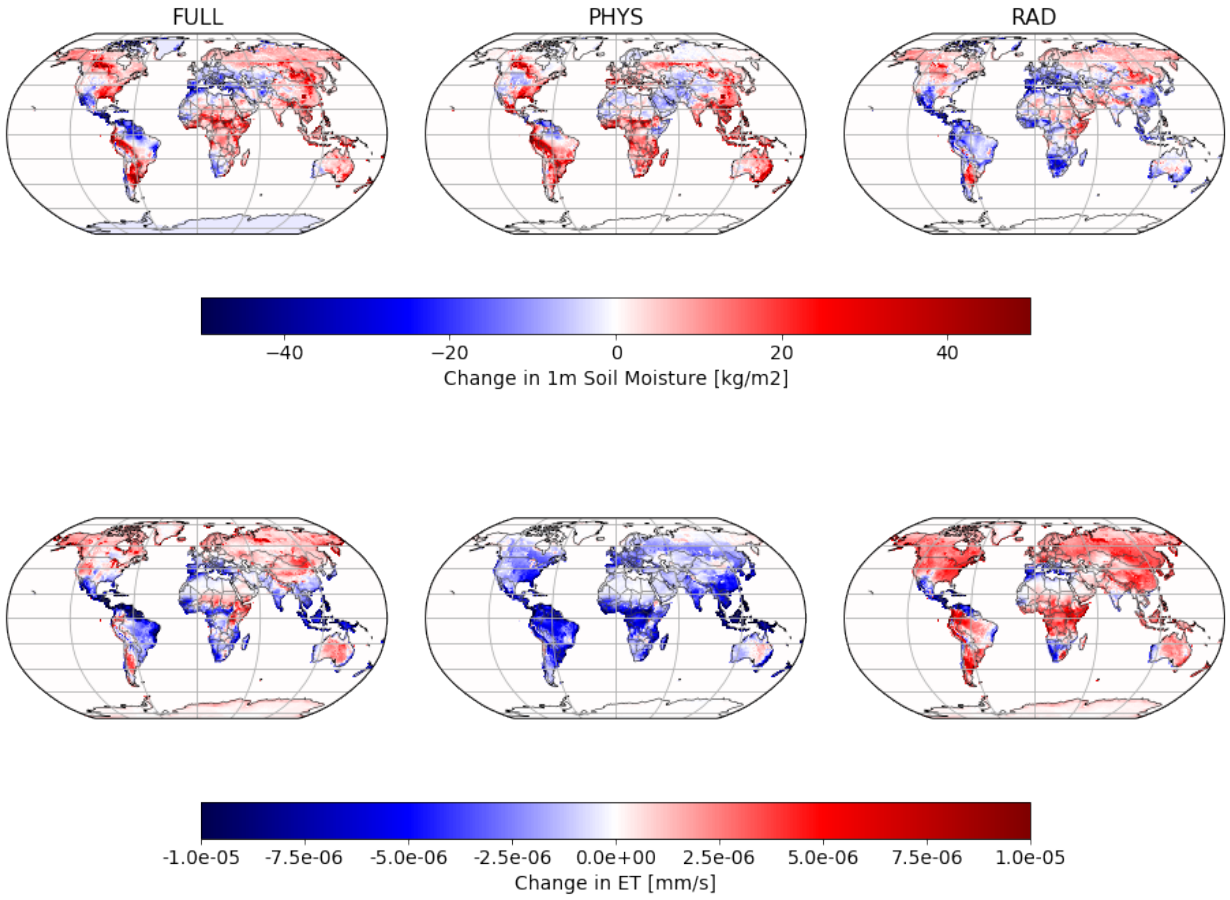

Figure B.10: *Change in average 1m soil moisture (top) and in average evapotranspiration (bottom).*

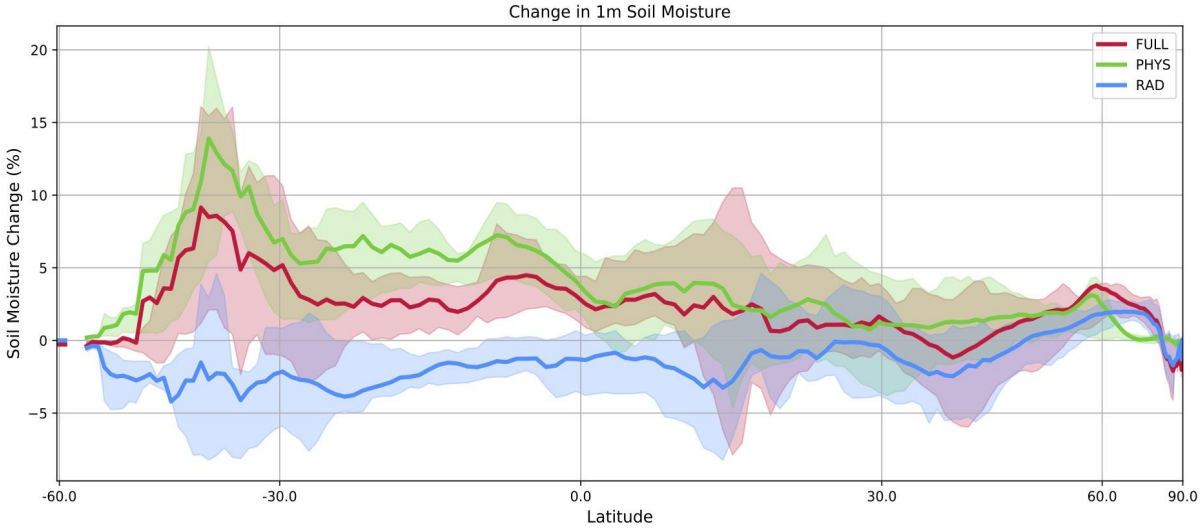

Figure B.11: *Change in smoothed 1m soil moisture. Smoothing applied as in Fig. 3, though no masking of gridcells has been applied in this case.*

	Tropics (30˚S-30˚N)	Mid- and high-latitudes (30-90˚S, 30-90˚N)
PHYS	0.67	0.48
RAD	0.36	0.81

Table B.4: *Correlation coefficient (R) between the change in FULL and either PHYS or RAD (as depicted in Figures 2 and S3).*

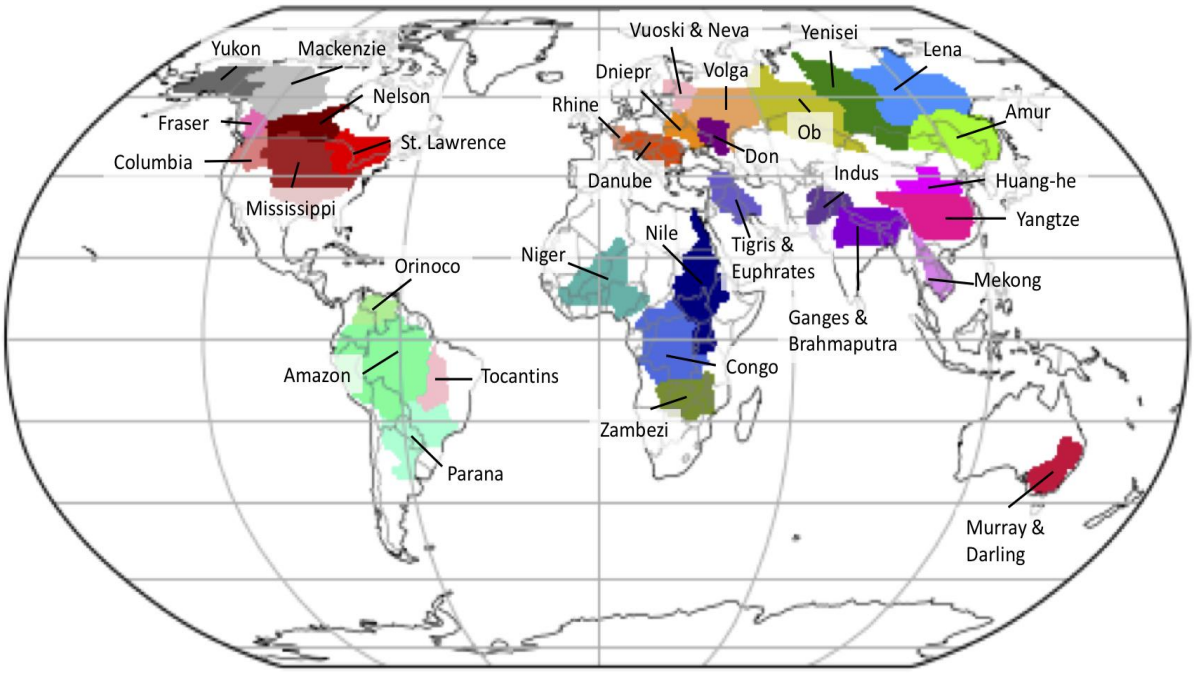

Figure B.12: *River basins assessed in this study.*

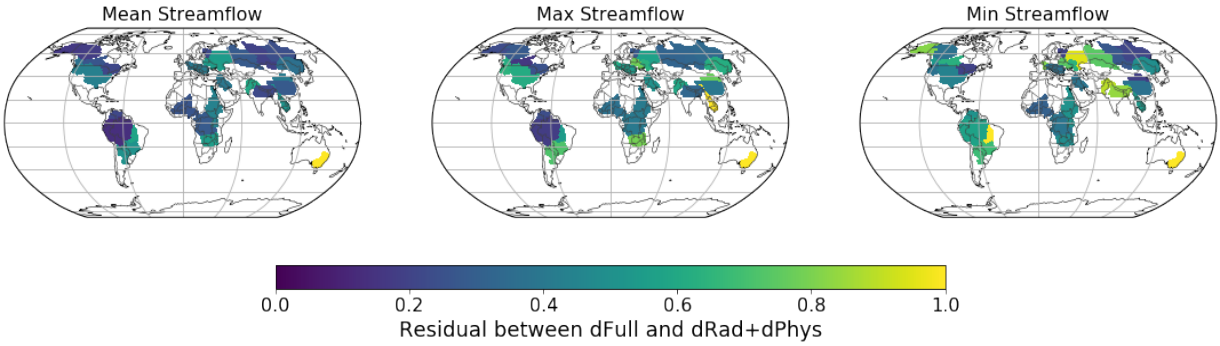

Figure B.13: *Residual of linear equation, defined as the root mean squared error between FULL and RAD+PHYS for all 30 years in each basin.*

Q_{mean} Linearity Analysis

	$CTRL\ (m^3\ s^{-1})$	$\Delta FULL$ (%)	$\Delta PHYS$ (%)	ΔRAD (%)	ε (%)
Yukon	4011.96	33.68	2.66	29.81	16.61
Mackenzie	3700.77	29.09	10.69	19.66	17.91
Columbia	3144.51	14.65	3.87	23.02	43.46
Nelson	1175.45	15.06	8.82	18.65	26.32
Mississippi	2752.70	41.25	13.55	29.83	43.01
St. Lawrence	3426.80	7.05	-5.77	14.86	21.10
Rhine	1677.32	-0.81	8.91	-5.89	38.46
Danube	2290.04	-16.58	13.04	-22.88	41.17
Dniepr	1901.25	-4.89	9.56	9.26	54.90
Volga	3353.25	32.00	26.70	36.54	54.51
Ob	3129.92	2.90	2.26	-5.95	28.45
Yenisei	3694.71	26.55	8.41	19.91	19.59
Lena	4262.81	35.38	4.18	26.60	23.86
Amur	3688.36	57.62	26.79	26.47	36.52
Orinoco	8033.61	-12.24	2.94	-9.77	21.52
Parana	4118.13	49.37	70.42	-4.22	50.73
Amazonas	8584.14	14.45	31.74	-12.47	13.57
Niger	2604.15	19.46	50.63	-43.34	26.41
Congo	7722.23	63.93	42.69	9.04	28.50
Nile	5523.38	120.02	47.85	56.14	43.93
Zambezi	4101.12	32.39	48.97	-10.82	55.30
Tigris & Euphrates	958.72	-53.87	-4.32	-42.38	39.84
Indus	2897.65	-5.23	-3.27	-2.95	59.63
Ganges & Brahmaputra	5499.62	30.01	7.27	16.72	22.08
Mekong	3200.94	89.40	77.07	29.96	51.74
Huang-He	4207.62	32.31	12.93	12.78	41.08
Yangtze	5290.31	44.78	34.46	3.17	27.82
Murray & Darling	1430.79	105.39	197.73	-27.12	346.65
Don	2512.12	16.32	20.10	24.47	56.07
Fraser	2576.83	18.58	4.75	21.08	36.82
Tocantins	5144.31	-1.22	11.97	2.73	58.57

Vuoski & Neva	1039.55	22.35	-5.01	24.12	22.09

Table B.5: *For each of the basins assessed, 30-year averaged mean streamflow (Q_{mean}) is reported along with the percent change from that in FULL, PHYS, and RAD. The RMSE (ε) values between ΔFULL and ΔRAD+ΔPHYS for all thirty years is also reported. Basins that do not meet the linearity criteria are shown in grey.*

Q_{peak} Linearity Analysis

	$CTRL\ (m^3\ s^{-1})$	$\Delta FULL$ (%)	$\Delta PHYS$ (%)	ΔRAD (%)	ε (%)
Yukon	7496.18	0.32	5.24	-3.64	22.69
Mackenzie	6251.49	5.67	11.93	-1.87	27.97
Columbia	8725.18	-3.53	10.70	4.70	64.31
Nelson	1628.75	-0.42	5.09	0.63	15.78
Mississippi	3822.31	58.57	23.57	49.11	61.19
St. Lawrence	3775.37	9.34	-4.71	14.27	25.31
Rhine	3005.07	16.87	21.09	8.50	61.35
Danube	2885.41	-13.76	18.04	-21.47	55.23
Dniepr	2654.52	-3.81	16.31	16.79	78.35
Volga	6502.04	11.41	22.36	11.91	56.87
Ob	5691.13	-10.65	1.17	-18.74	31.94
Yenisei	7223.18	16.73	-0.13	14.22	32.48
Lena	8749.14	21.72	-2.86	22.94	34.30
Amur	5176.19	77.75	29.83	40.37	61.95
Orinoco	15938.49	18.51	22.36	3.48	23.68
Parana	6428.74	61.88	85.30	-3.39	72.05
Amazonas	12878.61	24.57	35.33	-5.93	17.83
Niger	4665.74	24.43	56.11	-40.38	37.37
Congo	13601.92	52.92	27.01	14.53	40.24
Nile	6083.53	119.93	53.50	55.40	41.20
Zambezi	8013.36	53.63	71.40	-6.18	78.97
Tigris & Euphrates	1296.36	-55.51	-2.07	-46.36	50.40
Indus	5929.52	-7.09	-2.15	-5.94	59.45
Ganges & Brahmaputra	11961.83	37.53	11.79	22.61	33.18
Mekong	5928.97	141.76	111.98	66.02	120.81
Huang-He	6357.90	52.56	23.50	20.37	76.62
Yangtze	9842.45	46.04	34.14	5.66	39.53
Murray & Darling	2877.77	149.66	312.39	-22.06	600.03
Don	4574.01	4.68	17.47	7.88	63.70
Fraser	8037.87	-12.24	18.26	-12.88	61.95

Tocantins	15096.85	11.62	15.99	5.43	54.57
Vuoski & Neva	1173.58	28.35	-4.03	28.46	27.25

Table B.6: *As in Table B.5, but for peak flow (Q_{high}).*

Q_{low} Linearity Analysis

	$CTRL\ (m^3\ s^{-1})$	$\Delta FULL$ (%)	$\Delta PHYS$ (%)	ΔRAD (%)	ε (%)
Yukon	1118.12	223.74	7.73	206.82	81.72
Mackenzie	1959.35	80.97	24.02	67.06	37.88
Columbia	719.92	-1.83	-0.36	3.85	37.68
Nelson	710.94	57.94	28.81	67.47	63.57
Mississippi	1636.28	24.25	4.11	8.81	43.77
St. Lawrence	3103.41	5.60	-6.71	14.97	19.92
Rhine	699.42	-13.15	12.49	-9.39	80.95
Danube	1608.07	-20.42	12.03	-24.43	36.91
Dniepr	1113.61	0.10	10.27	15.56	74.98
Volga	1502.64	52.55	39.72	73.51	95.26
Ob	857.89	97.17	22.66	75.39	74.48
Yenisei	1643.60	56.88	26.13	33.07	27.16
Lena	1301.99	29.28	11.43	19.04	21.05
Amur	1920.18	92.45	54.71	37.82	49.04
Orinoco	1077.24	-35.79	-33.07	-9.61	50.67
Parana	2430.49	59.57	73.05	-1.61	68.29
Amazonas	2847.29	-10.23	47.39	-25.18	57.75
Niger	1298.61	16.12	51.42	-46.66	30.79
Congo	2841.73	94.06	96.08	-1.18	38.81
Nile	5091.86	121.02	47.89	57.17	50.95
Zambezi	1569.89	12.28	38.98	-14.78	48.76
Tigris & Euphrates	724.03	-57.94	-4.44	-44.44	38.29
Indus	440.80	38.56	-2.82	31.98	89.62
Ganges & Brahmaputra	732.20	69.48	18.28	32.27	84.14
Mekong	1211.87	51.63	53.15	10.78	53.88
Huang-He	2754.64	13.29	2.86	7.48	18.64
Yangtze	2104.30	43.15	44.61	-2.53	37.13
Murray & Darling	716.70	55.45	103.34	-26.28	123.79
Don	1364.88	4.85	19.82	22.71	64.35
Fraser	604.16	-0.19	6.07	12.45	53.44
Tocantins	239.66	-6.02	56.71	-7.20	142.26

Vuoski & Neva	889.14	18.41	-5.68	21.77	19.56

Table B.7: *As in Table B.5 but for low flow (Q_{low}).*

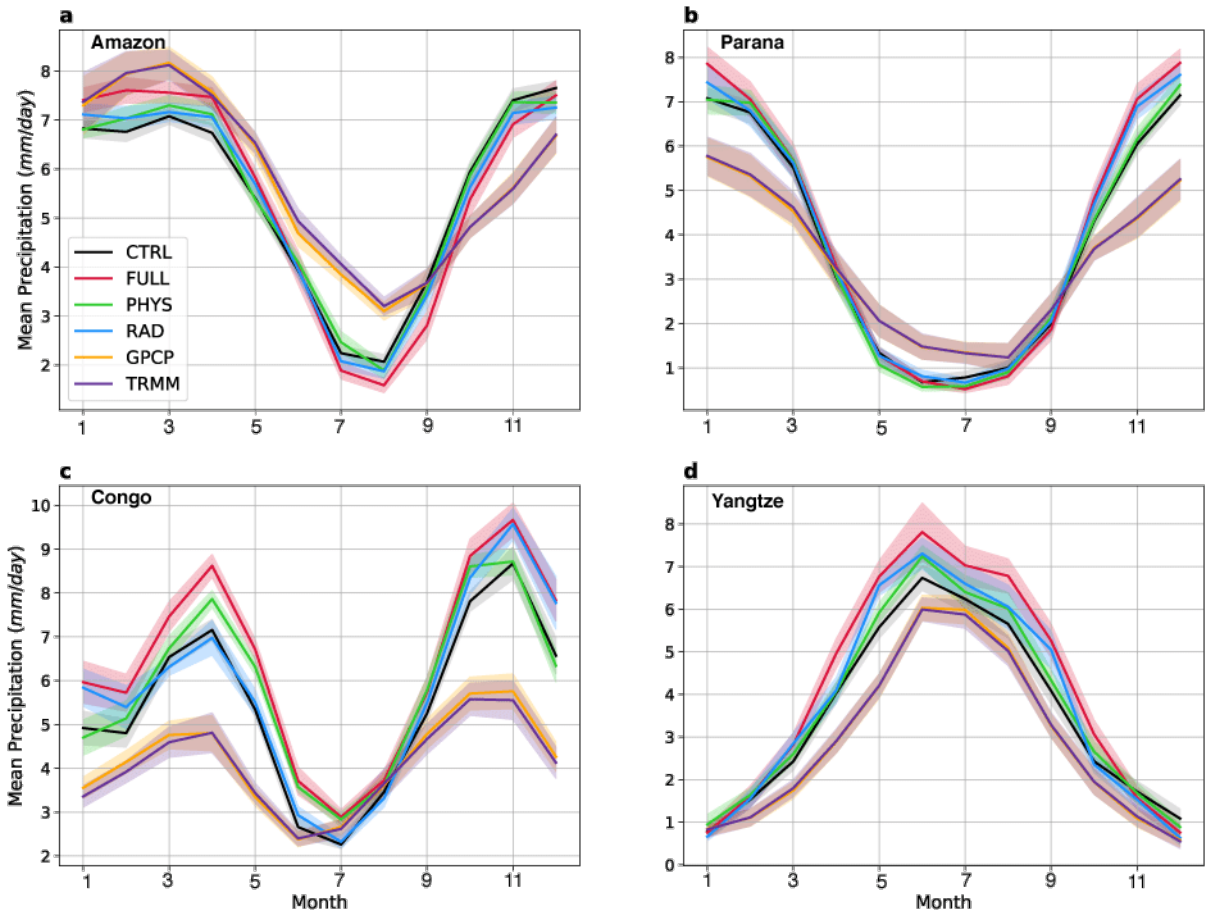

Figure B.14: *Annual cycle of precipitation in basins selected for further analysis in* Figure 3.4*. Observations are averaged from GPCP or TRMM over the period of 1998-2013, while CESM experiments are averaged over the 30-year period used for analysis. Both are averaged over the whole basin.*

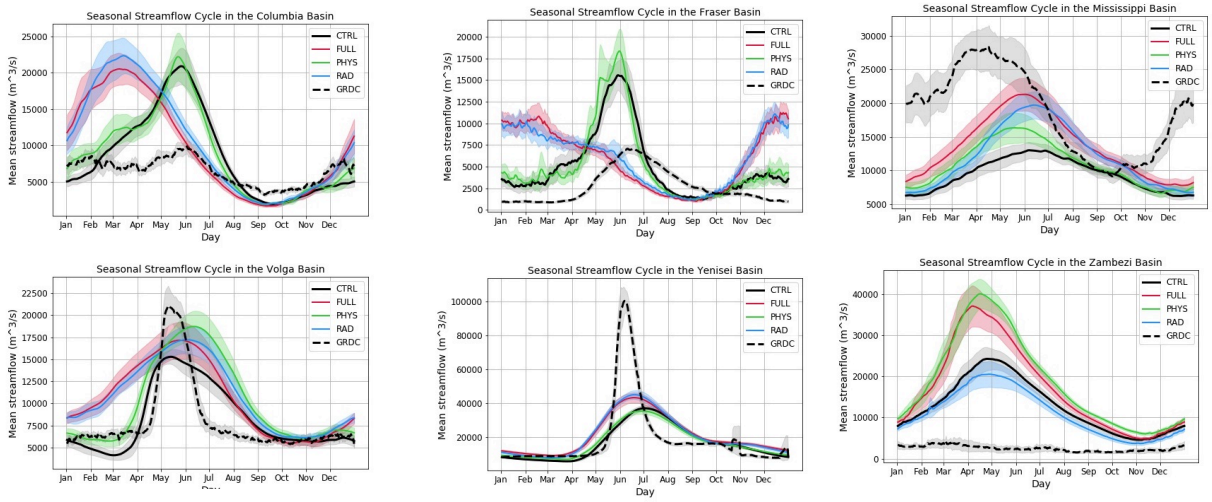

Figure B.15: *Annual cycle of streamflow in basins where the timing of peak/low flow shows a shift in* FULL *relative to* CTRL*.*

Appendix C

Supplementary Information for Chapter 4

C.1 Creation of MJO phase climatologies

The model used to create thousands of synthetic TCs, the MIT model, relies on inputs of monthly environmental variables, a time scale that is prohibitive for assessing modulation by the MJO. A single MJO event can have a period as short as 30 days and in that time progress through eight distinct phases. The challenge then is to create monthly averages consistent with single phases of the MJO. We do this by grouping days with an active MJO according to their month and phase, resulting in a series of 96 month-phase pairs (12 months by 8 phases). That is to say, we construct a record of days in January with active phase 1 conditions, February with phase 1 conditions, and so on until an annual climatology is created for each phase of the MJO.

Inevitably, the selection process of grouping days by month and MJO phase results in either more or less days than are necessary to fill a particular month. In the case that there were not enough MJO events of a particular phase to fill a given month, the available observations were randomly resampled to fill in the remainder of the month. For the RMM, this was the case for just 2 pairs (2.1% of the pairs), with a minimum of 26 observations in September during phase 3. For the OMI, 7 pairs (7.3%) required this resampling, with a minimum of 15 observations in September for phase 1. On the other end of the spectrum, some pairs had over 100 observations available for use. In those cases, we selected days with the strongest MJO amplitudes to use in downscaling. Though this may have slightly tipped the odds in favor of finding a significant modulation of cyclogenesis by the MJO, neither index seems to modulate TC number based on their amplitude alone (not shown).

C.2 Supporting figures

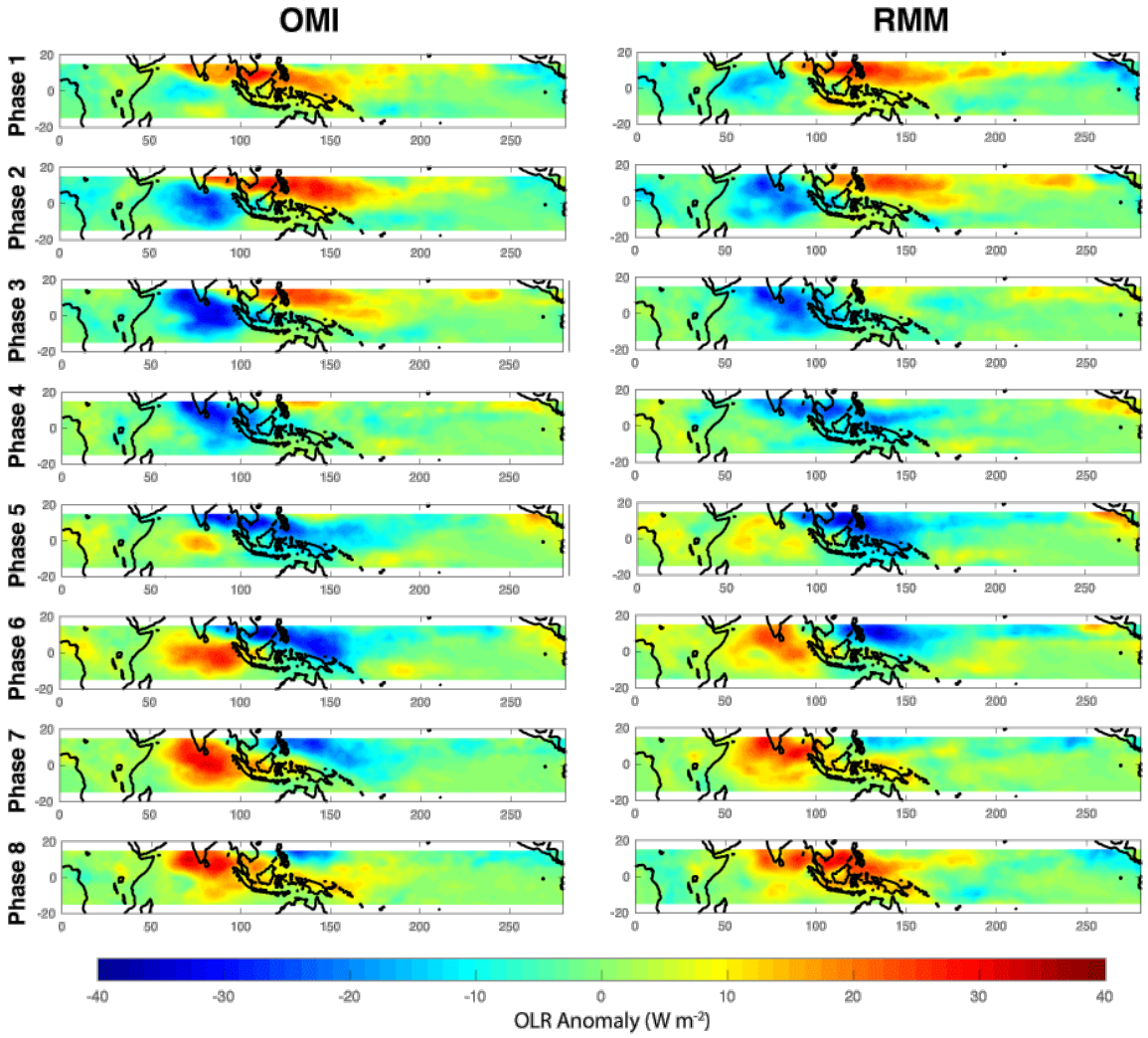

Figure C.1*: OMI and RMM anomalies of outgoing longwave radiation (OLR). The anomaly for each phase is taken by removing the Phase 1-8 mean from the average OLR for all days within the TC season of June-November for a given phase's climatology (i.e., using the month-phase pairs described in Section 2).*

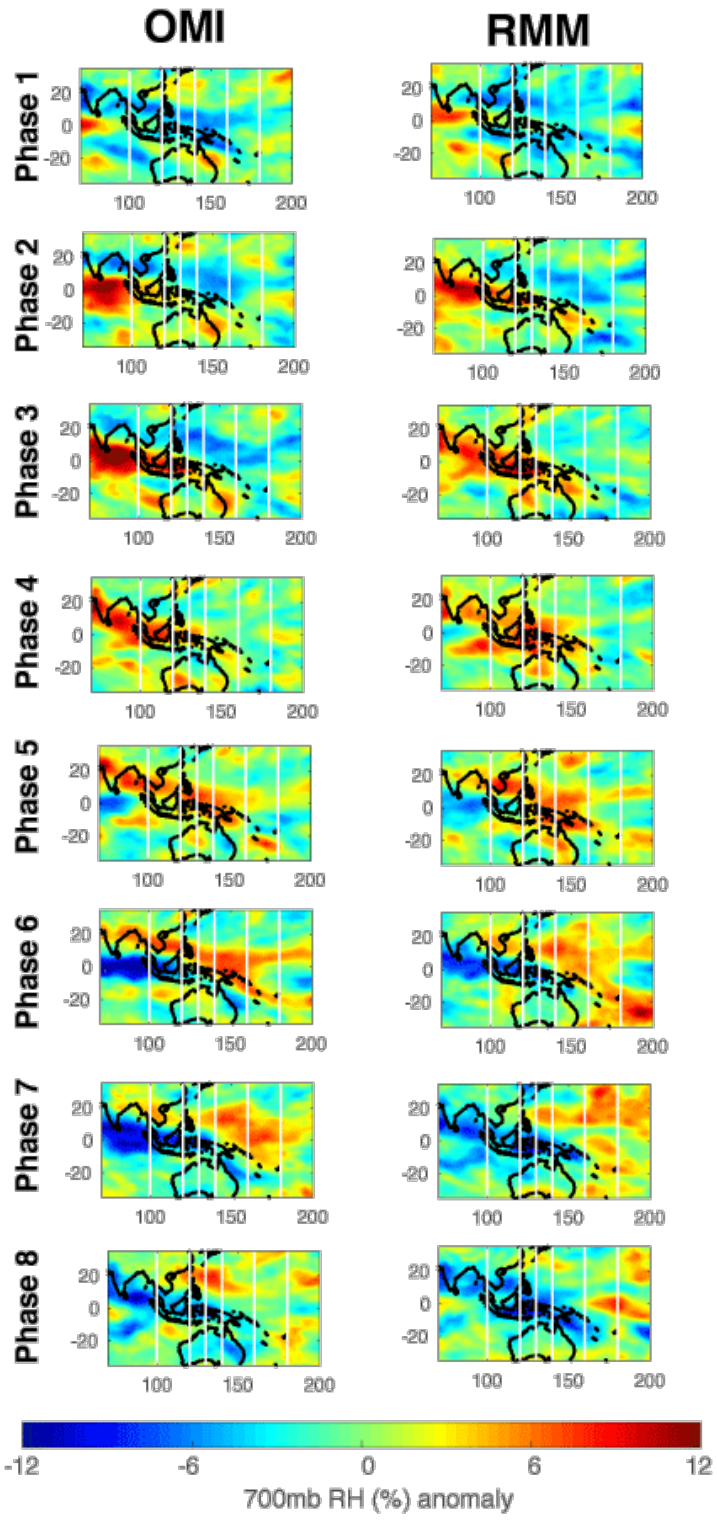

***Figure C.2**: As in Fig. C.1 but for 700 hPa relative humidity.*

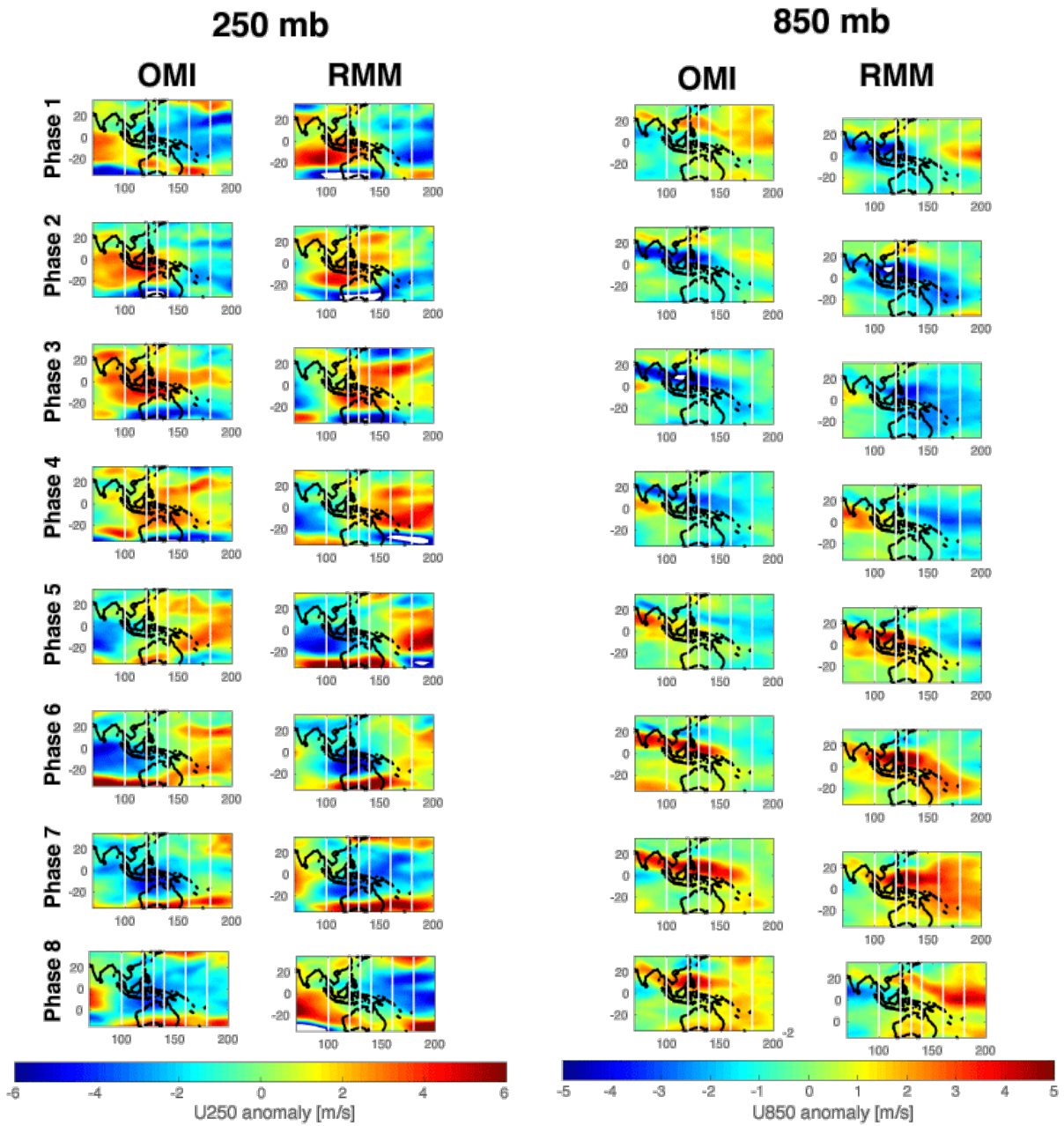

Figure C.3*: As in Fig. C.1, but for zonal wind anomalies at 250 and 850 hPa (U250 and U850 respectively).*

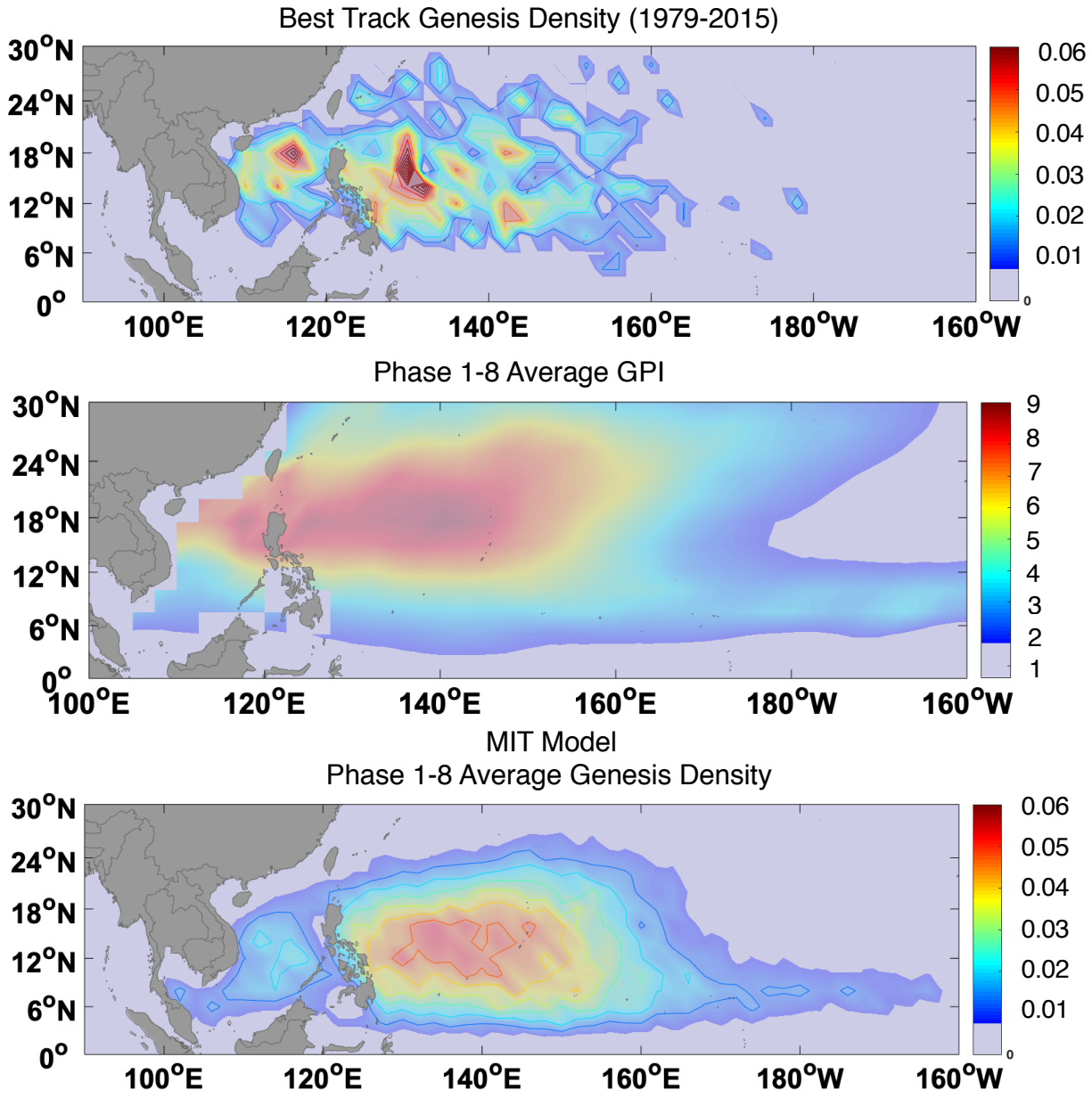

***Figure C.4**: Genesis density from (top) the best track record provided as part of the MIT model, from 1979-2015 during the TC season of Jun-Nov, compared to (middle) MJO Phase 1-8 (OMI) average genesis potential index (GPI), and (bottom) the Phase 1-8 (OMI) average genesis density as produced by downscaling.*

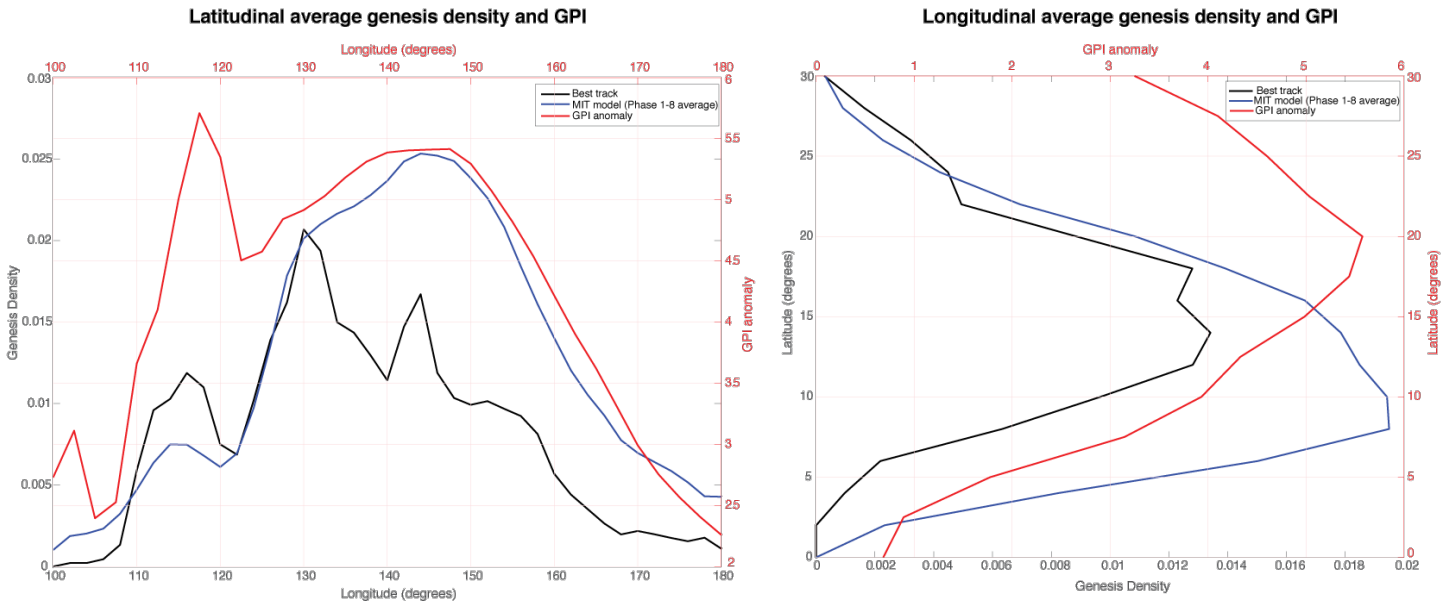

Fig. C.5: *Genesis density from (black) best track records from 1979-2015 during the TC season of Jun-Nov and (blue) MJO Phase 1-8 (OMI) average as produced by the MIT model downscaling (Jun-Nov), compared to (red) Genesis Potential Index (GPI), which is plotted on the upper and rightmost axes in each plot. These are averaged over longitude to get zonal means (right) or over latitude to get meridional means (left). Meridional means are smoothed with a 4° running mean for genesis density and a 5° running mean for GPI.*

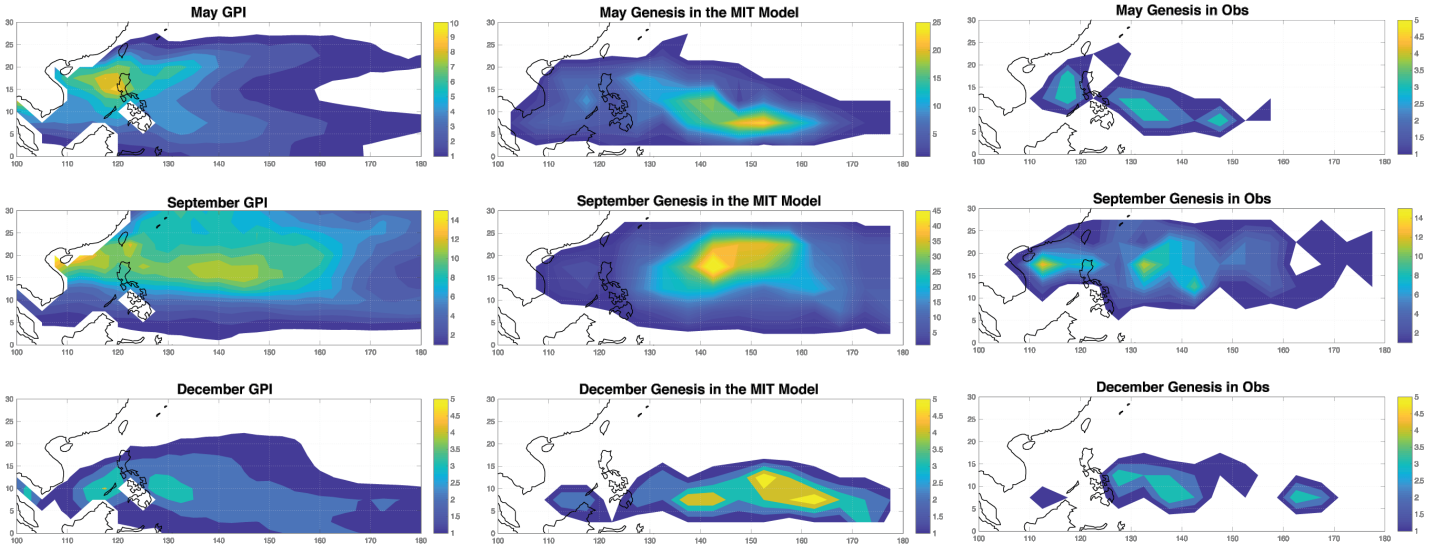

Figure C.6: *Number of TC geneses in May (top), September (middle row), and December (bottom) as determined by observations from 1979-2015 (right), the MIT model (middle column), and GPI (left).*

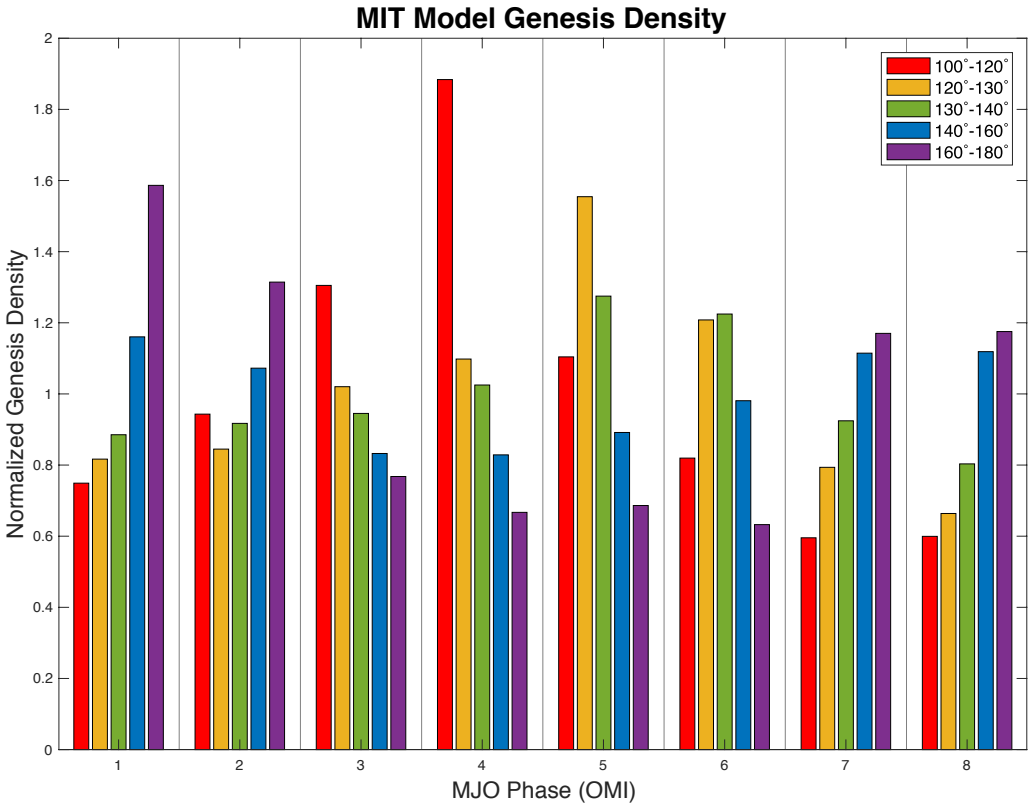

Figure C.7*: Regional breakdown of genesis density in the MIT model downscaling results. Each phase is defined as in OMI for comparison to the GPI analysis in Figure 4.2, and overall genesis density is normalized by the mean genesis density in a given region.*

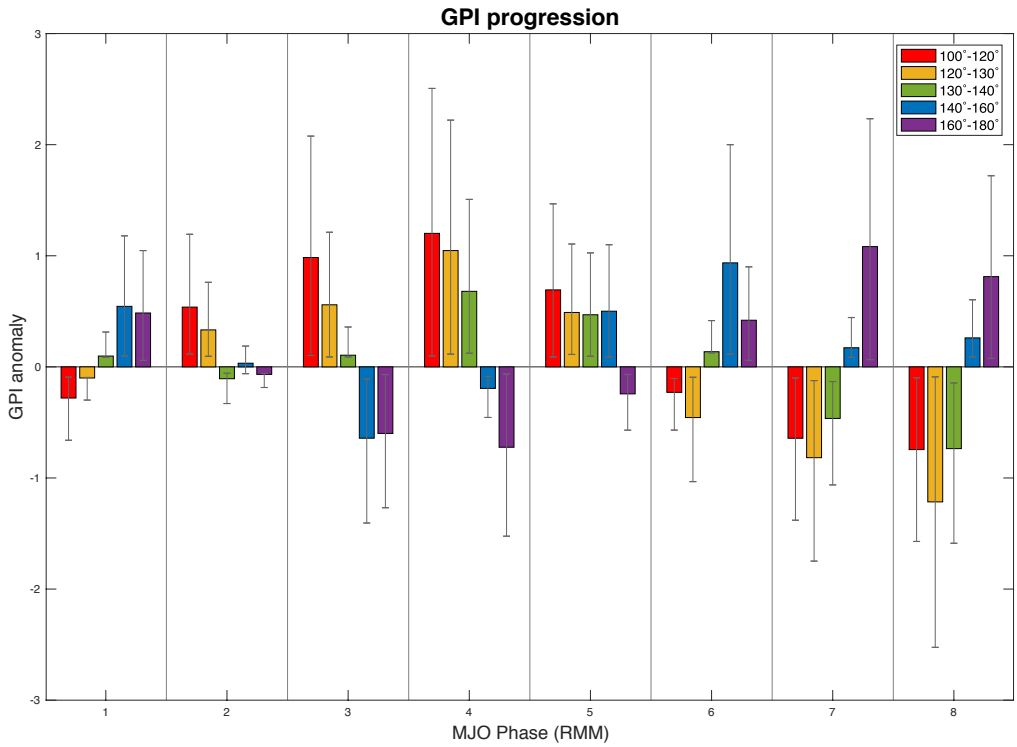

***Figure C.8**: As in Figure 4.2 - anomalous GPI for each phase of the RMM-defined MJO (x-axis), relative to the Phase 1-8 mean, as computed in Equation 4.1. Each region is assessed individually, shown as colored bars, which represent the mean of the 100-member bootstrap for the TC season of June-November with error bars corresponding to the 25th and 75th percentiles of that analysis.*

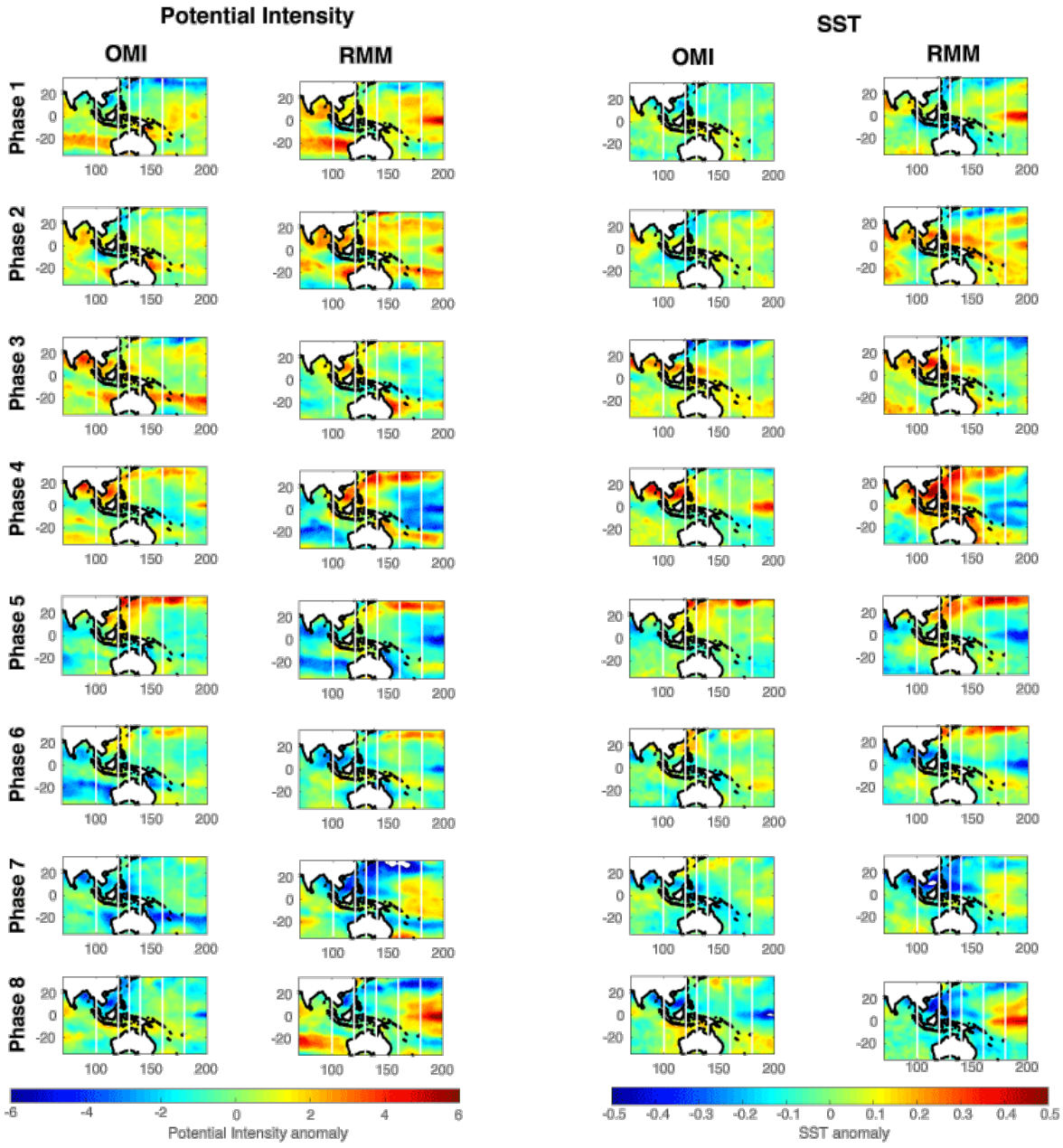

Figure C.9: *As in Fig. C.1, but for potential intensity and SST (which contributes to PI).*

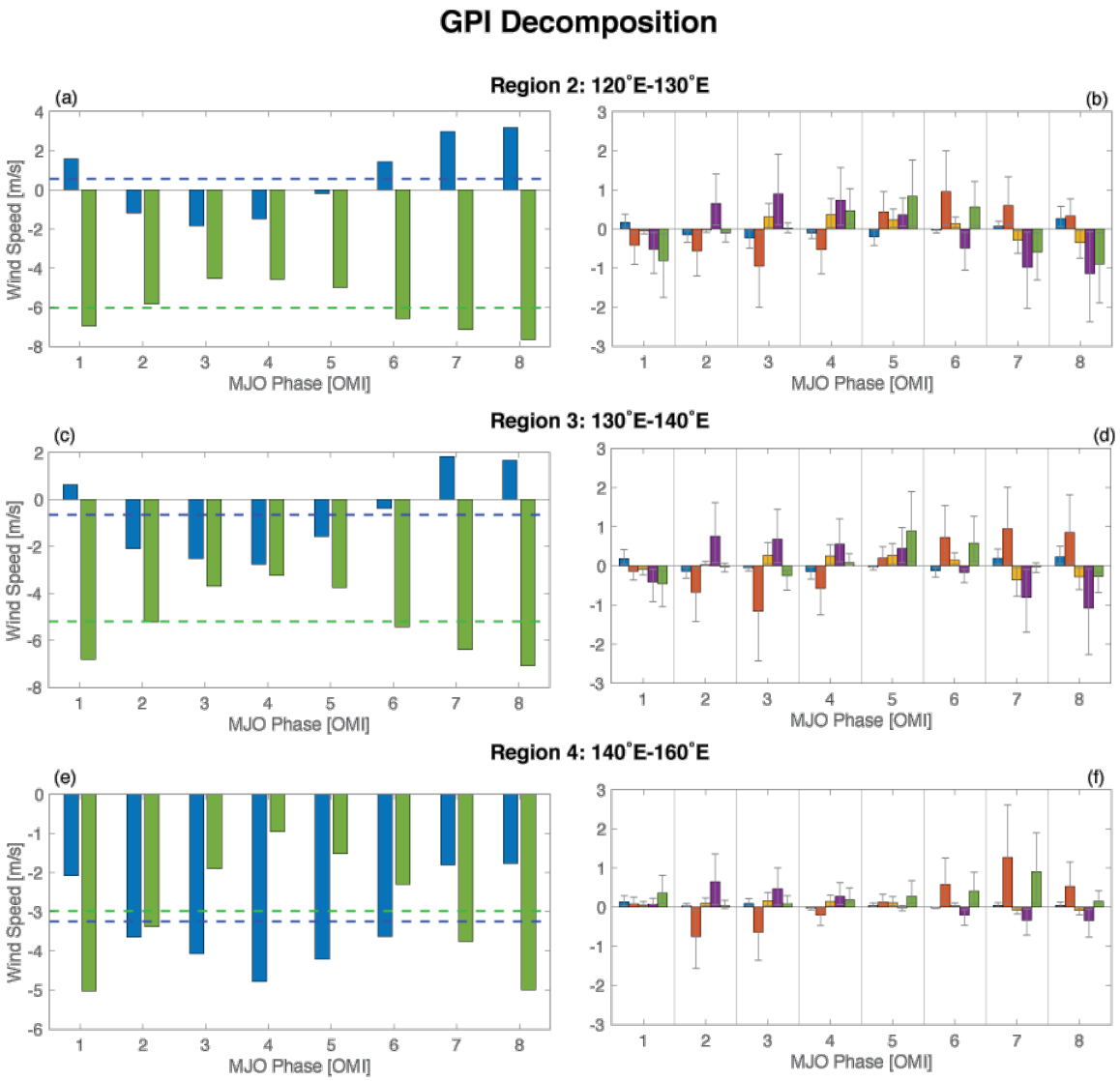

Figure C.10*: As in Figure 4.3, but for Regions 2-4. (Left) average 850 (blue and 350 (green) mb winds in the 100-member bootstrap ensemble for each phase of the MJO; dashed lines represent the Phase 1-8 mean. (Right) average GPI decomposition from Equation 4.1 for each phase of the MJO, taken from the 100-member bootstrap ensemble. Error bars correspond to the 25th and 75th percentiles. Averages are taken for each region over the TC season of June-November.*